



Technische Universität München  
Ingenieur fakultät Bau Geo Umwelt  
Lehrstuhl für Statik

---

METHODOLOGICAL TREATMENT OF NON-LINEAR  
STRUCTURAL BEHAVIOR IN THE DESIGN, ANALYSIS AND  
VERIFICATION OF LIGHTWEIGHT STRUCTURES

Benedikt Franz Philipp

Vollständiger Abdruck der von der Ingenieur fakultät Bau Geo Umwelt der  
Technischen Universität München zur Erlangung des akademischen  
Grades eines

**Doktor-Ingenieurs**

genehmigten Dissertation.

Vorsitzender:

Prof. Dr.-Ing. Stefan Winter

Prüfer der Dissertation:

1. Prof. Dr.-Ing. Kai-Uwe Bletzinger
2. Prof. Dr.-Ing. Rainer Barthel
3. Prof. Marijke Mollaert Ph.D., Vrije Universiteit Brussel

Die Dissertation wurde am 08.06.2017 bei der Technischen Universität  
München eingereicht und durch die Ingenieur fakultät Bau Geo Umwelt  
am 07.11.2017 angenommen.



Schriftenreihe des Lehrstuhls für Statik TU München

Band 36

**Benedikt Franz Philipp**

METHODOLOGICAL TREATMENT OF NON-LINEAR  
STRUCTURAL BEHAVIOR IN THE DESIGN, ANALYSIS AND  
VERIFICATION OF LIGHTWEIGHT STRUCTURES

München 2017

Veröffentlicht durch

Kai-Uwe Bletzinger  
Lehrstuhl für Statik  
Technische Universität München  
Arcisstr. 21  
80333 München

Telefon: +49(0)89 289 22422  
Telefax: +49(0)89 289 22421  
E-Mail: [kub@tum.de](mailto:kub@tum.de)  
Internet: [www.st.bgu.tum.de](http://www.st.bgu.tum.de)

ISBN: 978-3-943683-49-3

©Lehrstuhl für Statik, TU München

## Abstract

Lightweight structures attract with their slender dimensions and their curved shapes. However, they are characterized by pronounced non-linear behavior. Within this thesis consequences on the design, the analysis and the verification of safety of lightweight structures considering their non-linear behavior are discussed and novel methods and techniques for the raised challenges are developed.

To account for the close relation between geometry and load-bearing behavior, the concept of performing structural analyses on CAD models with the *Isogeometric B-Rep Analysis* (IBRA) as a very recent finite element technique is extended to the analysis of structural membranes. A prestressed membrane element and a cable element are formulated. The cable element follows the novel paradigm of embedded B-Rep edge elements. These new developments are investigated and assessed in both academic and real examples.

The shape of lightweight structures in many cases results from an elastic mounting procedure. The large deformations that occur during these mounting processes can have an important impact on the load-bearing behavior. In order to account for this impact, the configuration update between different construction stages of the structure is investigated. A review of existing methods is followed by an in-depth development of mechanically accurate update procedures that are applied to selected examples of increasing complexity.

Only little guidance exists for the verification of lightweight structures considering their non-linear behavior. Based on reviews of existing standards for the verification of non-linear structures and of the underlying principles of the *Eurocodes*, the behavior of structural membranes is analyzed in detail. As a contribution to the development of a future *Eurocode* for structural membranes, propositions for the classification of their non-linear behavior and – in a more general sense – for their verification are made.

## Zusammenfassung

Tragwerke des Leichtbaus begeistern durch ihre schlanken Abmessungen und ihre gekrümmten Formen. Allerdings weisen sie ein ausgeprägt nichtlineares Tragverhalten auf. Im Rahmen dieser Arbeit werden Auswirkungen dieses Tragverhaltens auf den Entwurf, die Analyse und den Sicherheitsnachweis von Leichtbautragwerken unter Berücksichtigung ihres nichtlinearen Verhaltens diskutiert und neue Methoden und Techniken für die erarbeiteten Fragestellungen entwickelt.

Um die unmittelbare Abhängigkeit von Geometrie und Lastabtragung zu berücksichtigen, wird das Konzept der Strukturanalyse auf dem CAD Modell mittels der *Isogeometrischen B-Rep Analyse* (IBRA), einer jungen Finite Element Technik, auf die Analyse von Membrantragwerken erweitert. Ein vorgespanntes Membranelement und ein Seilelement werden formuliert, wobei das Seilelement hierbei dem neuen Ansatz eingebetteter B-Rep Kantenelemente folgt. Diese Neuentwicklungen werden anhand verschiedener akademischer und realer Beispiele untersucht und getestet.

Die Form leichter Tragwerke ist oft das Ergebnis ihres Aufbauprozesses wobei die dabei auftretenden großen Verformungen erheblichen Einfluss auf die Lastabtragung haben können. Um diesen Einfluss zu berücksichtigen, wird das Konfigurationsupdate zwischen den einzelnen Bauzuständen des Tragwerks untersucht. Auf eine Übersicht über bestehende Methoden folgt eine detaillierte Entwicklung von mechanisch präzisen Update-Methoden, die anschließend in ausgewählten Beispielen mit steigender Komplexität angewandt werden.

Derzeit existieren noch wenige Richtlinien für den Nachweis von Leichtbautragwerken unter Berücksichtigung ihres nichtlinearen Verhaltens. Ausgehend von einer Diskussion bestehender Normen zum Nachweis nichtlinearer Tragwerke sowie der Grundlagen der *Eurocodes* wird das Verhalten von Membrantragwerken im Detail analysiert. Als Beitrag zur Entwicklung eines zukünftigen *Eurocodes* für Membrantragwerke werden Vorschläge für die Klassifizierung ihres nichtlinearen Tragverhaltens und – im allgemeinen Sinne – für ihren Nachweis gemacht.

## Acknowledgments

This thesis was written from 2010 to 2017 during my time as research and teaching associate at the Chair of Structural Analysis (Lehrstuhl für Statik) at the Technische Universität München.

First of all, I would like to express my gratitude towards Prof. Dr.-Ing. Kai-Uwe Bletzinger for giving me the possibility to work in the fascinating, challenging, rewarding and inspiring field of lightweight structures. The academic freedom he provided in combination with his interest and passion for the subject allowed for a great working environment and a very enriching experience, on scientific, academic and personal level. Teaching with him in a very self-responsible way will always be one of the highlights of my professional career.

I also want to thank Prof. Dr. Marijke Mollaert and Prof. Dr.-Ing. Rainer Barthel for completing my board of examiners and Prof. Dr.-Ing. Stefan Winter for the organization. Their interest in my work is gratefully acknowledged.

Furthermore I would like to thank all coworkers at the Chair of Structural Analysis for the friendly cooperation and the pleasant time I had working with them. Among them I want to mention especially Falko Dieringer, Michael Breitenberger and Ann-Kathrin Goldbach who inspired my work with numerous discussions and did the proof-reading of my thesis. PD Dr.-Ing. habil. Roland Wüchner has always been open for discussions on- and off-topic and has supported me at all times, which I am very grateful for.

Finally, I want to thank my family for their unconditional support, not only of my work, but – far more important – of my life. Thank you!

Benedikt Philipp  
Weilheim  
November 2017



# LIST OF SYMBOLS

## Calligraphic letters

$\mathcal{D}$  Trimmed domain

$\mathcal{G}$  Gaussian space

## Greek letters

$\boldsymbol{\sigma}, \boldsymbol{\sigma}_0$  Cauchy stress tensor and prestress as Cauchy stress

$\gamma$  (Partial) factor of safety or load amplification factor

$\Gamma_0, \Gamma$  Boundary of the physical domain in the reference resp. current configuration

$\lambda$  Load amplification factor or homotopy factor

$\boldsymbol{\epsilon}, \boldsymbol{\epsilon}$  Green-Lagrange strains for membranes resp. line elements

$\boldsymbol{\Xi}, \mathbf{H}$  Knot vector in  $\xi$  resp.  $\eta$  direction

$\Omega_0, \Omega$  Physical domain in the reference resp. current configuration

$\theta_i, \theta^i$  Co- resp. contravariant coordinates

$\xi, \eta$  Parameters for B-Splines resp. NURBS geometries

$\tilde{\xi}$  Parameter for B-Splines resp. NURBS curves within the parameter space

## Mathematical symbols and operators

$\det[\square]$  Determinant

## List of Symbols

$\square \otimes \square$  Dyadic product

$(\square \cdot \square)$  Inner product

$(\cdot)_{,i}$  Partial derivatives w.r.t. to a quantity  $i$

$(\cdot)_{,r}$  Partial derivatives w.r.t. to a discretization parameter  $u_r$

### Latin letters and sub- resp. superscripts

$\square_d$  Design value of an entity (factored)

$\square_h$  Approximated field

$\square_k$  Characteristic value of an entity (unfactored)

$\Delta \mathbf{u}$  Displacement increment

$\delta W$  Virtual work

$\delta \mathbf{u}$  Virtual displacement field

$\hat{\mathbf{u}}$  Discretization parameters for the displacement field

$\mathbf{A}$  Metric tensor on a surface

$\mathbf{A}_i, \mathbf{A}^i$  Co- resp. contravariant basis on surface

$\mathbf{C}$  B-Spline resp. NURBS curve

$\mathbf{E}$  Green-Lagrange strain tensor

$\mathbf{E}_i, \mathbf{e}_i$  Global resp. local orthonormal coordinate system

$\mathbf{F}$  Deformation gradient

$\mathbf{f}_{\text{int}}$  Internal force vector

$\mathbf{G}_i, \mathbf{G}^i$  Co- resp. contravariant basis in space

$\mathbf{K}$  Tangential stiffness matrix or curvature tensor

$\mathbf{P}$  Control point or 1<sup>st</sup> Piola-Kirchhoff (PK1) stress tensor

$\mathbf{R}$  Residual force vector or rotation tensor

$\mathbf{S}$	B-Spline resp. NURBS surface or 2 <sup>nd</sup> Piola Kirchhoff (PK2) tensor
$\mathbf{S}_0$	Prestress as 2 <sup>nd</sup> Piola Kirchhoff (PK2) stress
$\mathbf{u}$	Displacement field
$\mathbf{u}_0$	Initial displacement
$\mathbf{X}, \mathbf{x}$	Geometry in the reference and current configuration, respectively
$\mathbf{X}_{\text{surf}}$	Spatial point on a surface in the reference configuration
$\tilde{\mathbf{C}}$	Trimming curve in the parameter space
$\tilde{\mathbf{G}}$	Local base vector of an embedded B-Rep edge within the parameter space
$\tilde{\mathbf{P}}$	Control point in the parameter space
$A_{ij}, A^{ij}$	Co- resp. contravariant metric coefficients on surface
$B_{\alpha\beta}, B^{\alpha\beta}$	Co- resp. contravariant coefficients of the curvature tensor
$E$	Young's modulus or effect of action
$E_{ij}$	Coefficients of the Green-Lagrange strain tensor
$EA, EI$	Axial resp. bending stiffness of a line element
$F$	Action
$f(\square)$	Function of $\square$
$G, Q$	Permanent resp. variable action
$H$	Mean curvature of a surface
$J$	Jacobian used for different mapping operations
$K$	Gaussian curvature of a surface or stiffness for single DOF system
$K_{rs}$	$(r, s)^{\text{th}}$ component of the stiffness matrix
$L, \ell$	Length (of a line element) in the reference resp. current configuration

## List of Symbols

$N$	(B-Spline) basis function in $\eta$ direction or normal force in line element
$n_{\square}$	Number of entity $\square$
$p, q$	Polynomial degree in $\xi$ and $\eta$ direction, respectively
$R$	NURBS basis function or radius or resistance
$R_r$	$r^{\text{th}}$ component of the residual force vector
$t$	Thickness of a membrane
$w$	Control point weight or quadrature weight or deflection

## Abbreviations

B-Rep	Boundary representation
CAD	Computer-aided design
CAE	Computer-aided engineering
DOF	Degree of freedom
EC	Eurocode
FE	Finite element
FEA	Finite element analysis
FEM	Finite element method
IBRA	Isogeometric B-Rep analysis
IGA	Isogeometric analysis
NURBS	Non-uniform rational B-splines
TUM	Technische Universität München
ULS, SLS	Ultimate resp. serviceability limit state

# CONTENTS

<b>List of Symbols</b>	<b>vii</b>
<b>Contents</b>	<b>xi</b>
<b>1 Introduction</b>	<b>1</b>
<b>2 Fundamentals</b>	<b>5</b>
2.1 Basics of geometry and its description	6
2.1.1 Differential geometry of surfaces in space . . . . .	8
2.1.2 Geometry parameterization and discretization . . . . .	12
2.2 NURBS-based B-Rep models	16
2.2.1 NURBS, NURBS curves and NURBS surfaces . . . . .	16
2.2.2 Trimmed surfaces and the trimming operation . . . . .	20
2.2.3 Boundary Representation (B-Rep) . . . . .	23
2.2.4 Integration procedure . . . . .	24
2.2.5 Exact geometry representation in IGA . . . . .	25
2.3 Structural mechanics for finite displacements	25
2.3.1 Kinematics . . . . .	25
2.3.2 Stresses and material law . . . . .	28
2.3.3 Equilibrium . . . . .	29
2.3.4 Discretization and solution approach . . . . .	31
2.4 Characteristics of geometrically non-linear beam elements	32
2.4.1 Finite rotations and their parameterization . . . . .	34
2.4.2 Buckling of beam elements . . . . .	36
2.4.3 Applied beam element formulation . . . . .	39
2.5 Characteristics of structural membranes	42
2.5.1 Load-bearing behavior of structural membranes	42

## Contents

2.5.2	Principal design steps for structural membranes	43
2.5.3	Form-finding of tensile structures . . . . .	46
<b>3</b>	<b>Integration of geometry and structural behavior with IBRA</b>	<b>53</b>
3.1	Interaction of geometry and structural behavior	54
3.2	IBRA for lightweight structures	55
3.3	Developments for analyzing tensile structures with IBRA	56
3.3.1	Membrane element accounting for prestress . . .	57
3.3.2	Embedded cable element accounting for prestress	59
3.3.3	Outlook on cutting pattern generation with IBRA	67
3.4	Evaluation of the developed components	69
3.4.1	Non-linear analysis of a stretched quarter-circle .	69
3.4.2	Form-finding of a catenoid . . . . .	73
3.5	Application examples for lightweight structures with IBRA	78
3.5.1	Generation of an inflated bubble cluster . . . . .	79
3.5.2	Form-finding of the <i>Olympiastadion München</i> . .	83
3.5.3	Grid structures on surfaces of zero mean curvature	85
<b>4</b>	<b>Interaction of deformation and structural behavior</b>	<b>91</b>
4.1	Deformation-based structures	92
4.1.1	Gridshells – Creating curvature through bending	93
4.1.2	Hybrid structures – Tension with bending . . . . .	97
4.2	Including deformation in structural analysis	102
4.2.1	Construction stages in structural engineering . .	103
4.2.2	Geometric non-linearity and construction stages	110
4.3	Modeling and analysis of deformation-based structures	111
4.3.1	Applied element formulations . . . . .	111
4.3.2	Update of configurations and coupling of elements	113
4.4	Applications for the simulation of the mounting process	119
4.4.1	Structural analysis after form-finding . . . . .	120
4.4.2	Guided movements with contracting cables . . . .	125
<b>5</b>	<b>Safety verification of membrane structures</b>	<b>133</b>
5.1	General design practice in civil engineering	134
5.1.1	The semi-probabilistic method . . . . .	134
5.1.2	The principal concept of the Eurocodes . . . . .	135
5.2	Non-linear behavior and verification approaches	137
5.2.1	Linear behavior and related simplifications . . . .	138

5.2.2	Verification concepts for geometric non-linearity	139
5.3	Membrane structures and the Eurocode framework	144
5.3.1	Verification guidelines for membrane structures	144
5.3.2	Classification of the non-linear behavior . . . . .	146
5.3.3	Further aspects related to verification . . . . .	157
5.4	Methodological approach for verification of safety	160
5.4.1	Prestress in the context of safety verification . . .	160
5.4.2	Safety verification and the numerical model . . .	161
<b>6</b>	<b>Conclusions and outlook</b>	<b>165</b>
	<b>Bibliography</b>	<b>169</b>



## INTRODUCTION

Contemporary structural design often aims at a reduction of the invested material. Besides the obvious economic advantages of this reduction, using less material and therefore less “gray energy” is closely related to the ecological impact of the structure. In architectural design, the reduction of the applied material often implicates minimalistic, clear structures reduced to the essential.

Lightweight structures are a natural answer to those demands. Although the concept of lightweight construction perfectly fits those contemporary requirements, the idea already disposes of a long tradition: Already in 1940 Fritz LEONHARDT [83, p. 413, transl.] proclaimed

*"Lightweight construction – a demand of our time",*

a statement that certainly has lost nothing of its relevance despite its age. Compared to conventional structures, lighter structures also follow different load-bearing principles, with considerable impact on their design: Lightweight structural design aims at an advantageous stress distribution, characterized by normal forces entailing a full utilization of the cross

section. In order to allow for this stress distribution, the shape has to be adapted to the desired load-bearing characteristics. Beyond load-bearing, lightweight construction often includes an optimized production: To this aim, the use of initially straight resp. flat members and a simple mounting procedure are to be preferred.

In general lightweight structures are characterized by non-linear behavior in their structural design and analysis. Two aspects are considered of special relevance in the current context:

- The required adapted shape allowing for the advantageous load-bearing through normal forces is the result of a form-finding resp. optimization process in most cases, either through specialized numerical applications or by using physical experiments like hanging shapes.
- The reduction in material generally leads to a lower stiffness and thus entails larger deformations. These finite deformations are beyond the scope of linear structural behavior and linearized kinematics.

The design and analysis of lightweight structures deals with these aspects since its first days. In that context often the design of the roof structure of the *Olympiastadion München* (1972) is considered a seminal project, which built the basis of a wide development for numerical applications in civil engineering. Nowadays new challenges for the numerical design and analysis of lightweight structures arise.

This thesis intends to give more insight to some of these challenges and to propose adequate techniques for the consideration of non-linear structural behavior in the analysis and design of lightweight structures. Therefore the fields dealt with can be outlined as follows:

- The tight relation between geometry and structural behavior for lightweight structures requires a close interaction of geometric modeling (design) and mechanical simulation (analysis). Therefore a common model description is needed for both purposes that allows for a real interaction and the advantageous use of the respective methods.

- The simulation of the deformation process during the mounting of lightweight structures and the determination of the impact on further load-bearing behavior requires a mechanically consistent description of the mounting process.
- Beyond the analysis of lightweight structures, the verification of safety considering their non-linear behavior still is the subject of intense discussions.

For each field, the current state of the art will be presented as a basis and further necessary developments will be worked out including a detailed derivation of novel mechanical aspects and methodological approaches. The derived components and techniques will be critically assessed and discussed in detail.

### **Outline of the thesis**

CHAPTER 2 reviews the necessary fundamentals for the subsequent developments. The basics of geometry description, parameterization and the application of NURBS-based B-Rep models are introduced. Following a short review of structural mechanics under consideration of finite displacements, characteristics of geometrically non-linear beam elements and finite rotations are pointed out. Finally the specific behavior and computation approaches for structural membranes as main examples within this thesis are reviewed.

CHAPTER 3 presents the *isogeometric B-Rep analysis* (IBRA) integrating the geometry of structures and their load-bearing behavior in one model. To this aim the concept of IBRA is described and the necessary components for analyzing tensile structures – mainly a prestressed membrane element and an embedded cable element – are elaborated. An evaluation of the developed components in terms of accuracy, speed and robustness is followed by selected application examples.

CHAPTER 4 starts with a review of realized deformation-based structures of different scales and highlights the influence of deformation on the load-bearing behavior of lightweight structures. Existing approaches of construction stage analysis as an approach to properly account for the effect of deformation in later structural simulations are critically assessed. Based on these considerations, methods for the update of configurations in a

## 1 Introduction

multi-stage analysis of non-linear structures are discussed. Application examples and novel simulation approaches to simulate deformation-based structures and their mounting close this chapter.

CHAPTER 5 is focused on the verification of safety for geometrically non-linear structures. A review of existing verification concepts and standards yields the present basis for the verification of structural membranes. In regard of the development of a future Eurocode for structural membranes, possible classifications of the behavior of tensile structures are exemplified and investigated in detail.

CHAPTER 6 gives conclusions and an outlook on future research.

**Remark:** All structural simulations shown in the present thesis have been obtained with the research code *Carat++* [29] of the Chair of Structural Analysis, Technische Universität München.

## FUNDAMENTALS

Dealing with lightweight structures and their design and analysis requires various aspects from the fields of structural mechanics as well as differential geometry. In that context, the necessary fundamentals for the developments in the next chapters will be introduced here.

Lightweight structures draw their load-bearing capacity out of their geometry. Hence an emphasis is made on the fundamentals of geometry description and parameterization, as well as discretization with (low-order) polynomials and NURBS-based B-Rep models. The large displacements that can be encountered for many lightweight structures necessitate geometrically non-linear kinematics. These are discussed together with their implications on the solution process with FEA.

Finally the chapter reviews specific aspects for geometrically non-linear beam elements and for structural membranes, since these will be focused on in the structures discussed in the sequel.

## Conventions

Note the following conventions that will be used throughout this thesis if not indicated differently:

- Greek letters ( $\alpha, \beta$ ) can take the values  $\{1, 2\}$ , whereas Latin indices ( $i, j$ ) can take the values  $\{1, 2, 3\}$ .
- Capital letters, like  $\mathbf{X}$  and  $\mathbf{A}_1$ , refer to the reference configuration. The description in the current configuration is indicated by lower case letters, e.g.  $\mathbf{x}$  or  $\mathbf{g}_3$ .
- The partial derivative w.r.t. a quantity  $i$  will be written  $(\bullet)_{,i}$  and the partial derivative w.r.t. to a discretization parameter  $u_r$  is abbreviated as  $(\bullet)_{,r}$ .
- Quantities referring to a local Cartesian basis will be denoted by an overbar,  $(\bar{\bullet})$ . The corresponding bases will be denoted by  $\mathbf{E}_i$  resp.  $\mathbf{e}_i$ .
- Einstein summation convention is used: When an index variable appears as super- and subscript index within a single term, summation of that term over all the values of the index is implied, e.g.  $a_\alpha b^\alpha = a_1 b^1 + a_2 b^2$ .
- For the structural examples and applications unit-free quantities are assumed, if not indicated differently. Hence an arbitrary length and force measure may be applied consistently in these examples.

## 2.1 Basics of geometry and its description

The mechanical objects that are discussed in the sequel are reductions of the reality in several ways. Three of these are of special importance for the following developments:

- *Physical reduction*: In order to simplify their description, the mechanical behavior of structures is often homogenized to some extent. For instance the ensemble of yarns and fill of a textile membrane is commonly represented by a homogeneous material within the material law, see also Section 2.3.2.

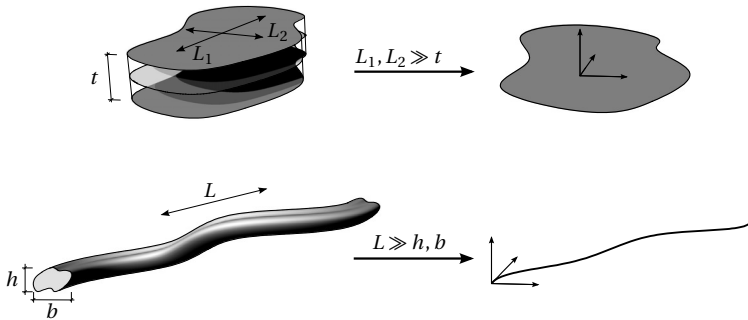


**Figure 2.1:** Dimension reduction for a surface structure to its mid-surface and for a line structure to its center-line

- *Geometric reduction:* Surface structures – in the present context membrane and shell elements – are commonly characterized by their mid-surface, whereas line structures such as cables, trusses and beams are characterized by their center-line, as illustrated in Figure 2.1. Therefore the corresponding mechanical properties are commonly pre-integrated in order to significantly simplify the description of those entities.
- *Discretization:* In order to allow for the numerical treatment of the structural problem to solve, the continuous geometry has to be discretized to a finite number of degrees of freedom (DOFs), see Sections 2.1.2 and 2.3.4.

If not indicated differently in the sequel the geometrically reduced mid-surface resp. center-line description assuming homogeneous material properties is considered. In the following sections, relevant fundamentals of geometry and geometry description are briefly laid out as basis for the following chapters. The presentation is mostly done with the example of surfaces. However, the conclusions and derivations are in principle valid for curves, as well.

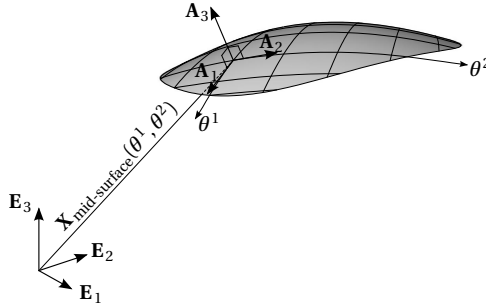


**Figure 2.2:** Differential geometry of a surface: curvilinear parameters  $\theta^\alpha$  with corresponding covariant base vectors  $\mathbf{A}_i$  at the position  $\mathbf{X}_{\text{mid-surface}}(\theta^1, \theta^2)$

### 2.1.1 Differential geometry of surfaces in space

Since a vast amount of literature on differential geometry of surfaces has been published, only a brief introduction is given here. For further reading, the reader is referred *e.g.* to Basar et al. [9], Bischoff et al. [21], Holzapfel [72], Klingbeil [80], Pottman et al. [122], and Walker [147], which also provide the basis for this section.

Mathematically, a surface in space may be represented in different ways, classified as explicit, implicit and parametric representation. Among those, the parametric representation is best suited for general surfaces.

#### Base vectors

For the parametric representation, a net of curvilinear coordinates  $\theta^1$  and  $\theta^2$ , called parameter-lines, is laid out on the mid-surface as illustrated in Figure 2.2, see also Section 2.1.2.

Covariant base vectors  $\mathbf{A}_\alpha$  can then be obtained by

$$\mathbf{A}_\alpha = \frac{\partial \mathbf{X}_{\text{mid-surface}}}{\partial \theta^\alpha} = \mathbf{X}_{\text{mid-surface},\alpha} , \quad (2.1)$$

whereas the third base vector  $\mathbf{A}_3$  is a unit normal vector  $\mathbf{N}$  to the mid-surface<sup>1</sup>. Hence it can be determined as

$$\mathbf{A}_3 = \frac{\mathbf{A}_1 \times \mathbf{A}_2}{|\mathbf{A}_1 \times \mathbf{A}_2|} . \quad (2.2)$$

Using these base vectors, a position vector  $\mathbf{X}_P$  to a point  $\mathbf{P}$  in the three-dimensional body is determined by

$$\mathbf{X}_P = \mathbf{X}(\theta^1, \theta^2, \theta^3) = \mathbf{X}_{\text{mid-surface}}(\theta^1, \theta^2) + \theta^3 \mathbf{A}_3 , \quad (2.3)$$

where  $\theta^3 \in [-t/2; t/2]$ , with  $t$  being the thickness of the structure as illustrated in Figure 2.1.

The contravariant base vectors  $\mathbf{A}^\alpha$  may be introduced as *dual basis* [72] with the definition

$$\mathbf{A}^\alpha \cdot \mathbf{A}_\beta = \delta_\beta^\alpha = \begin{cases} 0 & \text{for } \alpha \neq \beta \\ 1 & \text{for } \alpha = \beta \end{cases} , \quad (2.4)$$

or alternatively by

$$\mathbf{A}^\alpha = A^{\alpha\beta} \mathbf{A}_\beta , \quad (2.5)$$

where  $A^{\alpha\beta}$  are the contravariant metric coefficients that will be introduced in Equation (2.7). For the third base vector, the normal vector to the surface, these considerations lead to  $\mathbf{A}^3 = \mathbf{A}_3$ .

### The metric tensor

Referring to the thus derived base vectors, the so-called metric tensor  $\mathbf{A}$  is given by

$$\mathbf{A} = A_{\alpha\beta} \mathbf{A}^\alpha \otimes \mathbf{A}^\beta = A^{\alpha\beta} \mathbf{A}_\alpha \otimes \mathbf{A}_\beta , \quad (2.6)$$

where the metric coefficients are determined as  $A_{\alpha\beta} = \mathbf{A}_\alpha \cdot \mathbf{A}_\beta$ . The metric is also referred to as *first fundamental form of surfaces*, see Klingbeil [80].

---

<sup>1</sup> Note that for structures defined through their mid-surface the base vectors are commonly referred to as  $\mathbf{A}_i$ , whereas in general they are termed  $\mathbf{G}_i$ . This difference is due to the determination of the third base vector in Equation (2.2): In general  $\mathbf{G}_3$  is neither perpendicular to  $\mathbf{G}_\alpha$  nor of unit length, but to be determined in analogy to Equation (2.1).

## 2 Fundamentals

The contravariant metric coefficients  $A^{\alpha\beta}$  used in Equation (2.5) may be determined through

$$[A^{\alpha\beta}] = [A_{\alpha\beta}]^{-1} . \quad (2.7)$$

With the help of the metric coefficients, a differential piece of area  $dA$  can be computed based on the Lagrangian identity

$$|\mathbf{A}_1 \times \mathbf{A}_2| = \sqrt{A_{11}A_{22} - (A_{12})^2} = \sqrt{\det[A_{\alpha\beta}]} = \sqrt{A} \quad (2.8)$$

as

$$dA = |\mathbf{A}_1 \times \mathbf{A}_2| d\theta^1 d\theta^2 = \sqrt{A} d\theta^1 d\theta^2 . \quad (2.9)$$

It might be convenient to represent tensors in different bases, *e.g.* in a Cartesian basis. If for a tensor  $\mathbf{T}$  the transformation from one basis  $\mathbf{A}_\alpha \otimes \mathbf{A}_\beta$  to another basis  $\tilde{\mathbf{A}}_\alpha \otimes \tilde{\mathbf{A}}_\beta$  is required, the necessary transformation of the tensor coefficients  $T_{\alpha\beta}$  to the corresponding coefficients  $\tilde{T}_{\alpha\beta}$  is performed by

$$\tilde{T}_{\gamma\delta} = T_{\alpha\beta} (\tilde{\mathbf{A}}_\gamma \cdot \mathbf{A}^\alpha) (\mathbf{A}^\beta \cdot \tilde{\mathbf{A}}_\delta) . \quad (2.10)$$

### Curvature properties of a surface

The curvature properties of a surface are characterized through the curvature tensor

$$\mathbf{K} = B_{\alpha\beta} \mathbf{A}^\alpha \otimes \mathbf{A}^\beta = B^{\alpha\beta} \mathbf{A}_\alpha \otimes \mathbf{A}_\beta , \quad (2.11)$$

where  $B_{\alpha\beta}$  is defined as the *second fundamental form* of the surface, see Basar et al. [9], Itskov [76], and Klingbeil [80].

The covariant curvature coefficients  $B_{\alpha\beta}$  are defined as

$$B_{\alpha\beta} = B_{\beta\alpha} = -\mathbf{A}_\alpha \cdot \mathbf{A}_{3,\beta} = \mathbf{A}_{\alpha,\beta} \cdot \mathbf{A}_3 = \frac{1}{2} (\mathbf{A}_{\alpha,\beta} + \mathbf{A}_{\beta,\alpha}) \cdot \mathbf{A}_3 . \quad (2.12)$$

In combination, the metric tensor  $\mathbf{A}$  and the curvature tensor  $\mathbf{K}$  resp. their coefficients are used to define essential geometric properties of a surface at a specific point  $(\theta^1, \theta^2)$ . In the present context curvature properties are in the focus, see Figure 2.3.

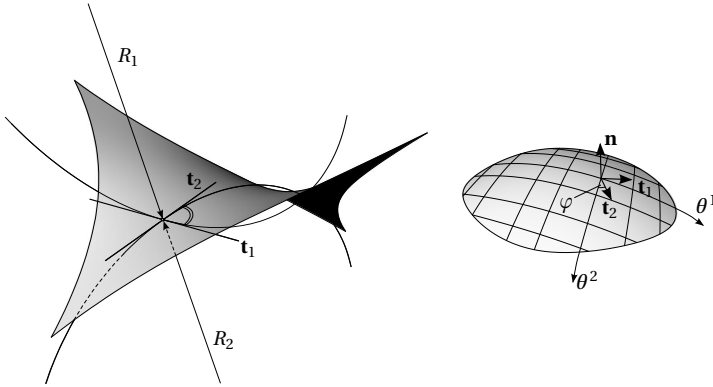


**Figure 2.3:** Curvature properties: principal radii  $R_\alpha$ , tangents  $\mathbf{t}_\alpha$  and surface normal  $\mathbf{n}$  with tangential base vectors

The Gaussian curvature  $K$  is determined by

$$K = \frac{B_{11}B_{22} - (B_{12})^2}{A_{11}A_{22} - (A_{12})^2} = \frac{\det[B_{\alpha\beta}]}{\det[A_{\alpha\beta}]} = \frac{B}{A}, \quad (2.13)$$

as the second invariant  $I_2(\mathbf{K})$  of the curvature tensor. It expresses the product of the principal curvatures  $\kappa_1$  and  $\kappa_2$ ,

$$K = \kappa_1 \kappa_2 = \frac{1}{R_1} \frac{1}{R_2}, \quad (2.14)$$

where  $R_\alpha$  are the principal radii. Regarding their load-bearing behavior, shapes may be characterized based on their Gaussian curvature  $K$ :

- $K > 0$ : a *synclastic* shape, where both principal radii are on the same side of the surface. This shape occurs *e.g.* for pressurized cushions or shells loaded under self-weight, see Figure 2.3 (right).
- $K = 0$ : a *developable* surface which may be flattened without residual stresses, *e.g.* a cylinder or a cone.

- $K < 0$  : an *anticlastic* shape, where both principal radii are on opposite sides of the surface. Mechanically prestressed tensile structures are commonly anticlastic, see Figure 2.3 (left).

The mean curvature  $H$  is determined as

$$H = \frac{1}{2} \frac{B_{11}A_{22} - 2B_{12}A_{12} + B_{22}A_{11}}{\det[A_{\alpha\beta}]}, \quad (2.15)$$

which is expressed through the first invariant  $I_1(\mathbf{K})$  of the curvature tensor, see Basar et al. [9] and Walker [147]. It expresses the arithmetic mean of the principal curvatures  $\kappa_1$  and  $\kappa_2$ :

$$2H = \kappa_1 + \kappa_2 = \frac{1}{R_1} + \frac{1}{R_2} \quad (2.16)$$

As will be referred to in Section 2.5.3, minimal surfaces are characterized by a mean curvature  $H = 0$ .

Note that the measures  $K$  and  $H$  are surface properties which are – just like the principal curvatures  $\kappa_1$  and  $\kappa_2$  – independent of the parameterization. The fact that  $H$  and  $K$  are determined through the first and second invariant of the curvature tensor  $\mathbf{K}$ , respectively, reflects this observation.

### 2.1.2 Geometry parameterization and discretization

As mentioned above, the introduction of a parameterization allows for a description of geometry. In general the handling of geometry – both in CAD (Computer-Aided Design)-tools and in FEA (Finite Element Analysis)-software – requires the possibility to modify shapes and to represent geometry and solution fields through a finite number of discrete parameters.

#### Parametric description of geometries

In an explicit respectively implicit geometry description, a modification might be realized by altering the function parameters  $c_i$ , for instance the radius  $r$  of a circle in 2D:

$$x^2 + y^2 = r \quad (2.17)$$

However, these function parameters are in general not well-suited for direct interaction, *e.g.* through a graphical user-interface (GUI).

In the parametric description the spatial coordinates  $x$ ,  $y$  and  $z$  of a point on the surface are the function of two surface parameters  $\theta^1$  and  $\theta^2$ . Basis functions are used to either fit or approximate a finite number of nodal positions. Hence in CAD control points and their positions are the handles to create and modify geometry. In general a surface  $\mathbf{S}$  in parametric representation can be determined through

$$\mathbf{S}(\theta^1, \theta^2) = f(\theta^1, \theta^2, \mathbf{P}_i, c_j), \quad (2.18)$$

where  $\mathbf{P}_i$  are the control point positions and  $c_j$  are possible additional parameters like weights for the individual control points. As an example a parametric description of a NURBS-based surface is given in Equation (2.26).

### Spatial discretization

The concept of spatial discretization is at the core of the finite element method (FEM), see Bathe [10], Belytschko et al. [18], Hughes [74], Strang et al. [135], and Zienkiewicz et al. [152]: the functional spaces for the description of the different fields – e.g. geometry, displacements, stresses – are approximated by finite elements with their locally confined basis functions. Following the isoparametric paradigm (see Strang et al. [135] and Zienkiewicz et al. [152]) the solution field is expressed through the same ansatz as the geometry itself.

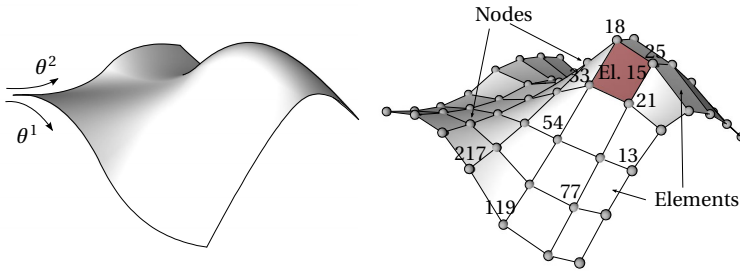
Within the spatial discretization, the continuous surface  $\mathbf{S}$  is then represented by  $n_{\text{ele}}$  non-overlapping sub-domains  $\Omega_e$  (the finite elements) by

$$\mathbf{S} \approx \mathbf{S}_h = \bigcup_{e=1}^{n_{\text{ele}}} \Omega_e, \quad (2.19)$$

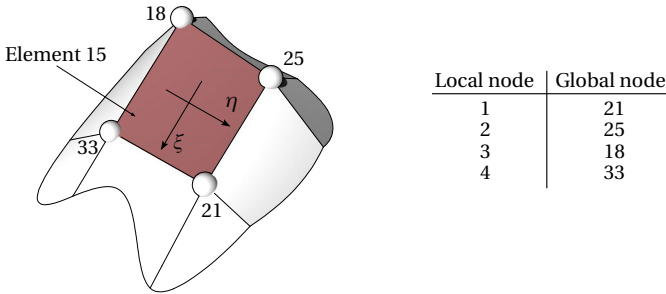
where the subscript h is used to indicate the approximative character, represented in Figure 2.4(a). This geometry transformation from the original, continuous geometry  $\mathbf{S}$  to the discretized geometry  $\mathbf{S}_h$  is called *meshing*, see Coll Sans [43] and Topping [142].

With the concept of classical finite element analysis (FEA), it is possible to reduce the unknown fields to discrete quantities in the nodes of the elements. The unknown spatial fields are now approximated within the elements by locally confined basis functions among which low order (linear,

## 2 Fundamentals



(a) Continuous surface and spatial discretization with bi-linear quad-mesh



(b) Element of the mesh from (a) with global nodes and local parameters and node numbers

**Figure 2.4:** Spatial discretization of a surface with a low-order (bi-linear) polynomial quad-mesh and global and local nodes

quadratic) Lagrange polynomial shape functions are the most commonly used, see Figure 2.5. As an example the approximated displacement field  $\mathbf{u}_h$  is expressed within the element as

$$\mathbf{u}_h = \mathbf{u}_h(\xi, \eta) = \sum_{i=1}^{n_{\text{nodes}}} N_i(\xi, \eta) \hat{\mathbf{u}}_i. \quad (2.20)$$

Here  $\xi$  and  $\eta$ , introduced in Figure 2.4(b), identify the local parameters within the element<sup>2</sup>,  $N_i$  is the basis function corresponding to node  $i$  of

<sup>2</sup> Here the parameters  $(\xi, \eta)$  are introduced instead of the priorly used  $(\theta^1, \theta^2)$ : Thus a difference is made between the parameters of the geometric description,  $(\theta^1, \theta^2)$ , spreading

## 2.1 Basics of geometry and its description

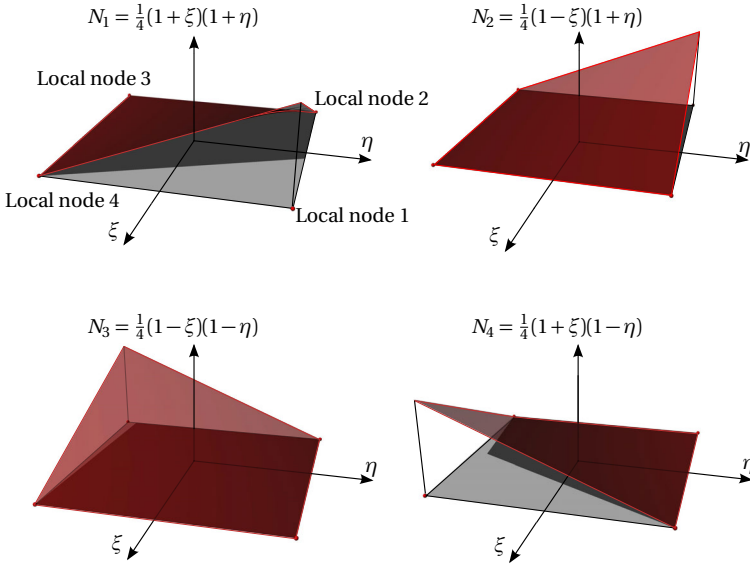


**Figure 2.5:** Bi-linear shape functions and parameterlines for the spatial discretization from Figure 2.4

the element and  $\hat{\mathbf{u}}_i$  are the discrete nodal displacements at node  $i$ . The same principle is applied to all occurring fields, including the geometry itself.

The quality of the approximation can generally be improved by refinement, *i.e.* either increasing the number of elements ( $h$ -method) or using higher-valued shape functions ( $p$ -method), see Hughes [74] and Zienkiewicz et al. [152].

In analogy to Equation (2.20) the geometry  $\mathbf{X}$  within a finite element is approximated as

$$\mathbf{X} \approx \mathbf{X}_h(\xi, \eta) = \sum_{i=1}^{n_{\text{nodes}}} N_i(\xi, \eta) \hat{\mathbf{X}}_i, \quad (2.21)$$

through the whole surface, and those corresponding to each individual finite element,  $(\xi, \eta)$ , confined within the element, see also Figure 2.4(a).

where  $\hat{\mathbf{X}}_i$  are the discrete nodal positions. In consequence the base vectors  $\mathbf{A}_\alpha$  from Equations (2.1) and (2.2) are then computed as

$$\mathbf{A}_{1h} = \frac{\partial \mathbf{X}_h}{\partial \xi} = \sum_{i=1}^{n_{\text{nodes}}} N_{i,1} \hat{\mathbf{X}}_i \quad \text{resp.} \quad \mathbf{A}_{2h} = \frac{\partial \mathbf{X}_h}{\partial \eta} = \sum_{i=1}^{n_{\text{nodes}}} N_{i,2} \hat{\mathbf{X}}_i. \quad (2.22)$$

Further required entities of differential geometry can then be derived from these approximated base vectors  $\mathbf{A}_{ih}$ . Obviously the approximation by piecewise low order polynomial shape functions leads to a reduction of continuity as can be seen in Figure 2.4(a). Hence, as a consequence of the meshing, some entities like curvature properties or discrete surface normals need to be approximated by adapted approaches, as they are discussed *e.g.* in Linhard [88] and Wakefield [146]. For ease of reading in the remainder of this thesis the subscript h, indicating the approximated quantities, will be skipped if the context allows to do so.

An alternative approach to approximate geometry and solution fields lies in directly using the basis functions from CAD, as is presented in the following section.

## 2.2 NURBS-based B-Rep models

As an alternative to classical facet-type discretization (see Figure 2.5), which is predominant in contemporary CAE-systems (Computer-Aided Engineering), CAD often relies on NURBS-based B-Rep models. Figure 2.6 shows a prototypic example for such a NURBS-based B-Rep model, which is composed out of trimmed NURBS surfaces. The fundamentals for this type of geometry description and related implications are presented in the following.

Note that this section only intends to give a brief introduction. Further reading and more complete information may be found *e.g.* in Breitenberger [32], Cottrell [45], Hughes et al. [73], and Piegl et al. [120].

### 2.2.1 NURBS, NURBS curves and NURBS surfaces

*Non-Uniform Rational B-Splines* (NURBS) are the underlying geometry description for B-Rep models applied in many contemporary CAD systems, see *e.g.* Piegl et al. [120]. The term "non-uniform" refers to the knot vector

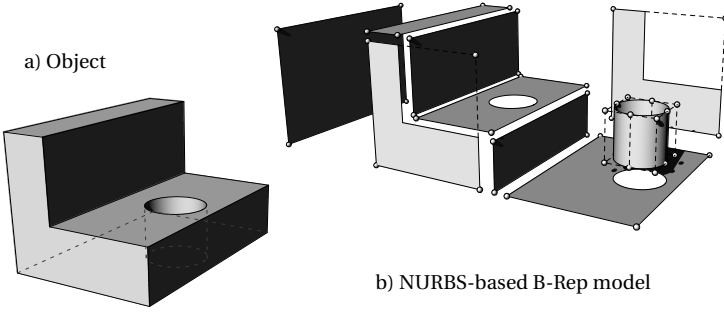


**Figure 2.6:** NURBS-based B-Rep model as composition of trimmed NURBS surfaces (multi-patch) (remade after Choi [42])

$\Xi = [\xi_1, \xi_2, \dots, \xi_{n+p+1}]$  that can be non-uniformly defined while the term "rational" refers to the basis function definition.

### NURBS curves

Mathematically NURBS curves are defined as

$$\mathbf{C}(\xi) = \sum_{i=1}^n \frac{N_{i,p}(\xi)w_i}{\sum_{k=1}^n N_{k,p}(\xi)w_k} \mathbf{P}_i = \sum_{i=1}^n R_{i,p}(\xi) \mathbf{P}_i, \quad (2.23)$$

where the NURBS basis functions  $R_{i,p}(\xi)$  of polynomial degree  $p$  consist of the B-Spline basis functions  $N_{i,p}(\xi)$  and  $\xi$  is the parametric coordinate of the curve, see Figure 2.7. Each control point  $\mathbf{P}_i$  has an additional weight  $w_i$  that allows to control the influence of the individual point on the curve.

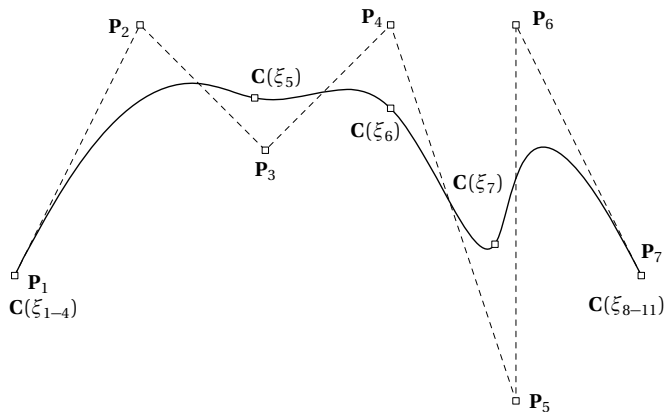
In contrast to linear shape functions, the control points  $\mathbf{P}_i$  are generally not interpolating, *i.e.* they are not located within the geometry they describe, as illustrated in Figure 2.7.

### Basis functions

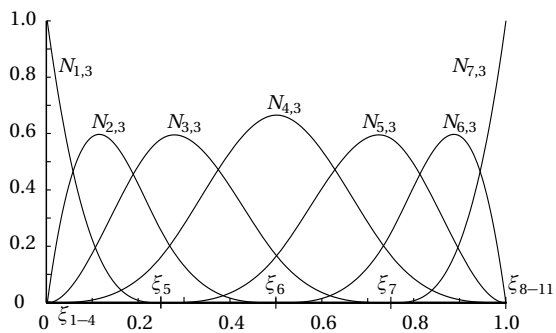
The B-Spline basis functions  $N_{i,p}$  are computed starting from  $p = 0$  as

$$N_{i,0}(\xi) = \begin{cases} 1 & \text{for } \xi_i \leq \xi < \xi_{i+1} \\ 0 & \text{otherwise} \end{cases}, \quad (2.24)$$

## 2 Fundamentals



(a) B-Spline curve in the 2D-space with its control points  $P_i$ , the control point polygon (dashed lines) and corresponding knot positions on the curve



(b) Corresponding basis functions  $N_{i,p}$  in the parameter space

**Figure 2.7:** Cubic B-Spline curve with a clamped knot vector  $\Xi = [0, 0, 0, 0, 0.25, 0.5, 0.75, 1, 1, 1, 1]$  (leading to interpolating control points  $P_1$  and  $P_7$ ) and corresponding basis functions

while for  $p \geq 1$  they are defined as

$$N_{i,p}(\xi) = \frac{\xi - \xi_i}{\xi_{i+p} - \xi_i} N_{i,p-1}(\xi) + \frac{\xi_{i+p+1} - \xi}{\xi_{i+p+1} - \xi_{i+1}} N_{i+1,p-1}(\xi). \quad (2.25)$$

Inside a knot span the basis functions  $N_{i,p}(\xi)$  are  $C^\infty$ -continuous. The continuity across knots depends on the multiplicity  $k$  of the knot and is determined to be  $C^{p-k}$ , see also Piegl et al. [120].

B-Spline basis functions have important characteristics, especially w.r.t. their usage as basis functions for element formulations (see also Hughes et al. [73]):

- Partition of unity, *i.e.*  $\sum_{i=1}^n N_{i,p}(\xi) = 1$
- Local support, *i.e.* the support is contained in the interval  $[\xi_i, \xi_{i+p+1}]$
- Non-negativity, *i.e.*  $N_{i,p}(\xi) \geq 0$
- Linear independence, *i.e.*  $\sum_{i=1}^n \alpha_i N_{i,p}(\xi) = 0 \Leftrightarrow \alpha_j = 0, j = 1, 2, \dots, n$

### Geometry refinement

Another important aspect of B-Spline resp. NURBS geometries is related to their capabilities of geometry refinement: Refinement is possible without altering the initial geometry, but nevertheless increasing the number of control points. This aspect is especially important for the representation of solution fields, when B-Spline resp. NURBS are applied as basis functions for FEA. Different refinement strategies have been developed which are classified as

- *knot insertion*, the analog of  $h$ -refinement: By inserting knots new control points are introduced and the continuity may be reduced if knots are repeated;
- *order elevation*, the analog of  $p$ -refinement: It consists in increasing the polynomial degree of the basis functions while preserving the continuity through repetition of knots;
- combination of knot insertion and order elevation: This combination of the other two strategies is referred to as *k-refinement*. It allows for a more homogeneous structure in the refined level.

For more details on the refinement, the reader is referred to Cottrell [45], Hughes et al. [73], and Piegl et al. [120].

### NURBS surfaces

Analogously to the definition of the curve in Equation (2.23) a NURBS surface  $\mathbf{S}$  as illustrated in Figure 2.8 is defined by the tensor product structure of its basis functions as

$$\begin{aligned} \mathbf{S}(\xi, \eta) &= \sum_{i=1}^n \sum_{j=1}^m \frac{N_{i,p}(\xi)M_{j,q}(\eta)w_{ij}}{\sum_{k=1}^n \sum_{l=1}^m N_{k,p}(\xi)M_{l,q}(\eta)w_{kl}} \mathbf{P}_{ij} \\ &= \sum_{i=1}^n \sum_{j=1}^m R_{ij,pq}(\xi, \eta) \mathbf{P}_{ij}, \end{aligned} \quad (2.26)$$

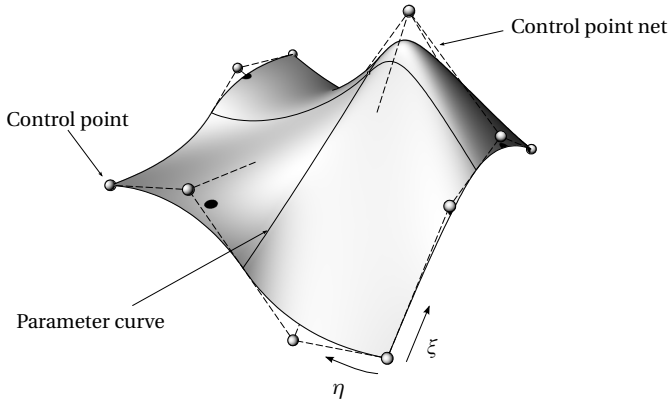
where  $\xi$  and  $\eta$  are the two parametric dimensions,  $m \times n$  is the net of control points, and  $p$  and  $q$  are the respective polynomial degrees of the corresponding basis functions  $N_{i,p}(\xi)$  and  $M_{j,q}(\eta)$ .

These NURBS surfaces are able to exactly represent many technically relevant geometric primitives like conic sections. Nevertheless, an exact geometry representation is still only possible for geometries which are within the function space. This aspect will be treated in Section 2.2.5 and exemplified in Section 3.4.2.

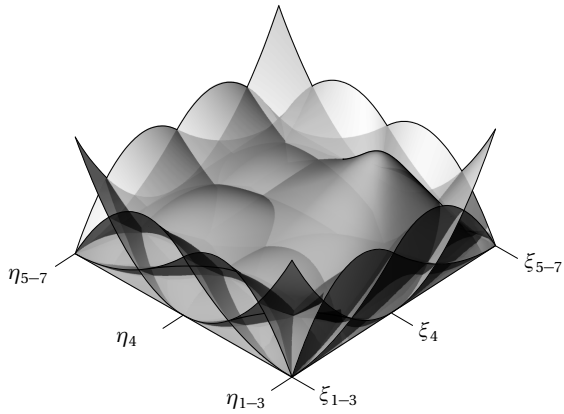
### 2.2.2 Trimmed surfaces and the trimming operation

Trimming refers to the operation of creating trimmed surfaces, *i.e.* surfaces that are based on a complete patch where parts are "cut off" or holes are "cut out". The result of this trimming operation is a partially visible surface, defined by a trimmed domain  $\mathcal{D}$  in the parameter space. In Figure 2.9 an example of a trimmed surface with a hole is illustrated.

The trimming curves  $\tilde{\mathbf{C}}(\tilde{\xi})$ , *i.e.* the separators between visible and non-visible resp. active and non-active parts of the surface, are defined in the parameter space of the surface with their counterpart  $\mathbf{C}(\tilde{\xi})$  in the geometry space. Here  $\tilde{\xi}$  is the parametric coordinate of the curve. The geometric definition of the trimming curves is based on the intersection of geometric entities. Through this intersection the representation of the curve in the parameter space of the surface to be trimmed is determined.



(a) NURBS surface with an increased weight  $w_{ij}$  of the top control point, pulling up the surface



(b) Corresponding NURBS basis functions in the parameter space

**Figure 2.8:** Quadratic NURBS surface with clamped knot vectors  $\Xi = \mathbf{H} = [0, 0, 0, 0.5, 1, 1, 1]$  and its basis functions

## 2 Fundamentals

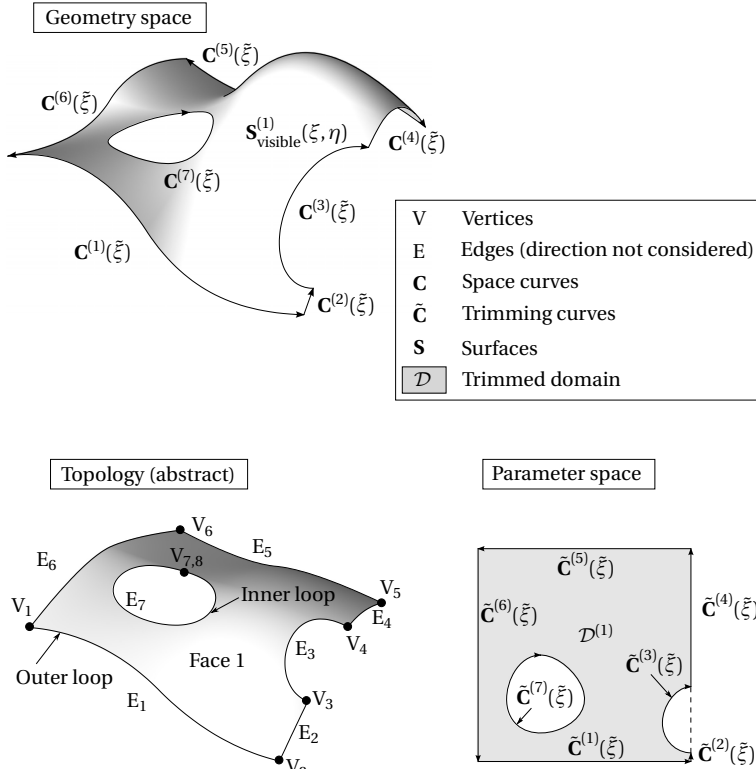


**Figure 2.9:** B-Rep description of a spatial surface with a hole: The NURBS-based surface is bounded by trimming curves  $\tilde{C}(\xi)$  in the parameter space, with their corresponding geometrical curves  $C(\xi)$  on the surface  $S$ . The trimming curves  $\tilde{C}(\xi)$  are joined properly to form outer (counter-clockwise oriented) and inner (clockwise oriented) trimming loops, respectively.

In computer-aided architectural geometry, different geometry descriptions are used, see Pottman et al. [122]. Among those notably the *sub-division surfaces* should be mentioned which are increasingly used in modern architectural design tools owing to their ease of handling and the great topological freedom they provide. However, for computationally oriented approaches to geometries the standard model for the description of trimmed surfaces in contemporary CAD systems is a NURBS-based *Boundary-Representation* (B-Rep) model, see Hoffmann [71], Mäntylä [93], and Stroud [137], which is described in the following section.

### 2.2.3 Boundary Representation (B-Rep)

An unbounded NURBS surface is described by the tensor product structure of the NURBS basis functions, see Equation (2.26). By adding a description of the boundary, the limitations of this tensor product w.r.t an arbitrary number of edges or the representation of holes can be overcome, see Figure 2.9.

The *Boundary-Representation* (B-Rep) is a technique used in CAD to describe arbitrary geometrical entities. For a three dimensional object a set of adjacent bounded surface elements called *faces* (F) describes the "skin" of the object and thus the object itself, see Stroud [137]. The faces at their turn are bounded by sets of *edges* (E) which are curves lying on the surface of the faces. Several edges meet in points that are called *vertices* (V). The geometric counterparts to these topology entities F, E, and V are surfaces (S), curves (C) and points (P), respectively. Expressed in the parameter space of the surface, the curves are referred to as  $\tilde{C}(\tilde{\xi})$ . These entities are represented in Figure 2.9.

By also interpreting the original boundaries of the underlying patch as trimming curves, in the B-Rep description a trimmed surface is completely enclosed by trimming curves  $\tilde{C}(\tilde{\xi})$  in the parameter space. These trimming curves are joined properly to form outer (oriented counter-clockwise) and inner (oriented clockwise) trimming loops. Thus the B-Rep description of the trimmed surface in Figure 2.9 consists of the NURBS-based surface description and the outer and – if applicable – the inner trimming loop.

As illustrated in Figure 2.6, these trimmed surfaces are then combined to so-called multi-patch geometries, which form complete NURBS based B-Rep models.

### 2.2.4 Integration procedure

As introduced by Breitenberger [32], the integration over the trimmed NURBS surface is done knot span (element) wise by applying a Gaussian quadrature rule. If required as a consequence of trimming, the Gauss-space is adapted in order to fit to the trimmed surface domain according to the *Adaptive Gaussian Integration Procedure* [32]. Within this adapted Gauss-space a standard integration procedure, as presented *e.g.* in Cottrell [45] and Hughes et al. [73] can be applied.

As an example for the integration of NURBS-based B-Rep models, the area of a knot span is given as

$$|A| = \int_A dA = \int_{\mathcal{G}} J_1 J_2 d\mathcal{G}, \quad (2.27)$$

where  $\mathcal{G} \in [-1, 1] \times [-1, 1]$  is the Gaussian space and  $J_a$  indicates the Jacobians for the respective mapping operations.  $J_1$  represents the mapping from the geometry space in  $\mathbb{R}^3$  to the parameter space  $\mathcal{D} \in \mathbb{R}^2$ . Using the base vectors  $\mathbf{A}_a$ ,  $J_1$  can be computed as

$$J_1 = \|\mathbf{A}_1 \times \mathbf{A}_2\|. \quad (2.28)$$

$J_2$  at its turn represents the mapping from the parameter space  $\mathcal{D}$  to the Gaussian space  $\mathcal{G}$ . The Jacobian  $J_2$  can be determined as

$$J_2 = \frac{\partial \xi}{\partial \xi_{\mathcal{G}}} \frac{\partial \eta}{\partial \eta_{\mathcal{G}}}, \quad (2.29)$$

where  $\xi$  and  $\eta$  are the parameters in the parameter space and  $\xi_{\mathcal{G}}$  and  $\eta_{\mathcal{G}}$  describe the Gaussian space.

For the numerical integration, a standard Gauss quadrature is applied:

$$|A| \approx \sum_{l=0}^{n_g} J_1(\xi_l, \eta_l) J_2(\xi_l, \eta_l) w_l = \sum_{l=0}^{n_g} J_1(\xi_l, \eta_l) \tilde{w}_l, \quad (2.30)$$

where  $n_g$  is the number of quadrature points for each knot span and  $w_l$  are the corresponding quadrature weights. Since  $J_2$  is deformation independent, it can be pre-evaluated and thus the modified quadrature weight  $\tilde{w}_l$  applied in Equation (2.30) can be defined as  $\tilde{w}_l = J_2 w_l$ .

For a more in-depth description of the integration procedure and its implementation, refer to Breitenberger [32].

### **2.2.5 Exact geometry representation in IGA in the context of mechanically motivated surfaces**

The *isogeometric analysis* (IGA), which will be presented in detail in Chapter 3, refers to NURBS as basis functions for the analysis. One often cited feature of IGA is the exactness of the geometry representation through the use of NURBS, see *e.g.* Bazilevs et al. [16], Cottrell et al. [46], and Hughes et al. [73]. This exactness is valid for geometrically defined CAD-based structures, *i.e.* structures that are constructed out of the primitives that are available within the CAD-representation. In this context NURBS allow for significantly more geometric entities to be represented exactly, compared to standard linear or polynomial shape functions.

In general, solution fields cannot exactly be expressed with the same basis functions as the reference geometry. This also holds for NURBS discretizations, although – as for any discretization – refinement evidently improves the approximation of the solution field, without disturbing the quality of the initial geometry description, see Bazilevs et al. [16] and Beirão da Veiga et al. [17].

The shape of mechanically motivated surfaces such as minimal surfaces or hanging shapes in a certain sense already is a solution field. Thus – in contrast to geometrically motivated surfaces – the geometry of mechanically motivated surfaces is not necessarily within the function space of CAD parameterizations like NURBS. This approximating characteristic of a NURBS-based geometry description will be investigated in Section 3.4.2.

## **2.3 Structural mechanics for finite displacements**

In this section necessary fundamentals of structural mechanics for the analysis of lightweight structures shall briefly be introduced. Hereby the focus lies on the consideration of finite displacements since in the form-finding (see Section 2.5.3) and in the analysis of lightweight structures large deformations occur, requiring a geometrically non-linear description.

### **2.3.1 Kinematics**

The analysis of structures is based on the observation of their deformation process. This kinematic description introduces further assumptions,

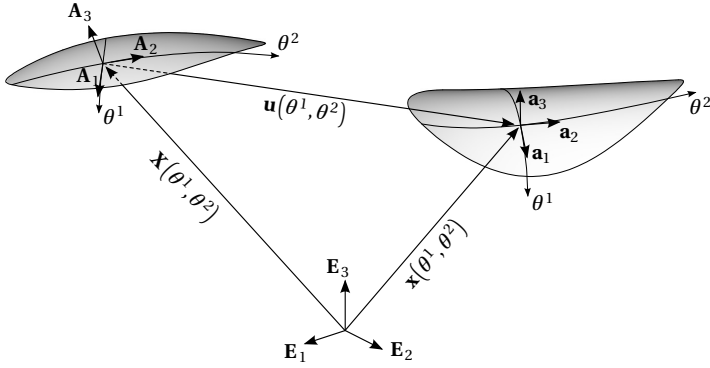


**Figure 2.10:** Schematic representation of the reference and the current configuration  $\mathbf{X}$  and  $\mathbf{x}$  with their respective base vectors  $\mathbf{A}_j$  and  $\mathbf{a}_j$  as well as the displacement vector  $\mathbf{u} = \mathbf{x} - \mathbf{X}$

models and simplifications to those already introduced in the geometry description. The main concept lies in the comparison of an initial, undeformed reference configuration  $\mathbf{X}$  and a deformed current configuration  $\mathbf{x}$  that will be introduced in the sequel.

Note that this brief introduction can only provide some selected aspects. For a more complete representation and deeper insight, a vast amount of literature exists. This section as well as parts of the notation are mainly based on Belytschko et al. [18], Holzapfel [72], and Parisch [110].

### Deformations, configurations and deformation gradient

The deformation  $\mathbf{u}$  of a surface structure is expressed by the displacement of its mid-surface (see Figure 2.1) as defined by the difference of positions of the current configuration  $\mathbf{x}$  and the reference configuration  $\mathbf{X}$ :

$$\mathbf{u} = \mathbf{u}(\theta^1, \theta^2, \theta^3 = 0) = \mathbf{x}_{\text{mid-surface}} - \mathbf{X}_{\text{mid-surface}} = \mathbf{x}(\theta^1, \theta^2) - \mathbf{X}(\theta^1, \theta^2) \quad (2.31)$$

A representation of the configurations  $\mathbf{X}$  and  $\mathbf{x}$ , the displacement vector  $\mathbf{u}$  and the corresponding base-vectors is given in Figure 2.10.

The deformation process can be described using the covariant base vectors in the current configuration  $\mathbf{g}_i = \partial \mathbf{x} / \partial \theta^i = \mathbf{x}_{,i}$  and the contravariant base vectors in the reference configuration  $\mathbf{G}^i = \partial \theta^i / \partial \mathbf{X}$ , see Equations (2.1) and (2.5), to formulate the deformation gradient  $\mathbf{F}$  which links the reference configuration to the deformed configuration:

$$\mathbf{F} = \frac{\partial \mathbf{x}}{\partial \mathbf{X}} = \mathbf{g}_i \otimes \mathbf{G}^i \quad (2.32)$$

The determinant of  $\mathbf{F}$  can be expressed as

$$\det[\mathbf{F}] = \frac{da}{dA} = \sqrt{\frac{\det[g_{\alpha\beta}]}{\det[G_{\alpha\beta}]}} \quad (2.33)$$

linking the surface areas  $dA$  and  $da$  in the undeformed resp. deformed configuration, see Equation (2.9), by means of the metric tensor, see Equation (2.6).

### Strain measures

As strain measure the *Green-Lagrange* (GL) strain tensor  $\mathbf{E}$  is mostly used within this thesis:

$$\mathbf{E} = \frac{1}{2}(\mathbf{F}^T \cdot \mathbf{F} - \mathbf{I}) = E_{ij} \mathbf{G}^i \otimes \mathbf{G}^j \quad (2.34)$$

where  $\mathbf{I}$  denotes the identity tensor. The coefficients  $E_{ij}$  are determined as

$$E_{ij} = \frac{1}{2}(g_{ij} - G_{ij}) \quad (2.35)$$

In membrane theory, the thickness  $t$  is considered very small, such that contributions of  $\theta^3$  may be set to zero in this context, see Basar et al. [9] and Bischoff et al. [21]. Hence the local basis  $\mathbf{A}_i$  refers to the continuum base vectors  $\mathbf{G}_i$ . It is further implied that transverse strain components are zero, *i.e.*  $E_{i3} = E_{3i} = 0$ . Thus the components of the GL strain tensor  $\mathbf{E}$  in Equation (2.35) can be written as

$$E_{\alpha\beta} = \frac{1}{2}(a_{\alpha\beta} - A_{\alpha\beta}) = \epsilon_{\alpha\beta} \quad (2.36)$$

in order to align with classical definitions. Here the membrane strain coefficients  $\epsilon_{\alpha\beta}$  are introduced in order to distinguish the membrane strains from the general case.

The related strain measure based in the current configuration is the *Euler-Almansi* strain tensor

$$\mathbf{e} = e_{ij} \mathbf{g}^i \otimes \mathbf{g}^j, \quad (2.37)$$

where the coefficients  $e_{ij}$  are the same as the coefficients  $E_{ij}$  of the GL strains, see Equation (2.35).

### 2.3.2 Stresses and material law

As energetically conjugated stress measure to the GL strains, the *2<sup>nd</sup> Piola-Kirchhoff* (PK2) stress tensor  $\mathbf{S}$  is introduced. The coefficients of the elastic stresses  $\mathbf{S}_{\text{elast}}$  can be identified as the in-plane normal stresses  $S^{11}$ ,  $S^{22}$ , and the in-plane shear stress  $S^{12}$  resp.  $S^{21}$  through the constitutive equation

$$\mathbf{S}_{\text{elast}} = S_{\text{elast}}^{\alpha\beta} \mathbf{G}_\alpha \otimes \mathbf{G}_\beta = \mathbb{C} : \mathbf{E}, \quad (2.38)$$

where  $\mathbb{C} = C^{\alpha\beta\gamma\delta} \mathbf{G}_\alpha \otimes \mathbf{G}_\beta \otimes \mathbf{G}_\gamma \otimes \mathbf{G}_\delta$  is the fourth order elasticity tensor. The coefficients  $S_{\text{elast}}^{\alpha\beta}$  of the PK2 stress tensor are determined as

$$S_{\text{elast}}^{\alpha\beta} = C^{\alpha\beta\gamma\delta} \epsilon_{\gamma\delta}. \quad (2.39)$$

Within this thesis the *St. Venant-Kirchhoff* (StVK) material model, which is characterized by Young's modulus  $E$  and Poisson's ratio  $\nu$ , will be applied. Using the convective curvilinear basis, the coefficients of the elasticity tensor  $\mathbb{C}_{\text{StVK}}$  are determined as

$$C_{\text{StVK}}^{\alpha\beta\gamma\delta} = \frac{E\nu}{1-\nu^2} G^{\alpha\beta} G^{\gamma\delta} + \frac{E}{2(1+\nu)} (G^{\alpha\gamma} G^{\beta\delta} + G^{\alpha\delta} G^{\beta\gamma}). \quad (2.40)$$

Referring to a local Cartesian basis and applying Voigt-notation, the St. Venant-Kirchhoff material law can then be simplified to

$$\begin{bmatrix} \bar{S}_{\text{elast}}^{11} \\ \bar{S}_{\text{elast}}^{22} \\ \bar{S}_{\text{elast}}^{12} \end{bmatrix} = \frac{E}{1-\nu^2} \begin{bmatrix} 1 & \nu & 0 \\ \nu & 1 & 0 \\ 0 & 0 & \frac{1-\nu}{2} \end{bmatrix} \cdot \begin{bmatrix} \bar{\epsilon}_{11} \\ \bar{\epsilon}_{22} \\ 2\bar{\epsilon}_{12} \end{bmatrix} = \bar{\mathbb{C}}_{\text{StVK}} \cdot \bar{\boldsymbol{\epsilon}}. \quad (2.41)$$

Note that the St. Venant-Kirchhoff material model as the spatial generalization of Hooke's material law is only suited for the description of small strains. More sophisticated material models accounting for moderate to large strains and anisotropy can be found *e.g.* in Holzapfel [72] and Ogden [108].

Whereas the PK2 stress tensor  $\mathbf{S}$  refers to the reference configuration, the energetically conjugate to the Euler-Almansi strains, see Equation (2.37), is the *Cauchy* stress tensor

$$\boldsymbol{\sigma} = \sigma^{\alpha\beta} \mathbf{g}_\alpha \otimes \mathbf{g}_\beta . \quad (2.42)$$

The Cauchy stresses act in the current configuration and hence express the "true physical stresses" (Parisch [110]). The two stress measures are linked through

$$\mathbf{S} = \det[\mathbf{F}] \mathbf{F}^{-1} \cdot \boldsymbol{\sigma} \mathbf{F}^{-T} = \det[\mathbf{F}] \sigma^{\alpha\beta} \mathbf{G}_\alpha \otimes \mathbf{G}_\beta = S^{\alpha\beta} \mathbf{G}_\alpha \otimes \mathbf{G}_\beta , \quad (2.43)$$

from which the components of the PK2 stress tensor can be identified as

$$S^{\alpha\beta} = \det[\mathbf{F}] \sigma^{\alpha\beta} . \quad (2.44)$$

Another common stress measure is the *first Piola-Kirchhoff* (PK1) stress tensor  $\mathbf{P}$ , which is obtained by

$$\mathbf{P} = \det[\mathbf{F}] \cdot \boldsymbol{\sigma} \cdot \mathbf{F}^{-T} = \mathbf{F} \cdot \mathbf{S} = P^{\alpha\beta} \mathbf{g}_\alpha \otimes \mathbf{G}_\beta . \quad (2.45)$$

It is based in both the current and the reference configuration and hence is non-symmetric.

### 2.3.3 Equilibrium

Equilibrium is fulfilled, when internal and external forces are in balance. For a static problem, *i.e.* neglecting dynamic effects, this state is expressed in the reference configuration through

$$\operatorname{div} \mathbf{P} + \rho_0 \mathbf{B} = \mathbf{0} , \quad (2.46)$$

where  $\mathbf{P}$  represents the stress state in the body through the PK1 stress tensor, see Equation (2.45),  $\rho_0$  is the density of the body and  $\mathbf{B}$  is the vector

of body forces, both in the reference configuration. The corresponding formulation in the current configuration is

$$\operatorname{div} \boldsymbol{\sigma} + \rho \mathbf{b} = \mathbf{0}, \quad (2.47)$$

where now  $\boldsymbol{\sigma}$  represents the stress state in the body through the Cauchy stress tensor, see Equation (2.42),  $\rho$  is the density of the body and  $\mathbf{b}$  is the vector of body forces (see Basar et al. [9], Wunderlich et al. [151], and Zienkiewicz et al. [152] for more details).

The relation from Equations (2.46) resp. (2.47) has to be fulfilled everywhere in the structure including the boundaries. This is referred to as the *strong form* of equilibrium. Since in general a closed-form solution to spatial problems cannot be found, discretization methods like the finite element method (FEM) are employed. Here the field equations are no longer satisfied point-wise, but in an integral sense. This leads to the *weak form* of the equilibrium problem, commonly formulated through the principle of virtual work (see Wunderlich et al. [151]):

$$\delta W = \delta W_{\text{int}} + \delta W_{\text{ext}} = 0 \quad (2.48)$$

The internal and external contributions to the virtual work are defined as

$$-\delta W_{\text{int}} = \int_{\Omega_0} \mathbf{S} : \delta \mathbf{E} \, d\Omega_0 = \int_{\Omega} \boldsymbol{\sigma} : \delta \mathbf{e} \, d\Omega \quad (2.49)$$

and

$$\begin{aligned} \delta W_{\text{ext}} &= \int_{\Gamma_0} \mathbf{T} \cdot \delta \mathbf{u} \, d\Gamma_0 + \int_{\Omega_0} \rho_0 \mathbf{B} \cdot \delta \mathbf{u} \, d\Omega_0 \\ &= \int_{\Gamma} \mathbf{t} \cdot \delta \mathbf{u} \, d\Gamma + \int_{\Omega} \rho \mathbf{b} \cdot \delta \mathbf{u} \, d\Omega, \end{aligned} \quad (2.50)$$

where  $\Omega_0$  and  $\Omega$  represent the structural domain in the reference and current configuration, respectively, and  $\Gamma_0$  and  $\Gamma$  are the corresponding domain boundaries.  $\mathbf{T}$  and  $\mathbf{t}$  are the respective vectors of forces applied on the boundary in the two configurations. The virtual strains  $\delta \mathbf{E}$  and  $\delta \mathbf{e}$  arise from the virtual displacement field  $\delta \mathbf{u}$  which is applied to the structure. Equation (2.48) can be expressed through the variation of the internal and external work expression w.r.t. to  $\delta \mathbf{u}$  as

$$\delta W = \frac{\partial W}{\partial \mathbf{u}} \delta \mathbf{u} = 0. \quad (2.51)$$

### 2.3.4 Discretization and solution approach

By introducing the discretized displacement vector  $\mathbf{u}_h$  and an arbitrary virtual discretized displacement vector  $\delta \mathbf{u}_h$ , see Equation (2.20), a spatial discretization is applied, see Section 2.1.2. Hence the equilibrium expression from Equation (2.51) transforms to

$$\delta W = \frac{\partial W}{\partial \mathbf{u}_h} \delta \mathbf{u}_h = -\mathbf{R} \cdot \delta \mathbf{u}_h = 0. \quad (2.52)$$

Since the virtual displacements  $\delta \mathbf{u}_h$  are arbitrary, the residual force vector  $\mathbf{R}$  has to vanish in order to fulfill equilibrium.

#### Solution approach for the general discretized non-linear problem

The expression of the unbalanced forces  $\mathbf{R}$  in Equation (2.52) turns out to be non-linear for the general case, hence necessitating an iterative solution approach like the *Newton-Raphson* algorithm. The tangential stiffness matrix  $\mathbf{K}$  is introduced as the linearization of the unbalanced forces  $\mathbf{R}$ :

$$\text{LIN}(\mathbf{R}) = \mathbf{R} + \frac{\partial \mathbf{R}}{\partial \mathbf{u}_h} \Delta \mathbf{u}_h = \mathbf{R} + \mathbf{K} \Delta \mathbf{u}_h = \mathbf{0} \quad (2.53)$$

Thus in each iteration step, the system from Equation (2.53) is solved for the displacement increment  $\Delta \mathbf{u}_h$ . The stiffness  $\mathbf{K}$  and the residual  $\mathbf{R}$  are updated in consequence and used to solve the next inner iteration until convergence is achieved. Written in components, the definition of the vector of unbalanced forces  $\mathbf{R}$  and the stiffness matrix  $\mathbf{K}$  are identified as

$$R_r = -\frac{\partial W}{\partial u_r} = -\frac{\partial W_{\text{int}}}{\partial u_r} - \frac{\partial W_{\text{ext}}}{\partial u_r} = R_r^{\text{int}} + R_r^{\text{ext}}, \quad (2.54)$$

$$K_{rs} = \frac{\partial R_r}{\partial u_s} = -\frac{\partial^2 W}{\partial u_r \partial u_s} = -\frac{\partial^2 W_{\text{int}}}{\partial u_r \partial u_s} - \frac{\partial^2 W_{\text{ext}}}{\partial u_r \partial u_s} = K_{rs}^{\text{int}} + K_{rs}^{\text{ext}}, \quad (2.55)$$

where  $\{r, s\} = 1, \dots, n_{\text{DOF}}$  denote the respective degrees of freedom (DOFs).

#### Determination of the discrete quantities

Applying the discretization to the virtual work expressions from Equations (2.49) and (2.50) allows identifying the individual contributions to the residual force vector  $\mathbf{R}$  and the corresponding stiffness matrix  $\mathbf{K}$ .

In the reference configuration one can identify

$$R_r = \int_{\Omega_0} (\mathbf{S} : \mathbf{E}_{,rs}) d\Omega_0 - \int_{\Gamma_0} (\mathbf{T} \cdot \mathbf{u}_{,r}) d\Gamma_0 - \int_{\Omega_0} \rho_0 \mathbf{B} \cdot \mathbf{u}_{,r} d\Omega_0, \quad (2.56)$$

where the first integral represents the internal contributions  $R_r^{\text{int}}$  and the other two integrals represent  $R_r^{\text{ext}}$ . The right-hand side vector of unbalanced forces  $\mathbf{F}$  is defined as  $\mathbf{F} = -\mathbf{R}$  resp. in components  $F_r^{\text{int}} = -R_r^{\text{int}}$  and accordingly  $F_r^{\text{ext}} = -R_r^{\text{ext}}$ .

For the case of deformation-independent external forces  $\mathbf{T}$ , the external contribution  $K_{rs}^{\text{ext}}$  to the stiffness matrix vanishes and hence

$$K_{rs} = K_{rs}^{\text{int}} = R_{rs}^{\text{int}} = \int_{\Omega_0} (\mathbf{S}_{,s} : \mathbf{E}_{,r} + \mathbf{S} : \mathbf{E}_{,rs}) d\Omega_0. \quad (2.57)$$

An in-depth discussion of the contribution of deformation-dependent loads, *e.g.* surface pressure, can be found in Jrusjrunkiat [77], Rumpel et al. [125], and Schweizerhof et al. [132].

Based on the definition of the strain tensor  $\mathbf{E}$  and the stress tensor  $\mathbf{S}$  in Equations (2.36) and (2.39), respectively, together with the definition of the discretized base vectors  $\mathbf{G}_i$  and  $\mathbf{g}_i$ , see Equation (2.22), the required components for the determination of  $\mathbf{R}$  and  $\mathbf{K}$  can now be determined as a function of the discrete nodal displacements  $\hat{\mathbf{u}}$ .

## 2.4 Characteristics of geometrically non-linear beam elements

Beam elements are among the most widely used elements, especially in structural engineering. Based on a dimension reduction, see Figure 2.1, and possibly a homogenization (*e.g.* in the case of reinforced concrete members), beam element formulations can be used to model many parts of classical civil engineering structures.

Depending on the assumed beam-theory (following the Euler-Bernoulli assumption or Timoshenko shear-deformability, accounting for torsional warping, etc.) beam elements are classically formulated with 6 to 8 DOFs

per node<sup>3</sup> and provide the corresponding number of resultant forces. Usually these are: normal force  $N$ , bending moments  $M_y$  and  $M_z$ , torsional moment  $M_T$  (resp.  $M_x$ ) and shear forces  $V_y$  and  $V_z$ , where  $x$ ,  $y$  and  $z$  refer to the local axes of the beam element.

Under the assumption of small deformations and geometrically linear kinematics (referred to as *Theory of First Order*) beam element formulations can be considered established and generally provide satisfying and reliable results. However, the development of beam elements fully accounting for geometrical non-linearity is a challenging and still very active area of research, see *e.g.* the recent developments by Bauer et al. [14], Lumpe et al. [91], and Meier et al. [97].

In order to deal with moderate geometrical non-linearity and to assess stability problems, *Theory of Second Order* (abbr. Th.II.O.; also referred to as *second-order analysis*) has been developed. A strain measure  $\epsilon_{\text{Th.II.O.}}$ , suitable for moderate non-linear deformations, is used and equilibrium is established in the deformed configuration. In order to be accessible for manual calculation, further assumptions, notably the decoupling of bending and longitudinal deformation, have been introduced, see Lumpe et al. [91] and Petersen [112], forming different "sub-versions" of Th.II.O. Th.II.O. has been and still is successfully applied to a wide range of structures and provides the basis of many verification standards for geometrical non-linearity (*e.g.* in the Eurocodes, see Chapter 5). However, with increased computational possibilities and increasingly softer structures entailing larger deformations, Th.II.O. often is no longer suitable. For the present context of lightweight structures and more specifically the application in combination with structural membranes, two simplifications are in the focus: On the one hand, the strain measure  $\epsilon_{\text{Th.II.O.}}$  used in Th.II.O. is only applicable for small to moderate rotations, hence not for large deformations as they occur for the structures of interest. On the other hand, Th.II.O. (resp. its implementations in most available FE-environments) is not properly taking spatial deformations and their interaction into account, see Lumpe et al. [91]. Hence it can be stated that for the structures treated within this thesis – slender structures exhibiting large spatial deformations – Th.II.O. is not sufficient for reliable structural analyses.

---

<sup>3</sup> Note that within this thesis, the applied beam element formulation does not account for warping effects; the profiles that are used are considered warping free. In consequence, the beam elements need 6 DOFs per node and the listed resultant forces, see Section 2.4.3.

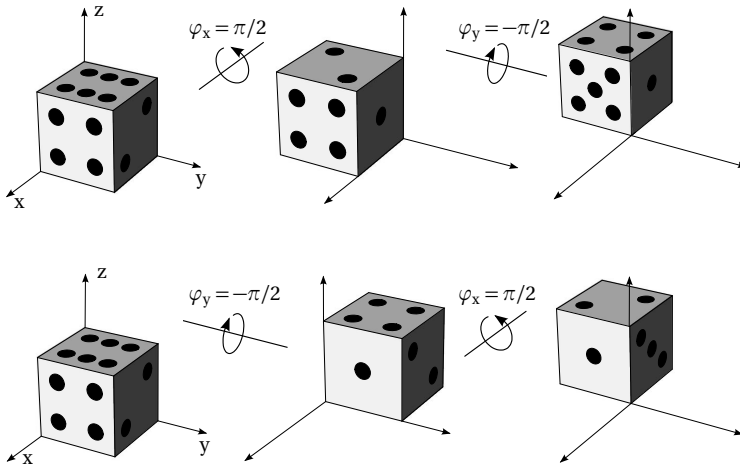


**Figure 2.11:** Non-commutativity of finite rotations with the example of a changed rotation sequence for rotations of a box around the x- and y-axis

As a basis for the developments and discussions within this thesis where bending active elements are included, some necessary fundamentals are presented in the following.

### 2.4.1 Finite rotations and their parameterization

One of the core aspects in the development of FE-formulations for spatial beam elements (as well as for shell elements) considering geometrically non-linear deformations is the treatment of finite rotations, *i.e.* rotations that cannot be considered "small" or even "moderate" any longer. Unlike rotations, displacements  $\mathbf{u}$  are added up over the load or iteration steps, *i.e.* the displacement at the load resp. iteration step  $(i + 1)$  is

$$\mathbf{u}^{(i+1)} = \mathbf{u}^{(i)} + \Delta\mathbf{u}^{(i)}. \quad (2.58)$$

In contrast, spatial rotations in general are *non-additive*, *i.e.* they cannot be determined as the sum of incremental rotations  $\Delta\varphi$ , see *e.g.* Crisfield [48] and Krenk [82]. Since the sequence of rotations is crucial for the result,

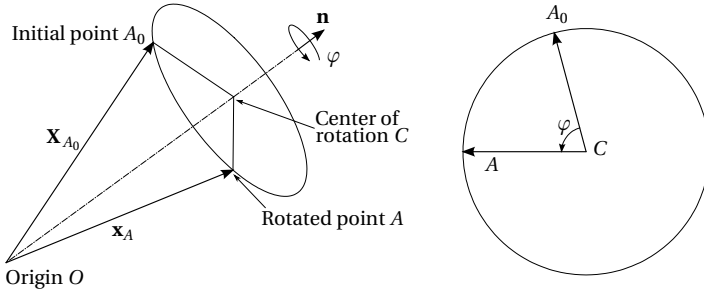


**Figure 2.12:** Spatial rotation of a point  $A$  by an angle  $\varphi$  around a rotation axis  $\mathbf{n}$  (remade based on [82])

the rotation "vector"  $\varphi$  in fact is a pseudo-vector, since it holds in general that for the combination of two rotations  $\varphi_1$  and  $\varphi_2$

$$\varphi_1 + \varphi_2 \neq \varphi_2 + \varphi_1, \quad (2.59)$$

which is referred to as *non-commutativity* [48, 82, 91]. This circumstance is illustrated in Figure 2.11. By switching the order of two rotations of magnitude  $\pi/2$  around the  $x$ - and  $y$ -axis, respectively, the result is completely changed. Hence a unique description of spatial rotations and a possibility for updating them between load and iteration steps is required.

Figure 2.12 displays the spatial rotation of a point  $A_0$  to the new position  $A$ . This rotation can be defined by a rotation axis  $\mathbf{n}$  and a rotation angle  $\varphi$ . Thus the position vector  $\mathbf{X}_{A_0}$  is rotated to give the vector  $\mathbf{x}_A$ . This rotation can be expressed as

$$\mathbf{x}_A = \mathbf{R} \mathbf{X}_{A_0}, \quad (2.60)$$

where  $\mathbf{R}$  is called *rotation tensor* and can be expressed through  $\mathbf{n}$  and  $\varphi$ , see *e.g.* Eberly [55].

Since  $\mathbf{n}$  is of unit length *a priori*, it only has two independent parameters. Together with the rotation angle  $\varphi$ , a spatial rotation can uniquely be defined by three independent parameters, where commonly  $\mathbf{n}$  is scaled to a length  $\varphi$  in order to include the entire rotation within one vector.

A consistent update of the rotation tensor  $\mathbf{R}$  is obtained through a multiplicative update, *i.e.* in step  $(i + 1)$  the rotation tensor can be expressed as

$$\mathbf{R}^{(i+1)} = \Delta\mathbf{R}^{(i)} \mathbf{R}^{(i)}, \quad (2.61)$$

where  $\Delta\mathbf{R}^{(i)}$  is the incremental rotation from step  $(i)$ .

Besides the described axis-angle representation, different approaches have been developed in order to enable a consistent description for the update of rotations, see Crisfield [48] and Krenk [82], where especially the possibility of an additive update (through modified rotation parameters) is of interest for the integration into an existing FEA-environment. Eberly [55] gives a very compact overview of different parameterizations for finite rotations, including transformation rules and estimations of computational cost.

Another approach, as used in the beam formulation by Lumpe et al. [91], consists in expressing the rotation through director displacements: Two directors<sup>4</sup> are introduced and their tip-displacements uniquely define the rotation state of the beam. It can be shown that also for this parameterization, only three independent parameters describe the entire rotation. Expressing rotations through displacements proves to be unique, path-independent and free of singularities, even for large rotations. However the modeling of junctions of several elements and the application of moments turns out to be considerably more complex, see [91].

Although in many ways the challenges encountered by the rotation description are the same for beams and shells, another aspect becomes important specifically for beam elements: Since the beam element description is reduced to its center-line, see Figure 2.1, already the unique and consistent definition of the local axes spanning the cross section is challenging, especially for spatially curved beams, as discussed *e.g.* by Bauer et al. [14].

### 2.4.2 Buckling of beam elements

Beam elements are encountered in various applications within lightweight structures: They provide the supports or act as columns, or they may act as integrated supporting arches. In all these applications beams act mainly in compression. Depending on the application, compression is often combined with bending. Since for the beam members slender dimensions are

---

<sup>4</sup> For shells, one director is sufficient, see *e.g.* Bischoff et al. [21] and Dornisch et al. [53].

## 2.4 Characteristics of geometrically non-linear beam elements

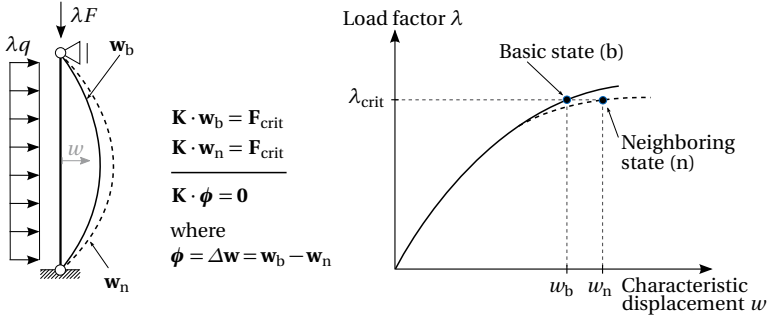


**Figure 2.13:** Plane buckling of a beam: Deformations  $\mathbf{w}_b$  and  $\mathbf{w}_n$  in the basic state resp. in the neighboring state, determination of the buckling mode  $\boldsymbol{\phi}$  and load-displacement diagram with the characteristic displacements  $w_b$  and  $w_n$

desired, they may be susceptible to buckling. Buckling occurs in absence of stability, which at its turn can be defined as "*the power to recover equilibrium*" as denoted by Felippa [59, p.28-3] or in other words: "*A structure is stable at an equilibrium position if it returns to that position upon being disturbed by an extraneous action*" [59, p.28-3].

Buckling of elements under compression is characterized by the existence of two infinitesimally close states of equilibrium for one load state  $\lambda$ . These states are referred to as *basic state* and *neighboring state*, respectively, see Figure 2.13. Hence the structure may change from one state to the other without an external force, as is the case for kinematic structures. The corresponding load state is referred to as critical load resp. buckling load  $\lambda_{\text{crit}}$ . The deformation between these two states – with an arbitrary scaling – is known as buckling mode  $\boldsymbol{\phi}$ .

Tracing buckling points<sup>5</sup> is an important part of structural analysis in the non-linear regime. Obviously, the problem described in Equation (2.62) will have several solutions for  $\lambda_{\text{crit}}$ . For most civil engineering structures, the first critical point, *i.e.* the one corresponding to the lowest load factor  $\lambda_{\text{crit}}$ , is of interest.

<sup>5</sup> For the sake of completeness the existence of other types of critical points like limit points shall be mentioned, however they are not in the focus of this thesis.

Buckling points may be detected through an analysis of the stiffness matrix. When the tangential stiffness matrix  $\mathbf{K}(\mathbf{u}, \lambda)$  turns out to be singular at a load level  $\lambda_{\text{crit}}$ , which is detected through

$$\det[\mathbf{K}(\mathbf{u}_{\text{crit}}, \lambda_{\text{crit}})] = 0 \quad \text{resp.} \quad \mathbf{K}(\mathbf{u}_{\text{crit}}, \lambda_{\text{crit}}) \boldsymbol{\phi} = \mathbf{0}, \quad (2.62)$$

a critical point is reached in which  $\boldsymbol{\phi} \neq \mathbf{0}$  is the *null eigenvector*. If a buckling point is reached, the eigenvector  $\boldsymbol{\phi}$  represents the buckling mode, corresponding to the arbitrarily scaled difference between the basis and the reference state introduced in Figure 2.13.

However, the detection of buckling points with the definition of the full non-linear problem in Equation (2.62) is computationally expensive when it comes to complex structures. For many applications like in early design stages of civil engineering structures, a simplified estimation of the critical load factors may be sufficient. In that case a *Linearized Prebuckling* (LPB) analysis may be applied, which drastically simplifies the eigenvalue determination from Equation (2.62). For the LPB the stiffness matrix is split into the elastic part  $\mathbf{K}_{\text{el}}$  and the geometric stiffness  $\mathbf{K}_{\text{geo}}$ . Furthermore the assumption that  $\mathbf{K}_{\text{geo}}$  is linearly dependent on the load factor  $\lambda$  is introduced, *i.e.*  $\mathbf{K}_{\text{geo}} = \lambda \cdot \mathbf{K}_{\text{geo}}^{\text{ref}}$ , where  $\mathbf{K}_{\text{geo}}^{\text{ref}} = \mathbf{K}_{\text{geo}}(\lambda = 1)$  is the geometric stiffness matrix evaluated at the reference state.

Consequently Equation (2.62) can be rewritten as

$$\mathbf{K}_{\text{LPB}} \boldsymbol{\phi} = (\mathbf{K}_{\text{el}} + \lambda \mathbf{K}_{\text{geo}}^{\text{ref}}) \boldsymbol{\phi} = \mathbf{0}, \quad (2.63)$$

which is often called the LPB stability eigenproblem. The solution of Equation (2.63) will deliver  $n_{\text{DOF}}$  eigenvalues  $\lambda$ , where  $n_{\text{DOF}}$  is the number of DOFs of the system. The eigenvalue  $\lambda_i$  closest to zero then is the critical load factor.

Through the assumed simplifications, which are cited *e.g.* by Felippa [59], the range of applicability of LPB is limited. The most important limitations in the present context are that prebuckling deformations must be small and that the effect of imperfection is considered negligible.

In the context of lightweight structures with bending-active members (beams) combined with tensile elements, see Chapter 4, a controlled buckling through pre-deformation of the beams is actively used in order to create new structural shapes. Within this combination, very slender beams

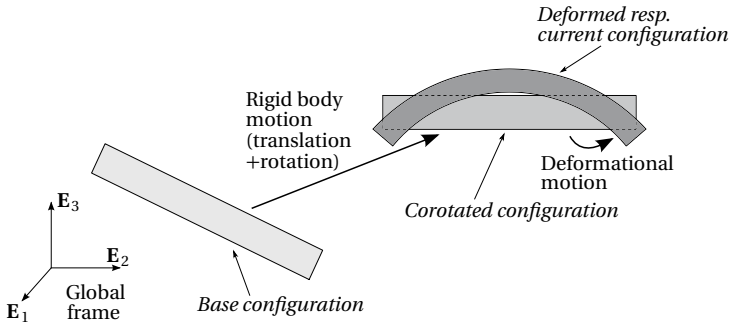


**Figure 2.14:** The corotational kinematic description as a decomposition of the element deformation (remade based on [59])

are applied, for buckling is prevented by the lateral stabilization from the membrane the beams are embedded in.

### 2.4.3 Applied beam element formulation

For the applications in the sequel of this thesis, notably in Chapter 4, an existing beam element formulation is used, a spatial corotational beam element formulation by Krenk [82]. Following the corotational concept, the deformation of the element is decomposed into two parts as illustrated in Figure 2.14: a rigid body motion of the element, accounting for the finite displacements and rotations, and an elastic element deformation. Since the applications in focus deal with large displacements but small strains, locally linear deformations are assumed. Although the elastic deformations are assumed to be small, at this point it should be noted that the rigid-body motion of the corotated frame still necessitates the description of finite rotations as explained in Section 2.4.1.

The element is based on six natural deformation modes that account for longitudinal extension, symmetric bending and opposing bending around the y- and z-axis, respectively, and for twisting around the x-axis. As nodal DOFs the element disposes of three displacements and three rotations per node, as illustrated in Figure 4.14, which largely simplifies the combination with other elements. The implementation used within this thesis has

## 2 Fundamentals

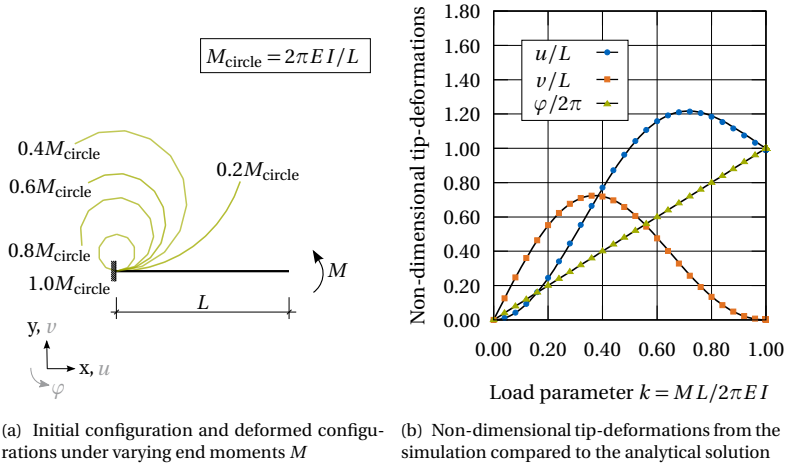


**Figure 2.15:** Roll-up of an initially straight cantilever to a circle in pure bending

been benchmarked by Heyden [69]. Selected benchmarks are shown in the following to demonstrate the abilities of the element. In these benchmarks, the reference solutions – analytical solutions resp. established solutions from literature – are indicated by continuous black graphs.

The so-called mainspring example illustrated in Figure 2.15 is a classical benchmark (see [11, 48, 82]) and demonstrates the ability to deal with large rotations in pure bending. From the analytical solution it can be seen that for a tip moment  $M = 2\pi EI/L$  the initially straight cantilever has to form a closed circle. Applying a sufficiently fine discretization and reasonable load increments, the beam closes to a circle up to numerical deviations.

The analysis of a  $45^\circ$  bending beam, loaded out of its plane, presents another well established benchmark, documented *e.g.* in Bathe et al. [11] and Bauer et al. [14]. The problem setup and the deformed configuration are shown in Figure 2.16. Although the computed out-of plane displacement  $w$  very nicely matches the reference solution from Bathe et al. [11], small deviations in the displacements  $u$  and  $v$  are still noticeable. These can be explained by the simplifying assumption of neglecting warping, although

## 2.4 Characteristics of geometrically non-linear beam elements

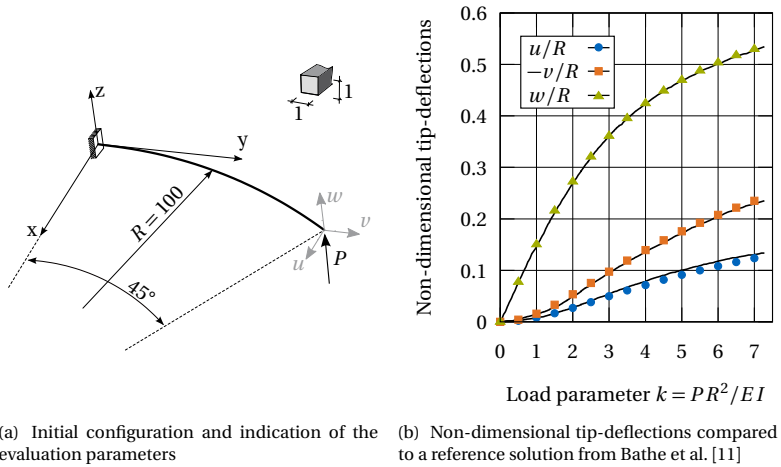


**Figure 2.16:** 45° bending beam loaded out of plane representing a spatial deformation including torsion

a non-warping free cross section (square) is analyzed here. However, the overall results prove the applicability of the element formulation to spatial problems with large deformations.

As a final example, the frame illustrated in Figure 2.17 is analyzed. This benchmark, discussed by Wriggers [149], is used to demonstrate the ability to couple elements and to analyze structures beyond the stability point, see Figure 2.17(b). In order to track the load-displacement curve beyond a critical value of  $w \approx -115$ , appropriate path-following methods like displacement- or arc-length-control (see [59, 82, 149]) are required. As can be seen, also the post-critical behavior is accurately tracked by the implemented element.

A series of other benchmarks for the applied element formulation can be found in [69]. In conclusion it can be stated that the element formulation fulfills all necessary requirements to be applied in the hybrid structures of Chapter 4.

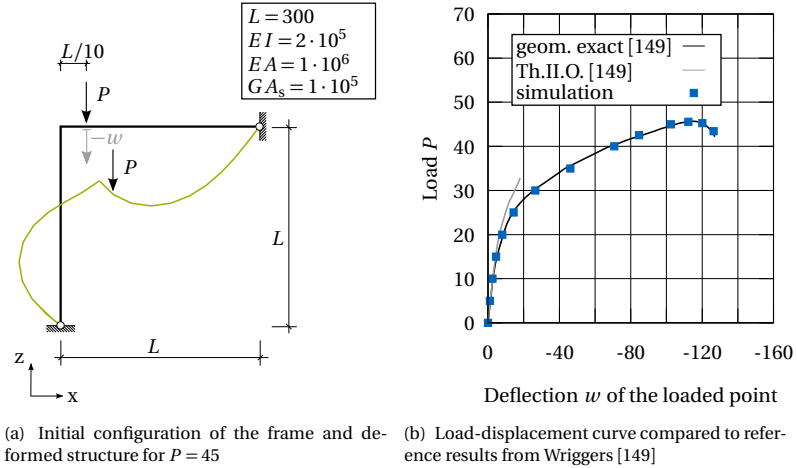


**Figure 2.17:** Bending of a one-sided frame under a single nodal force, leading to large deformations and a critical point

## 2.5 Characteristics of structural membranes

Structural membranes offer a unique language of shapes to designers as well as to visitors, mainly characterized by their curved silhouette that underlines the efficient lightweight nature of these structures.

The mechanical properties of structural membranes and their closely related shape entail very particular characteristics, also concerning their numerical design and analysis. Some of these specific characteristics are briefly introduced in the sequel as preparation for the developments in the next chapters.

### 2.5.1 Characteristics and consequences of the load-bearing behavior of structural membranes

One of the core characteristics of structural membranes is their load-bearing behavior: external and internal loads are transferred to the supports exclusively via tension, acting tangentially to their mid-surface. The absence of compression and bending allows for the very thin dimensions

of wide-span structural membranes, typically in the range of millimeters. In order to ensure stability and to transfer out-of-plane loads, prestress in the membrane and the cables is necessary.

Possibly occurring compressive forces lead to wrinkling in the membrane, as can be seen in Figure 3.15, which corresponds to local buckling in one direction due to the very thin to negligible bending stiffness. The analysis of wrinkling in structural membranes has been tackled by different approaches, see *e.g.* Jrusjrunkiat [77] and Rossi et al. [124].

In general wrinkling in membranes has to be avoided, as stated in [60, 136], since it results in loss of stiffness and eventually leads to fatigue in the material. Therefore, during the design and assessment of structural membranes, as discussed in Sections 2.5.2 and 5.3, the absence of compressive forces should be assured.

As mentioned above, the load-bearing through tensile forces allows for the use of very thin material. Two main types of material are in use, see Knippers et al. [81]:

- Foils, most prominent the widely used ETFE-foils, with a thickness of typically less than 0.3 mm.
- Woven coated fabrics, most prominent PTFE-coated glass fibers resp. PVC-coated polyester fibers, with a thickness typically in the range of 0.8 to 2 mm.

The investigation of the material behavior of foils and fabrics in use deals with topics like the consideration of orthotropy or the characterization of non-linear material properties, see *e.g.* Bridgens et al. [33, 34], Knippers et al. [81], Moritz [100], Münsch et al. [102], Schiemann [128], Uhlemann [143], and Widhammer [148]. Within this thesis the simplifying assumption of linear elastic isotropic material behavior is made, see also Section 2.3.2.

### 2.5.2 Principal design steps for structural membranes

In order to ensure the load-bearing exclusively via tension the design process for structural membranes can be seen as a design cycle. As commonly defined, this membrane design cycle consists of three major steps that mutually interact, see *e.g.* Bletzinger et al. [24], Dieringer [49], Gibson [61], Linhard [88], and Stimpfle et al. [134]:

- *Form-finding* has the task of defining the shape that fulfills both aesthetic and mechanical constraints. See Section 2.5.3 for more details.
- In *structural analysis and verification* the membrane structure is assessed against various loading scenarios in order to guarantee its safety, see also Chapter 5. The structural analysis commonly starts with the form-found shape and the desired prestress.
- The *cutting pattern generation* yields the plane patterns for the production of the individual membrane strips. Since compromises on the resulting shape and prestress have to be made, this step may lead to adjustments in the other steps of the design cycle.

In general, all design steps show large deformations which necessitate a geometrically non-linear analysis. The mechanical basis of the structural analysis considering geometrical non-linearity has already been laid out in Section 2.3. The form-finding will be introduced in more detail in the next section. For the sake of completeness, a short outlook on the cutting pattern determination shall be given here. Detailed discussions on cutting pattern determination may be found *e.g.* in Dieringer [49], Linhard [88], and Widhammer [148].

### **Outlook on cutting pattern determination**

Since structural membranes draw their load-bearing capacity out of the combination of prestress and their curved shape, they are characterized by a Gaussian curvature  $K \neq 0$ , see Equation (2.13), *i.e.* they are doubly curved. As a consequence, structural membranes in general are non-developable. The cutting pattern generation has the task of determining the plane, unstressed patterns that – after their assembly – result in the desired shape with the prescribed prestress resp. approximate it as good as possible.

As a first step in the cutting pattern determination the membrane surface is divided into separate strips. The boundaries of these strips in most cases follow geodesic lines as shortest paths between two points on the surface, see Forster et al. [60]. The numerical determination of these geodesic lines on facet-type FE-meshes (see Section 2.1.2) represents a computational challenge on its own, see Dieringer [49] and Linhard [88].

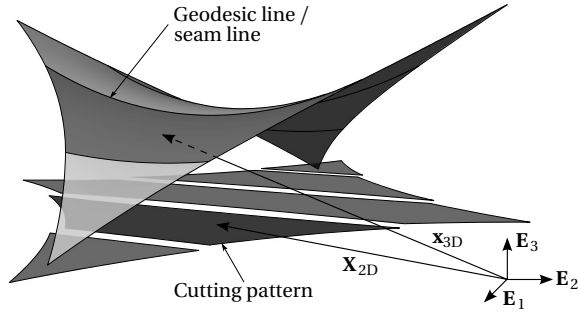


**Figure 2.18:** Schematic cutting pattern determination for a four-point sail: The separate strips are individually flattened and serve as starting configuration for a cutting pattern optimization.

The problem of cutting pattern determination for these strips can be formulated as an optimization problem, where the reference configuration  $\mathbf{X}_{2D}$  (see Figure 2.18) shall be such that the deviation of the stresses  $\boldsymbol{\sigma}_{el,2D \rightarrow 3D}$  from the mounting procedure and the prescribed prestress  $\boldsymbol{\sigma}_{pre}$  are minimized:

$$\min_{\mathbf{X}_{2D}} \rightarrow f(\mathbf{X}_{2D}) = \boldsymbol{\sigma}_{el,2D \rightarrow 3D} - \boldsymbol{\sigma}_{pre} \quad (2.64)$$

Several solution approaches to that problem have been proposed, e.g. a minimization of stress difference energy, see Bletzinger et al. [26] and Dieringer [49]. The *Variation of Reference Strategy* (VaReS) (see Dieringer et al. [51] and Widhammer [148]) as a more recent development is based on the minimum of the total elastic potential energy  $\Pi_{total}$ :

$$\min_{\mathbf{X}_{2D}} \rightarrow \Pi_{total} = \Pi_{el,2D \rightarrow 3D} - \Pi_{pre} \quad (2.65)$$

Thus VaReS avoids several of the numerical problems of the aforementioned approaches and allows incorporating anisotropy as well as highly non-linear material models as demonstrated in Widhammer [148].

### 2.5.3 Form-finding of tensile structures

The core part in the design process of architectural membranes is the form-finding, since it is the design step that ultimately reveals the shape of the structure. In the context of tensile structures it is the goal of any form-finding procedure to determine the shape of equilibrium w.r.t. a given stress distribution and boundary conditions.

Before the increasing success of numerical approaches to form-finding, physical form-finding had been used exclusively to determine the shape of textile membranes and cable net structures. Soap-film models with their isotropic prestress state can be used for the special case of minimal surfaces, *i.e.* surfaces that link given geometric boundary conditions with the minimum surface area possible. Therefore, soap-film or other physical models have successfully been used and still provide an attractive ground for creative form-finding within the design of membrane structures.

Minimal surfaces have also been in the focus of mathematical research (see *e.g.* Euler [57], Goldschmidt [63], Meusnier [98], Scherk [127], and Schwarz [131]) and still are today (see *e.g.* Costa [44]). The derived analytical solutions allow for pertinent comparisons of mechanical form-finding methods and the applied element formulations as used later in Section 3.4.2. Minimal surfaces provide several interesting characteristics, *e.g.* they are characterized by a mean curvature of zero, see Equation (2.15), which will be at the basis of the application in Section 3.5.3.

The search for a minimal surface area is obviously closely related to minimizing the material or weight used in a structure, which can be seen as a classical task for structural optimization, see Bletzinger et al. [25, 28], essentially providing the same results as the specialized form-finding methodology that is described in the following. From this procedure, the requirements for finite element formulations to be integrated in a form-finding analysis will be elaborated.

#### The inverse problem of form-finding

In a general sense, form-finding can be considered as a very special application of non-linear structural analysis. While in classical structural analysis the stress state is determined based on the load-dependent displacements, in form-finding problems this procedure is inverted: the desired stress state (*i.e.* the prestress of the membrane or cable net) is prescribed and

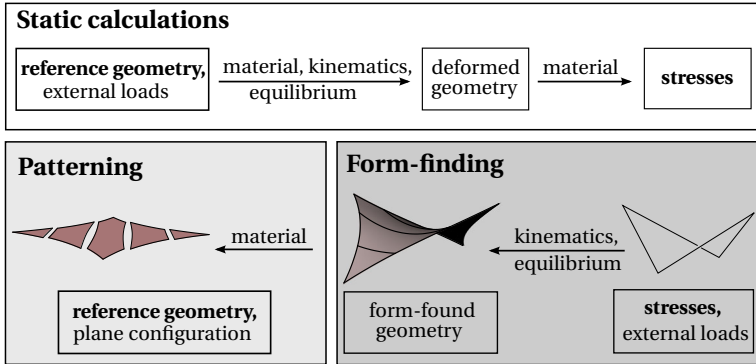


**Figure 2.19:** The inverse problem of form-finding, opposed to classical structural analysis (remade based on [24])

the geometry that brings this state into equilibrium is determined, see Figure 2.19. Due to this opposing behavior, form-finding is often described as an "inverse problem", see Bletzinger et al. [24, 26, 27].

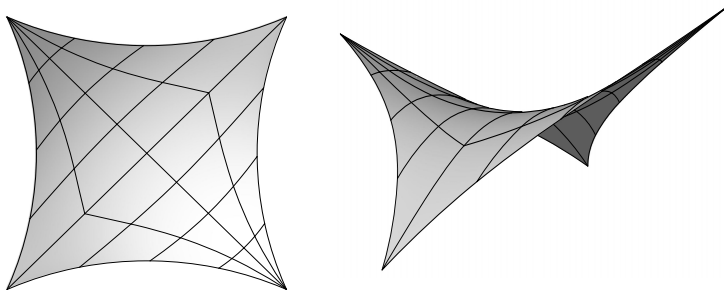
Since the goal of the form-finding procedure is to determine a shape of equilibrium, the form-finding problem can be formulated based on the principle of virtual work, see Equation (2.48). As the final shape of the structure is unknown at the beginning of the form-finding procedure, the problem has to be formulated in the current – yet still unknown – configuration. This way, equilibrium will ultimately be established for the form-found shape that fits the chosen prestress state.

For the case of mechanically prestressed structural membranes (in contrast to pneumatically prestressed cushions resp. air-halls), no external loads are considered during the form-finding. Comparing the self-weight of structural membranes – in the range of some few  $\text{kg}/\text{m}^2$ , see [81] – to the level of prestress, usually self-weight is neglected, too. Thus the balance of momentum, expressed through the internal virtual work in the current configuration can be simplified from Equation (2.49) to

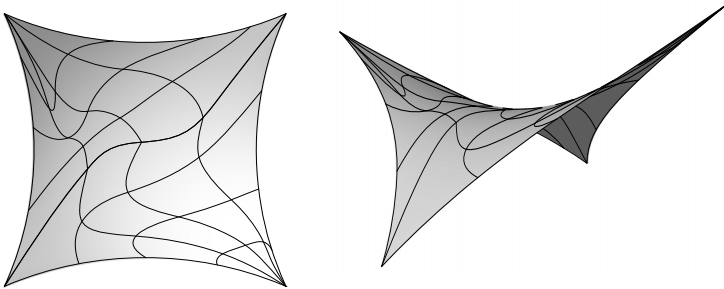
$$\delta W_{\text{cur}} = \delta W_{\text{cur,int}} = - \int_{\Omega} \boldsymbol{\sigma} : \delta \mathbf{e} d\Omega = 0, \quad (2.66)$$

where the Cauchy stresses now represent the prescribed prestress state.

## 2 Fundamentals



(a) Regular parameterization and corresponding deformed geometry



(b) Artificially distorted parameterization and corresponding deformed geometry

**Figure 2.20:** Illustration of the "non-unique" surface parameterization: Two different parameterizations describing the same geometry.

As described in Section 2.3, the problem from Equation (2.66) is discretized in order to be treated numerically. In the case of form-finding, the resulting stiffness matrix  $\mathbf{K}$  turns out to be singular. This deficiency corresponds to non-unique positions of the nodes on the determined shape, as illustrated in Figure 2.20. A physical counterpart to this phenomenon can be found in soap-bubbles where the soap is floating on the surface, although not altering the bubble's shape (see also Isenberg [75]).

Since this singular problem cannot be handled by the usual means of structural analysis, special approaches are required for the form-finding simulation. Many different methods have been proposed in order to overcome this problem, like the dynamic relaxation, see Barnes [8] and Wakefield [145], the force density method by Linkwitz [89] or adapted linearization techniques as presented by Haug [68]. As form-finding methodology in the present thesis, the *Updated Reference Strategy* (URS), initially proposed by Bletzinger et al. [27], is applied.

*A priori* all mentioned form-finding approaches are viable and should lead – at least for cases with a unique solution like minimal surfaces – to the same results. However, a round robin exercise on form-finding carried out by Gosling et al. [65] revealed considerable differences between the different methods respectively their implementations in various software packages.

### Form-finding with the updated reference strategy

In URS, the form-finding problem is set up as a combination of the original problem in the current configuration, according to Equation (2.66), and a stabilization term. In analogy to the expression in the current configuration, this stabilization term is defined by a modified problem in the reference configuration,

$$\delta W_{\text{ref}} = \delta W_{\text{ref,int}} = - \int_{\Omega_0} (\mathbf{S} : \delta \mathbf{E}) d\Omega_0 = 0, \quad (2.67)$$

see Equation (2.49), where now also the PK2 stresses are prescribed.

By linearly blending the two respective formulations for equilibrium of the structure,  $\delta W_{\text{cur}}$  from Equation (2.66) and  $\delta W_{\text{ref}}$  from Equation (2.67), while introducing a *homotopy factor*  $\lambda$ , a mixed formulation is obtained:

$$\delta W_{\text{URS}} = \lambda \cdot \delta W_{\text{cur}} + (1 - \lambda) \cdot \delta W_{\text{ref}} \quad (2.68)$$

Thus, by adding a certain portion of the stable, related problem  $\delta W_{\text{ref}}$  formulated in the reference configuration, the originally singular problem  $\delta W_{\text{cur}}$  is stabilized. After each form-finding step, the resulting geometry is set as the new reference and the solution of the problem is repeated, thus

giving the name of the method. Obviously the homotopy factor  $\lambda$  controls the solvability of the problem: As long as  $\lambda$  is sufficiently small in order to stabilize the problem, the system of equations is guaranteed to converge. For a detailed discussion on the choice of  $\lambda$  and the resulting convergence properties the reader is referred to Bletzinger et al. [26] and Wüchner et al. [150].

As convergence criterion for the URS, a comparison of the different stress measures can be used: When convergence is achieved, the prescribed prestress  $S_0^{\alpha\beta}$  in the reference configuration matches the resulting stress  $\sigma^{\alpha\beta}$  in the current configuration. As shown in Equation (2.44) the two stress measures are linked by the pull-back operation  $S^{\alpha\beta} = \det[\mathbf{F}] \sigma^{\alpha\beta}$  with the deformation gradient  $\mathbf{F} = \partial \mathbf{x} / \partial \mathbf{X}$ , see Equation (2.32). Hence the convergence criterion of  $S^{\alpha\beta} \approx \sigma^{\alpha\beta}$  is equivalent to  $\det[\mathbf{F}] \approx 1$ , which means that both geometries, the current geometry  $\mathbf{x}$  and the reference configuration  $\mathbf{X}$ , are identical and a shape that fulfills equilibrium w.r.t. the given prestress and boundary conditions is found.

### Discrete formulation of the Updated Reference Strategy

In prestressed tensile structures, stress results from elastic deformation and from prestress,

$$\mathbf{S} = \mathbf{S}_0 + \mathbf{S}_{\text{el}} = S^{\alpha\beta} \mathbf{G}_\alpha \otimes \mathbf{G}_\beta, \quad (2.69)$$

with the prestress being indicated by the subscript "0".

Since in pure form-finding problems only prescribed and thus constant prestress is applied and no elastic stresses occur, the corresponding derivative of  $\mathbf{S} = \mathbf{S}_0$  in Equation (2.57) vanishes and the residual and stiffness expression for form-finding can be written in simplified form as

$$R_r^{\text{fofi}} = \int_{\Omega_0} (\mathbf{S}_0 : \mathbf{E}_{,r}) d\Omega_0 \quad \text{and} \quad K_{rs}^{\text{fofi}} = \int_{\Omega_0} (\mathbf{S}_0 : \mathbf{E}_{,r,s}) d\Omega_0, \quad (2.70)$$

where now only the first and second derivative of the strains are required.

### Enhancements of the Updated Reference Strategy

Based on the presented approach, various enhancements of the URS have been developed over time. For example important progress has been made

in the field of automatic stress adaptation and control of the prestress ratio as a shaping parameter, see Bletzinger et al. [26] and Wüchner et al. [150]. Lately the problem of integrating elastic members into the design process of structural membranes has gained more attention. These so-called *hybrid structures* unite both processes sketched in Figure 2.19 in one single process, introducing new design possibilities and structural capacities as well as new computational challenges, see Dieringer et al. [50], Lienhard [85], and Philipp et al. [113, 117]. The arising possibilities and mechanical implications will be discussed in more detail in Chapter 4.

Based on the observation that the singularity in the equilibrium in Equation (2.66) is only related to the in-plane movement of the nodes (see also Figure 2.20), a splitting of the residual force components is performed in the *eXtended Updated Reference Strategy* (X-URS) by Dieringer et al. [52].

### **Summary and conclusions of Chapter 2**

This chapter provides the necessary fundamentals for the developments in the following chapters. Most of the explanations are made for surface structures, however the main conclusions and developments are valid for line elements (beams, cables) as well.

Within this chapter, notably the following aspects have been presented:

- differential geometry (notably of surfaces)
- geometry description and parameterization
- NURBS-based B-Rep models as geometry description and using NURBS as basis functions in FEA
- fundamentals of structural mechanics and solution of structural problems with FEA
- specific aspects of structural mechanics and geometric parameterization for beam elements accounting for finite displacements
- specific aspects for the form-finding and analysis of structural membranes

Moreover several conventions and notations are introduced in order to simplify the developments and derivations in the following chapters.

## THE INTEGRATION OF GEOMETRY AND STRUCTURAL BEHAVIOR WITH ISOGEOMETRIC B-REP ANALYSIS

The load-bearing behavior of lightweight structures is closely linked to their shape: Making use of double curvature, shells resp. prestressed membranes are able to form structures of an impressive slenderness.

To allow for that slenderness, the shapes of lightweight structures often result from a close integration of a functional and aesthetic design on the one hand and mechanical form-finding resp. optimization on the other hand. In that regard Stimpfle [133] describes the usage of different models for the respective purposes and the conversion between these as one of the bottle-necks in the design process of lightweight structures. In order to enable the required close collaboration between design and engineering, the *isogeometric B-Rep analysis* (IBRA) delivers the potential for a deep CAD-CAE-integration on one model.

Within this chapter, IBRA as a technique for the design and analysis of lightweight structures is presented. For the analysis of structural membranes, several components are developed. Finally, selected examples demonstrate the potential and allow to critically assess the application of IBRA for the design and analysis of membrane structures.

**Remark I:** The geometric modeling of the presented examples has been performed within the CAD software *Rhino3D* [95]. All structural analyses have been realized with the FE-code *Carat++* [29] which is integrated to *Rhino3D* by the in-house plug-in *TeDA* [23].

**Remark II:** In parts the content of this chapter has been published in Philipp et al. [114–116, 118]. For the sake of easier readability these sources will not always be cited explicitly.

## 3.1 Lightweight structures and the interaction of geometry and structural behavior

More than most other structures, lightweight structures rely on an “optimal” shape. Consequently they are (to be) designed in such a way that they transfer loads using their geometry, *i.e.* mainly (shells) resp. exclusively (tensile structures) by normal stresses and by reducing bending as much as possible. This ensures the optimal use of the cross-section through constant stresses along the thickness (see also Figure 4.1), thus allowing for a reduction of the used material.

Two examples illustrate the close interaction of geometry and structural behavior for lightweight structures:

- Shell structures are very sensitive to their geometry-adapted support conditions as well as their loading conditions.
- Structural membranes depend on their geometry – mainly their curvature – to withstand loads, but also to prevent “events” like ponding.

In consequence the shape-definition of lightweight structures usually is an iterative process, with alternating geometrical modifications and mechanical analyses. This iterative process can be illustrated in the form-finding of a structural membrane (see Section 2.5.3): Here the geometrical modeling of the initial shape (characterized *e.g.* by high- and low-points) enters

the mechanical form-finding analysis. The form-found shape at its turn (possibly after several iterations) is further used in the architectural design. To facilitate a close collaboration between the geometrical design and a structural analysis, an approach that allows both disciplines to collaborate on one model is required. In the following a technique that meets those requirements is presented.

### **3.2 The isogeometric B-Rep analysis for lightweight structures**

For several decades the finite element method (FEM) as the predominant method for computer-aided engineering (CAE) on the one hand and the computer-aided design (CAD) on the other hand have evolved more or less independently. When the need for a better CAD-CAE-integration (also referred to as "design-through-analysis work-flow") had been addressed, most approaches have aimed on facilitating the automatic creation of a separate, specialized analysis model from the CAD model.

Complex and powerful mesh-generation approaches have helped to automatize that task to some extent. Nevertheless considerable manpower still is invested in order to set up the structural model. Conversion between the models, especially recovering information from CAE to CAD, is time-consuming, error-prone and, generally, only approximative (see also Coll Sans [43], Hughes et al. [73], and Topping [142]).

In this context the *isogeometric analysis* (IGA) and – applied in the present work – the *isogeometric B-Rep analysis* (IBRA) have been developed in order to overcome the gap between CAD and CAE.

#### **The concept of the isogeometric B-Rep analysis**

The *isogeometric B-Rep analysis* (IBRA) which has been recently introduced by Breitenberger et al. [31] can be seen as a generalization of the *isogeometric analysis* (IGA) which at its turn had been introduced by Hughes et al. [73]. Within the present work only a very brief overview is given, for further details on IGA and IBRA in general, the reader is referred to Breitenberger et al. [31], Cottrell [45], and Hughes et al. [73].

As already discussed in Section 2.2, the isogeometric paradigm entails the use of basis functions from CAD (most commonly NURBS, see Equations (2.23) and (2.26) as well as Figures 2.7 and 2.8) for representing the geometry as well as the solution fields. This approach is opposed to classical finite element analysis (FEA) where typically low-order – often linear – interpolating functions describe the geometry in a facet-type manner, see Figure 2.5.

While IGA in its pure form is restricted to complete patches, IBRA refers to the full NURBS-based Boundary-Representation (B-Rep) model (see Section 2.2 and Figure 2.9) which is standard in many modern CAD systems. To this end, IBRA provides the framework for a consistent mechanical interpretation of the geometrical trimming operation. Thus, also trimmed and coupled patches can be used in a consistent manner: with IBRA, the complete CAD model can be augmented to an analysis suitable model.

Moreover the concept of IBRA allows enforcing various properties to the B-Rep entities. This can be seen as a new type of finite element formulation, the *B-Rep edge element*: Elements of this type permit enforcing among others coupling boundary conditions or supports and loads, as presented in Breitenberger et al. [31], or even mechanical properties like a cable element with prestress (see Philipp et al. [114]), which is introduced in Section 3.3.2.

The concept of embedding mechanical elements within the parameter space of a membrane or shell structure has recently been applied by Bauer et al. [13] to the non-linear isogeometric spatial Bernoulli beam introduced in [14] in order to form a B-Rep edge beam as stiffening resp. supporting element for lightweight structures.

### **3.3 Developments for the analysis of tensile structures with IBRA**

Since its conception, IGA has penetrated many areas of engineering and computational mechanics, such as structural and fluid mechanics, fluid-structure interaction, optimization, and contact mechanics. Various structural element formulations have been developed based on IGA, notably for shells [19, 20, 53, 56, 79] and membranes [114, 126], as well as cables and rods [7, 14, 66, 123].

For the analysis of tensile structures, new structural elements are required, notably a geometrically non-linear membrane element and an embedded cable element, both accounting for prestress. Their development is presented in the sequel.

### 3.3.1 Membrane element accounting for prestress

Owing to their very thin dimensions, structural membranes are commonly reduced to their mid-surface as illustrated in Figure 2.1. The thickness  $t$  of the membrane is assumed to be constant and deformation-independent. Hence it is convenient to apply Voigt-notation and to introduce entities that are pre-integrated over the thickness (see also Bischoff et al. [21]). Thus pre-integration of the stresses  $\mathbf{S}$  from Equation (2.38) over  $\theta^3$  yields the resultant forces

$$\mathbf{n} = \begin{bmatrix} n^{11} \\ n^{22} \\ n^{12} \end{bmatrix} = t \begin{bmatrix} S^{11} \\ S^{22} \\ S^{12} \end{bmatrix}. \quad (3.1)$$

Referring to a local Cartesian basis  $\mathbf{e}_\alpha$  in order to obtain values for the coefficients of the stress resultants that are free of the influence of a distorted basis, the PK2-stress resultants from elastic deformation can be written as

$$\bar{\mathbf{n}}_{\text{elast}} = \begin{bmatrix} \bar{n}_{\text{elast}}^{11} \\ \bar{n}_{\text{elast}}^{22} \\ \bar{n}_{\text{elast}}^{12} \end{bmatrix} = t \cdot \bar{\mathbf{D}}^{\text{isotropic}} \cdot \begin{bmatrix} \bar{\epsilon}_{11} \\ \bar{\epsilon}_{22} \\ 2\bar{\epsilon}_{12} \end{bmatrix} = t \cdot \bar{\mathbf{D}}^{\text{isotropic}} \cdot \bar{\boldsymbol{\epsilon}}. \quad (3.2)$$

In the present context  $\bar{\mathbf{D}}^{\text{isotropic}}$  is the material matrix for the St. Venant-Kirchhoff material model, see Section 2.3.2:

$$\bar{\mathbf{D}}^{\text{isotropic}} = \frac{E}{1-\nu^2} \cdot \begin{bmatrix} 1 & \nu & 0 \\ \nu & 1 & 0 \\ 0 & 0 & \frac{1-\nu}{2} \end{bmatrix} \quad (3.3)$$

In analogy to Equation (2.10) the transformation of the strain coefficients from a curvilinear system as in Equation (2.36) to a local Cartesian reference frame ( $\mathbf{e}_1, \mathbf{e}_2$ ) as required in Equation (3.2) is performed by

$$\bar{\epsilon}_{\gamma\delta} = \epsilon_{\alpha\beta}(\mathbf{e}_\gamma \cdot \mathbf{A}^\alpha)(\mathbf{A}^\beta \cdot \mathbf{e}_\delta). \quad (3.4)$$

The prestress  $\mathbf{S}_0$  from Equation (2.69) is pre-integrated in analogy to Equation (3.1) to give

$$\mathbf{n}_0 = \begin{bmatrix} n_0^{11} \\ n_0^{22} \\ n_0^{12} \end{bmatrix} = t \begin{bmatrix} S_0^{11} \\ S_0^{22} \\ S_0^{12} \end{bmatrix}, \quad (3.5)$$

respectively  $\bar{\mathbf{n}}_0$  in a local Cartesian frame.

With these derivations at hand, the contribution to the internal and external forces from Equation (2.56) as well as to the stiffness matrix from Equation (2.57) can be written as follows:

$$F_r^{\text{int}} = - \int_A (\bar{\mathbf{n}} : \bar{\epsilon}_{,r}) dA \quad (3.6)$$

$$F_r^{\text{ext}} = t \cdot \int_A (\boldsymbol{\rho} \cdot \mathbf{u}_{,r}) dA + \int_A (\mathbf{q} \cdot \mathbf{u}_{,r}) dA + \int_{\Gamma_0} (\mathbf{p} \cdot \mathbf{u}_{,r}) d\Gamma_0 \quad (3.7)$$

$$K_{rs}^{\text{int}} = \int_A (\bar{\mathbf{n}}_{,s} : \bar{\epsilon}_{,r} + \bar{\mathbf{n}} : \bar{\epsilon}_{,r,s}) dA \quad (3.8)$$

Here  $\boldsymbol{\rho}$  is the vector of body forces,  $\mathbf{q}$  are distributed external loads and  $\mathbf{p}$  are external loads on the edges. Note that  $\mathbf{q}$  and  $\mathbf{p}$  are supposed to be deformation-independent in the present developments.  $A$  is the surface area of the membrane and  $\Gamma_0$  are the respective edges.

From Equations (3.6) to (3.8) it can be seen that the stress resultants  $\bar{\mathbf{n}}$ , the variations  $\mathbf{u}_{,r}$  of the displacements and the first and second variations of the strains,  $\bar{\epsilon}_{,r}$  and  $\bar{\epsilon}_{,r,s}$ , respectively, are required for the determination of the stiffness and residual force contributions of the element.

The coefficients of the first variation of the in-plane strains  $\bar{\epsilon}$  in a Cartesian basis can be derived from Equation (3.4) and (2.36) as

$$\bar{\epsilon}_{\alpha\beta,r} = \epsilon_{\alpha\beta,r}(\mathbf{e}_\gamma \cdot \mathbf{A}^\alpha)(\mathbf{A}^\beta \cdot \mathbf{e}_\delta) = \frac{1}{2} a_{\alpha\beta,r}(\mathbf{e}_\gamma \cdot \mathbf{A}^\alpha)(\mathbf{A}^\beta \cdot \mathbf{e}_\delta). \quad (3.9)$$

The derivative  $a_{\alpha\beta,r}$  of the metric herein is obtained as

$$a_{\alpha\beta,r} = (\mathbf{a}_\alpha \cdot \mathbf{a}_\beta)_{,r} = \mathbf{a}_{\alpha,r} \cdot \mathbf{a}_\beta + \mathbf{a}_\alpha \cdot \mathbf{a}_{\beta,r}. \quad (3.10)$$

Applying discretization (see Section 2.1.2) the variation of the base vector w.r.t. the displacement variables can finally be determined referring to Equation (2.22) as

$$\mathbf{a}_{\alpha,r} = \mathbf{x}_{,\alpha,r} = \sum_i N_{,\alpha}^i \hat{\mathbf{u}}_{i,r}. \quad (3.11)$$

The second variations of the strain coefficients are obtained as

$$\epsilon_{\alpha\beta,r,s} = \frac{1}{2} a_{\alpha\beta,r,s} = \frac{1}{2} (\mathbf{a}_{\alpha,r} \cdot \mathbf{a}_{\beta,s} + \mathbf{a}_{\alpha,s} \cdot \mathbf{a}_{\beta,r}), \quad (3.12)$$

since from Equation (3.11) it is obvious that  $\hat{\mathbf{u}}_i$  only appears linearly and thus the second derivative w.r.t. the discretization parameters of the base vectors  $\mathbf{a}_{\alpha,r,s} = 0$ . Together with Equations (3.9) and (3.11),  $\bar{\epsilon}_{\alpha\beta,r,s}$  can thus be determined from the shape function derivatives  $N_{,\alpha}^i$ .

The variation of the elastic part of the stress resultants  $\bar{\mathbf{n}}_{\text{elast}}$  can be determined from Equations (3.2) and (3.9) as

$$\bar{\mathbf{n}}_{\text{elast},r} = t \cdot \bar{\mathbf{D}}^{\text{isotropic}} \cdot \bar{\boldsymbol{\epsilon}}_{,r}. \quad (3.13)$$

Hence all components for the determination of the element stiffness matrix and the internal force vector are determined.

### 3.3.2 Embedded cable element accounting for prestress

In the context of textile architecture, cables play a crucial role. They introduce accentuated kinks in the form of valley or ridge cables as displayed in Figure 3.4 or act as *Neumann* boundary condition in the form of edge cables. A broad variety of cable elements has been developed, including also isogeometric formulations as in Raknes et al. [123].

Commonly cable elements are formulated based on an *explicit* description of the cable geometry. Besides stability issues due to the lack of bending stiffness (see Raknes et al. [123] for a detailed discussion) the development of cable element formulations is rather straightforward. Problems arise for the coupling with other elements, like the coupling with membrane elements as it is necessary in the present case of architectural membranes. Already in standard FEA the coupling of different elements generally requires an adapted discretization or meshing, such that the respective elements to be coupled share common nodes. For IGA this problem is even more complex: The parameterization is non-interpolating, *i.e.* the control points are not located on the geometry (see Section 2.2), and the basis functions are not confined within the directly neighboring knotspans. Therefore a one-to-one identification of the control points to be coupled is no longer directly possible, which represents an important challenge.

#### **The concept of B-Rep edge elements**

Within this thesis, the development follows a novel paradigm: The curve of the cable is no longer described explicitly, but *implicitly*, embedded in the parameter space of the NURBS patch. This general concept for the formulation of embedded elements can be used for imposing a variety of analysis properties. Some application examples are listed in the following:

- *Neumann* boundary conditions (forces, moments);
- *Dirichlet* boundary conditions (displacements, rotations);
- mechanically motivated entities like the prestressed cable element presented in the sequel or the embedded beam element developed by Bauer et al. [13];
- internal (coupling) boundary conditions for the coupling between patches in multi-patch applications.

As illustrated by Breitenberger et al. [31], within the present context, the coupling<sup>1</sup> is not realized by a strong coupling of degrees of freedom, *i.e.* by merging control point positions. Instead the coupling is formulated in the

---

<sup>1</sup> Here "coupling" is used in the general sense of correctly accounting for different structural members that are coupled.

weak form, see Equation (3.14), on the basis of the virtual work expression. For a more detailed discussion on the coupling between patches, see also Apostolatos et al. [6] and Breitenberger et al. [31, 32].

This new concept of B-Rep edges allows for straightforward modeling of line elements such as cables or beams, but also supports that are embedded in a NURBS patch without requiring a separate discretization in 3D. The same concept is also used for the realization of the above mentioned coupling between different patches.

The mechanical contributions of these B-Rep edge elements are accounted for in the weak form. Hence various effects like coupling or the B-Rep cable element may be added to the equilibrium expression from Equation (2.48), written as

$$\delta W = \delta W_{\text{int}} + \delta W_{\text{ext}} + \delta W_{\text{B-Rep}}^{\text{coupling}} + \delta W_{\text{B-Rep}}^{\text{cable}} + \dots = 0, \quad (3.14)$$

where for ease of notation all  $k$  different B-Rep contributions are assembled in the expression  $W_{\text{B-Rep}}^k$ .

In analogy to Equations (2.54) and (2.55), the components of the residual force vector and the tangential stiffness matrix accounting for the B-Rep contributions can be derived:

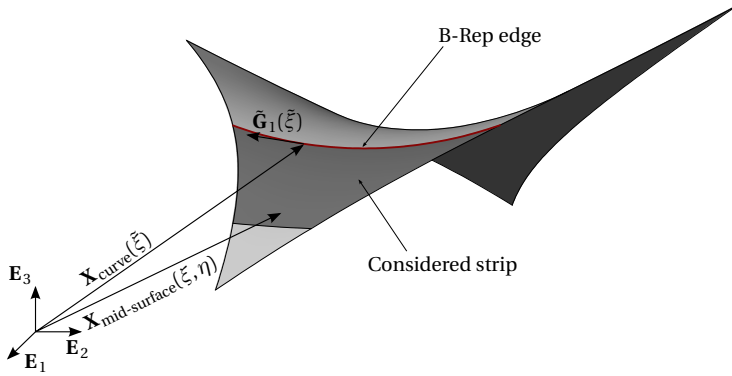
$$\begin{aligned} R_r &= -\frac{\partial W}{\partial u_r} = -\frac{\partial W_{\text{int}}}{\partial u_r} - \frac{\partial W_{\text{ext}}}{\partial u_r} - \sum_k \frac{\partial W_{\text{B-Rep}}^k}{\partial u_r} \\ &= R_r^{\text{int}} + R_r^{\text{ext}} + \sum_k R_{\text{B-Rep } r}^k \end{aligned} \quad (3.15)$$

$$\begin{aligned} K_{rs} &= -\frac{\partial^2 W}{\partial u_r \partial u_s} = -\frac{\partial^2 W_{\text{int}}}{\partial u_r \partial u_s} - \frac{\partial^2 W_{\text{ext}}}{\partial u_r \partial u_s} - \sum_k \frac{\partial^2 W_{\text{B-Rep}}^k}{\partial u_r \partial u_s} \\ &= K_{rs}^{\text{int}} + K_{rs}^{\text{ext}} + \sum_k K_{\text{B-Rep } rs}^k \end{aligned} \quad (3.16)$$

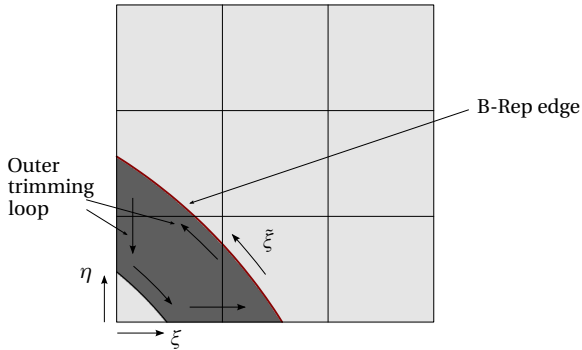
### Basis functions and integration of B-Rep edge elements

As mentioned above, the one-dimensional *B-Rep edge elements* dispose of an implicit geometry description. As such they are embedded into a surface as a non-zero knot span of a trimming curve. Hence the B-Rep

### 3 Integration of geometry and structural behavior with IBRA



(a) Geometry and local base vector  $\tilde{\mathbf{G}}_1$  of the cable, referring to the parameter  $\tilde{\xi}$  of the curve



(b) Parameter space and visualization of the outer trimming loop defining the considered strip

**Figure 3.1:** B-Rep edge element as an embedded cable along the trimming curve of a strip in a four-point sail

edge elements are situated along the boundary of the thus trimmed surface (for a description of the trimming, see Sections 2.2.2 and 2.2.3) with the curve parameter  $\tilde{\xi}$ , see Figure 3.1. Through this implicit definition in the parameter space of the surface, the B-Rep edge elements are embedded into NURBS surfaces and extract their basis functions from these surfaces as illustrated in Figure 3.2.

The thus extracted basis functions  $N_p^i(\tilde{\xi})$  as a subset of the basis functions  $R_{pq}^{ij}(\xi, \eta)$  of the NURBS surface still provide required properties w.r.t. their usage as basis functions for element formulations like partition of unity or linear independence.

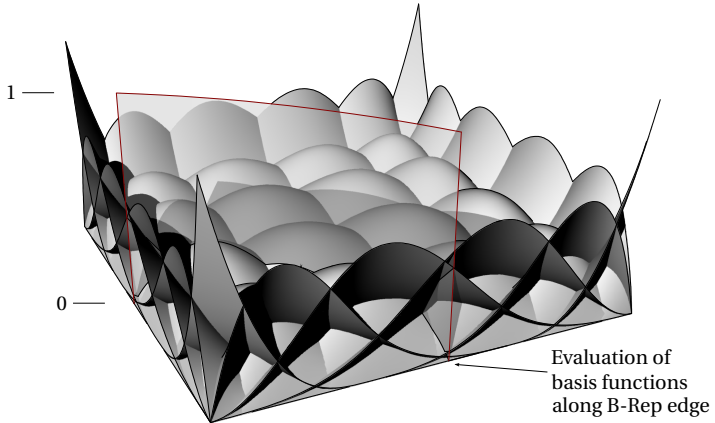
As presented in Section 2.2.1, the basis functions  $R_{pq}^{ij}(\xi, \eta)$  are related to the control points of the surface. Consequently each of the extracted basis functions  $N_p^i(\tilde{\xi})$  also refers to a control point of the surface and no additional control points (and with them additional degrees of freedom) are introduced. The extension of the (highlighted) affected control points  $\mathbf{P}_i$  (*i.e.* the corresponding basis function  $N_p^i(\tilde{\xi}) \neq 0$  along  $\tilde{\mathbf{C}}(\tilde{\xi})$ ) transverse to the curve of the cable reflects the overlapping basis functions, see Figure 3.3.

The numerical integration of these extracted basis functions is realized through Gauss-points along the curve. At each Gauss-point the extracted non-zero basis functions are evaluated and the respective contribution is assigned to the corresponding control point of the NURBS surface. Thus the contribution of the cable element to the residual force and stiffness, see Equations (3.15) and (3.16), is taken into account.

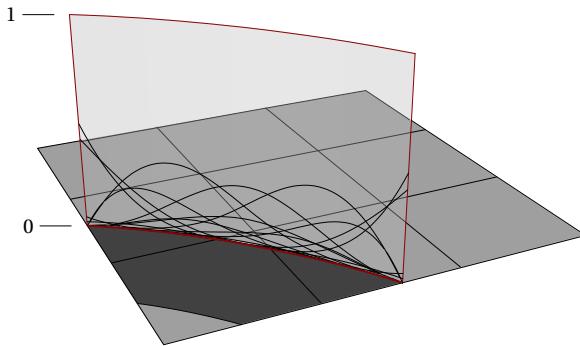
It is important to point out that – since it is a trimming curve (see Section 2.2.2) – there is no explicit description of the B-Rep edge curve in the geometry space. Consequently it can only be addressed through the parameter space of the surface. Once defined by the trimming operation, it is linked to the surface it is embedded in. As an example this implicit definition is illustrated by computing the length of an embedded cable in the next section.

In the sequel, an embedded cable element based on this new paradigm is formulated as a *B-Rep edge element*.

### 3 Integration of geometry and structural behavior with IBRA



(a) B-Spline basis functions  $N_{pq}^{ij}(\xi, \eta)$  of the NURBS surface (here with  $p = q = 3$  and  $3 \times 3$  elements) and location of the evaluation for the basis functions of the curve



(b) Extracted basis functions  $N_p^i(\xi)$  for the B-Rep cable element

**Figure 3.2:** Extraction of the implicitly defined basis functions for the B-Rep edge element from the embedding surface

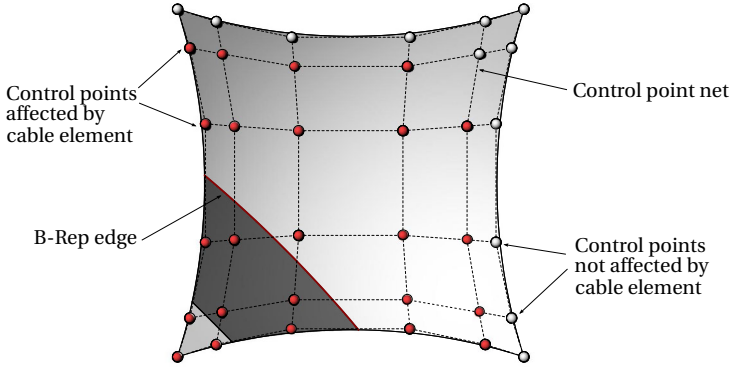


**Figure 3.3:** Top view of the four-point sail with embedded B-Rep cable element. The control points highlighted in red are affected by the considered B-Rep edge element.

### Geometry description of the cable as a B-Rep edge element

The length  $|L|$  of a *B-Rep edge element* in the reference configuration is given by

$$|L| = \int_{\Gamma_e} d\Gamma_e = \int_{\tilde{\xi}} \|\tilde{\mathbf{G}}_1\|_2 d\tilde{\xi} = \int_{\tilde{\xi}} \left\| \frac{\partial \mathbf{X}_{\text{curve}}}{\partial \tilde{\xi}} \right\|_2 d\tilde{\xi}, \quad (3.17)$$

where  $\tilde{\mathbf{G}}_1$  is the local base vector of the B-Rep element corresponding to the curvilinear coordinate  $\tilde{\xi}$  along the curve, derived from the position vector  $\mathbf{X}_{\text{curve}}$  of the spatial curve, see Figure 3.1(a). Through the implicit description of the geometry  $\mathbf{X}_{\text{curve}}$  of the curve, the expression is referred to the position vector of the surface along the B-Rep edge,

$$\mathbf{X}_{\text{curve}}(\tilde{\xi}) = \mathbf{X}_{\text{surf}}(\xi(\tilde{\xi}), \eta(\tilde{\xi})). \quad (3.18)$$

Applying Equation (3.18), the length  $|L|$  from Equation (3.17) can be expressed through the coordinates of the surface:

$$|L| = \int_{\tilde{\xi}} \left\| \frac{\partial \mathbf{X}_{\text{curve}}(\tilde{\xi})}{\partial \tilde{\xi}} \right\|_2 d\tilde{\xi} = \int_{\tilde{\xi}} \left\| \left( \frac{\partial \mathbf{X}_{\text{surf}}}{\partial \xi} \frac{\partial \xi}{\partial \tilde{\xi}} + \frac{\partial \mathbf{X}_{\text{surf}}}{\partial \eta} \frac{\partial \eta}{\partial \tilde{\xi}} \right) \right\|_2 d\tilde{\xi}$$

(3.19)

To perform this integration, the basis functions of the NURBS surface along the B-Rep edge are extracted as illustrated in Figure 3.2 and the above sketched integration procedure is applied.

The corresponding length  $|\ell|$  in the current configuration is defined analogously, now w.r.t. the surface description  $\mathbf{x}_{\text{surf}}$ .

### Kinematics, material law and equilibrium

According to classical cable mechanics the cable is characterized by its cross section area  $A^{\text{cable}}$  that is assumed constant along the cable, a homogeneous stress distribution through the cross section and the elastic stiffness that is material dependent. Here, as in Equation (3.3), a St. Venant-Kirchhoff material model is assumed as well as a constant and deformation-independent cross section area. Therefore, the stresses  $S^{\text{cable}}$  in the reference configuration are defined as

$$S^{\text{cable}} = S_0^{\text{cable}} + S_{\text{elast}}^{\text{cable}} = S_0^{\text{cable}} + E \cdot \epsilon_{11}^{\text{cable}}, \quad (3.20)$$

introducing the prestress  $S_0^{\text{cable}}$  in the cable, Young's modulus  $E$  and the longitudinal Green-Lagrange strain  $\epsilon_{11}^{\text{cable}}$ . In analogy to Equation (2.36) the strain in the cable is expressed through the metrics as

$$\epsilon_{11}^{\text{cable}} = \frac{1}{2}(\tilde{g}_{11} - \tilde{G}_{11}), \quad (3.21)$$

following the parameter  $\tilde{\xi}$  of the curve.

Referring to the implicit description of the cable geometry, the contribution of the cable element to the overall structural behavior can be expressed through its contribution to the internal virtual work by

$$\delta W_{\text{int}}^{\text{cable}} = \int_{\Omega_e} \mathbf{S}^{\text{cable}} : \delta \boldsymbol{\epsilon}^{\text{cable}} d\Omega_e = A^{\text{cable}} \int_{\Gamma_e} \mathbf{S}^{\text{cable}} : \delta \boldsymbol{\epsilon}^{\text{cable}} d\Gamma_e, \quad (3.22)$$

where  $\Omega_e$  and  $\Gamma_e$  represent the volume and the longitudinal extension of the B-Rep edge element, respectively. In Equation (3.22) the aforementioned assumption of a homogeneous stress distribution is used to perform the preintegration through the cross-section area  $A^{\text{cable}}$  in order to obtain the

force in the cable. The virtual work contribution  $\delta W_{\text{int}}^{\text{cable}}$  of the cable then enters the B-Rep contributions in Equation (3.14) as  $\delta W_{\text{B-Rep}}^{\text{cable}}$  from where it contributes to the internal force and stiffness of the embedding surface, see Equations (3.15) and (3.16), respectively.

#### **Application scenarios of the B-Rep edge cable**

As already discussed, the presented cable element is formulated as a B-Rep edge element along a trimming curve, *i.e.* along the boundary of a considered patch. Since several B-Rep contributions can be applied to one B-Rep edge simultaneously, see Equation (3.16), situations like ridge or valley cables can be simulated with the present approach, as is illustrated in the demonstrator application in Figure 3.4 for the different scenarios: Two surfaces with a non-matching parameterization are trimmed along one trimming curve. Edge cables are applied along all edges. Along the trimmed edges of the two surfaces that geometrically coalesce a cable element is assigned to one of the B-Rep edges. Additionally a displacement-coupling condition is applied between the two trimming edges, such that the surfaces stay attached.

Hence, all scenarios for the application of cable elements in the context of architectural membranes can be treated with the developed element.

#### **3.3.3 Outlook on the cutting pattern generation with IBRA**

The analysis of structural membranes with IBRA presented in this thesis reveals attractive properties for a future cutting pattern generation. The principle of cutting pattern generation has already been presented in Section 2.5.2 and illustrated in Figure 2.18.

For a closed NURBS-based surface description the geometric evaluation of the geodesic lines are straightforward, see Maekawa [92] and Polthier et al. [121], unlike the determination on facet-type meshes as they are used in classical FEA, discussed by Bletzinger et al. [26] and Dieringer [49]. The subsequent separation of the surface into separate strips can be performed by using these geodesics as B-Rep trimming curves, see Section 2.2.3. Note that those operations are even commonly fully supported by contemporary CAD systems.

### 3 Integration of geometry and structural behavior with IBRA

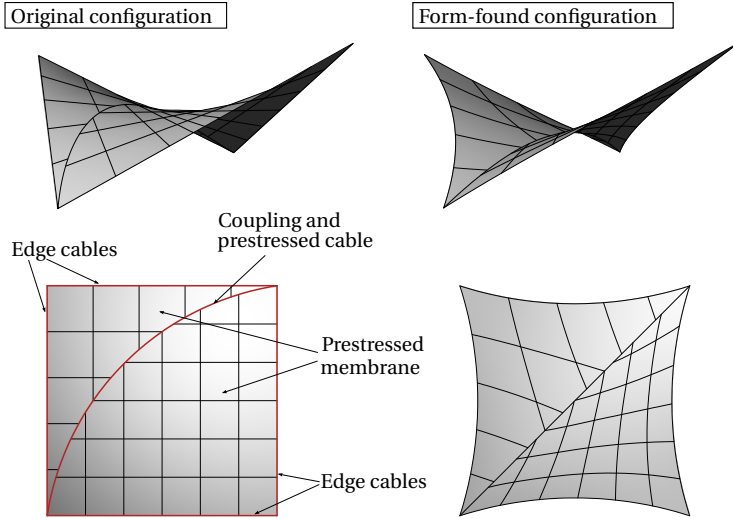


**Figure 3.4:** Application scenarios of the B-Rep cable element in the form-finding of a multi-patch structural membrane

For the development of a cutting pattern optimization of the individual strips within IBRA, two different concepts seem especially promising at the current state:

- In analogy to the approaches given by Bletzinger et al. [26], Dieringer [49], and Widhammer [148], the control point positions  $\mathbf{P}_{ij}$  of the (trimmed) patch in the plane reference configuration  $\mathbf{X}_{2D}$  are considered as unknowns. These are optimized in order to fulfill the requirements from Equations (2.64) resp. (2.65).
- Following the logic of the trimming operation, a novel approach might be considered, based on the present developments in IBRA: Instead of optimizing the control point positions  $\mathbf{P}_{ij}$  of the trimmed patch in the geometry space, the trimming curves  $\tilde{\mathbf{C}}$  themselves are moved across a plane NURBS patch. In this case the control points  $\tilde{\mathbf{P}}_i$  of the trimming curve in the parameter space  $(\xi, \eta)$  of the surface are the optimization variables. This approach corresponds directly

to the intuitive quest for the best cutting line on a piece of textile. As an objective for the optimization both the deviation in geometry and the (pre-)stress state between the mounted and the form-found shape could be used.

Based on the presented developments and on the work of Widhammer [148], promising developments towards a cutting pattern determination with IBRA have been made by Goldbach et al. [62].

## 3.4 Evaluation of the developed components

In the following, the developed elements and techniques shall be applied to selected numerical examples in order to evaluate their behavior and ability for the analysis of lightweight structures with IBRA.

### 3.4.1 Non-linear analysis of a stretched quarter-circle

The correct and accurate formulation and implementation of the developed elements in a non-linear structural analysis is demonstrated by using the example of a stretched quarter-circle, displayed in Figure 3.5(a).

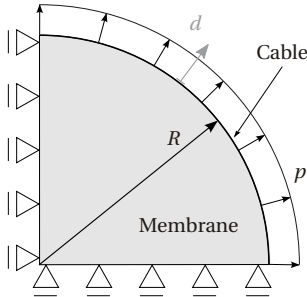
This example is modeled in three different ways, illustrated in the top row of Figure 3.6:

- (a) an untrimmed quarter of a circle, corresponding to a geometrically ideal parametrization of the structure,
- (b) a quarter of a circle, trimmed out of a rectangular patch, corresponding to the direct modeling approach of most CAD environments, and
- (c) a quarter of a circle composed of two oblique rectangular patches that are trimmed and coupled along arbitrary borders with non-matching parameterizations.

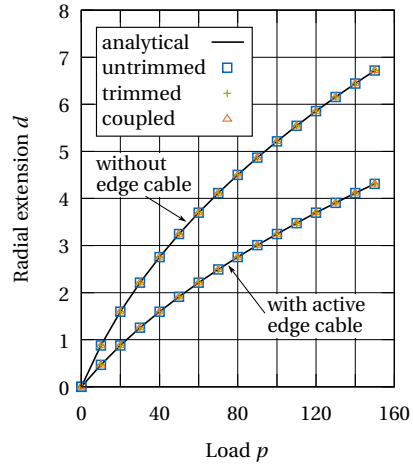
These models are analyzed as pure membrane examples (*i.e.* without cable, the upper graph in Figure 3.5(b)) as well as with an elastic cable applied at the edge (the lower graph in Figure 3.5(b)). In all cases the support conditions are the symmetry conditions of a complete circle and the distributed

### 3 Integration of geometry and structural behavior with IBRA

$R = 10$	$p = \text{variable}$
$E_{\text{cable}} = 1000$	$t = 1$
$E_{\text{mem}} = 100$	$A_{\text{cable}} = 1$
$\nu = 0$	



(a) Problem description and model parameters of the stretched quarter-circle



(b) Load-displacement diagrams for the different modelings depicted in Figure 3.6 with/without an edge cable

**Figure 3.5:** Quarter-circle under radial load constituted of a membrane and – if activated – an elastic B-Rep edge cable

load  $p$  is applied as a radial load, uniformly pulling the circle and resulting in a hydrostatic stress state in the structure, cf. Figure 3.5(a).

For this problem, the analytical solution for the radial extension  $d$  is

$$\frac{p}{E_{\text{mem}} \cdot t + \frac{E_{\text{cable}} \cdot A_{\text{cable}}}{R}} = \frac{1}{2} \frac{d^3}{R^3} + \frac{3}{2} \frac{d^2}{R^2} + \frac{d}{R}, \quad (3.23)$$

where  $p$  is the radial load,  $R$  is the initial radius,  $E_{\text{mem}}$  and  $t$  are the Young's modulus and the thickness of the membrane, and  $E_{\text{cable}}$  and  $A_{\text{cable}}$  are the Young's modulus and the cross section of the cable, respectively. For the case of the pure membrane example where the cable is not activated, the corresponding term vanishes. In Figure 3.5(b) the analytical solution for both with and without an edge cable is plotted in black.

At first, an ideal discretization, depicted in Figure 3.6(a), is analyzed. One can see from the graph in Figure 3.5(b) that the results from the non-linear analysis exactly match the analytical solutions with and without the edge cable, even for large deformations. Since in radial direction the

### 3.4 Evaluation of the developed components

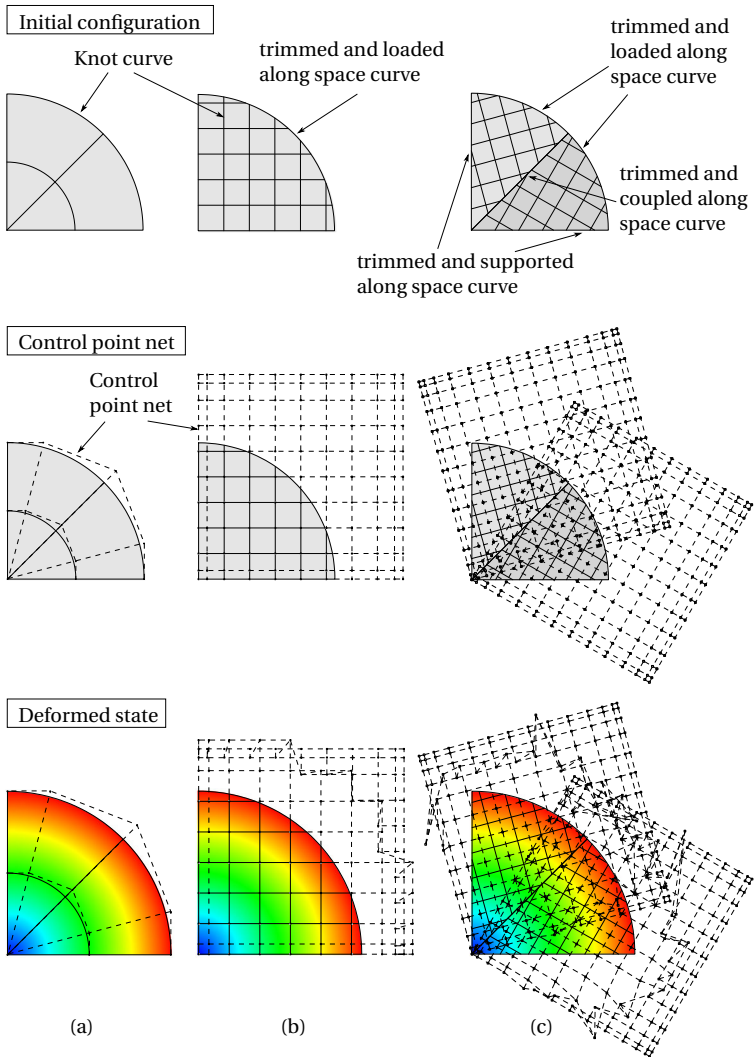


**Figure 3.6:** Different modelings of the stretched quarter-circle with control point net and deformed configurations (for quantitative results see Figure 3.5(b))

displacements increase linearly from center to edge and the exact circle can be represented by a polynomial degree of  $p = 2$  using NURBS, further degree elevation does not affect the result, see the deformed configuration in Figure 3.6(a).

Although this modeling is perfectly adapted to the problem, it does not reflect the direct modeling of the structure in a CAD environment, but rather represents an academic approach. Since the main goal in the application of IBRA is a close CAD-CAE workflow, modeling variations closer to CAD are further examined.

The most common approach in a CAD environment to model the quarter-circle is trimming the structure out of a rectangular patch, see Figure 3.6(b) and Figure 3.12. It is important to note that this trimming – at least in general – comes with a certain, user-defined or environment-dependent level of accuracy, see also Breitenberger et al. [31]. Therefore the quality of the results is limited by the quality of the original problem representation. In principle, the deviations in the results can be reduced to machine accuracy, supposing the corresponding precision in the geometry representation as will be discussed in Section 3.4.2. For the case with the elastic cable along the edge, this cable is now modeled along the trimming curve by enriching the trimming curve with the mechanical properties of the cable element as presented in Section 3.3.2. As can be seen in Figure 3.5(b), the results from the trimmed example without and with the edge cable again nicely match those from the ideal discretization.

The trimmed and coupled modeling and deformed configuration of the stretched quarter-circle are shown in Figure 3.6(c). Within this modeling, the major challenges are united in one example: the two patches are arbitrarily trimmed and coupled along two of the B-Rep edges. In addition, both types of boundary conditions mentioned in Section 3.3.2, Dirichlet boundary conditions at the supports and Neumann boundary conditions as the radial load  $p$ , are applied on the B-Rep trimming curves.

For this artificially complex geometry representation accurate results are obtained as well, see Figure 3.5(b). As mentioned in the previous section for the purely trimmed example, the quality of the result is just limited by the initial quality of the geometry representation.

With these examples of the stretched quarter circle, the membrane and the cable element have shown to provide accurate results for geometrically

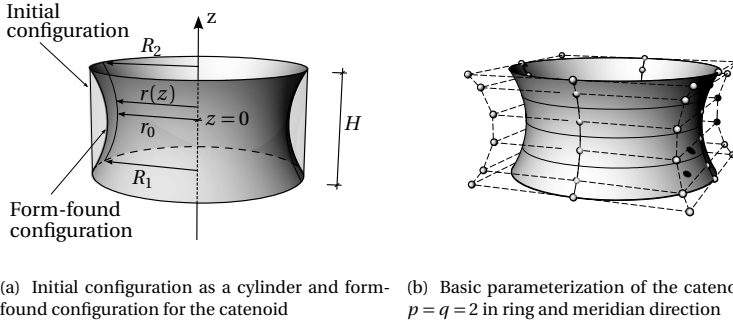


**Figure 3.7:** Problem description and parameterization of the investigated catenoid

non-linear analyses, see Figure 3.5(b). Furthermore the elements perfectly comply with the applied trimming and coupling approaches, as has been demonstrated with the examples in Figures 3.6(b) and 3.6(c). Therefore it can be stated that arbitrary geometries can be modeled and analyzed with the developed and presented methods.

### 3.4.2 Form-finding of a catenoid

In the following, the example of a catenoid will be form-found with the derived isogeometric membrane element for the demonstration of accuracy and robustness of the formulated elements in combination with different refinement strategies.

The catenoid has been the first minimal surface to be discovered, see Euler [57], Goldschmidt [63], and Meusnier [98]. Being a surface of revolution, the catenoid can be formed by rotating a catenary curve around an axis as shown in Figure 3.7. The boundaries of the catenoid are formed by two rigid rings which in the sequel are assumed to be of equal radius  $R_1 = R_2 = R$ . The form-finding then starts from a cylinder of radius  $R$  and height  $H$ .

#### Analytical description and form-finding

The resulting surface area  $A$  for a varying distance  $H$  between the rings of radius  $R = 1$  is plotted in Figure 3.8(a). While the curve is smooth up to a

height  $H_{\text{critical}}$ , the surface area suddenly drops and remains constant for any further increase of  $H$  beyond this limit.

For the range of  $H < H_{\text{critical}}$  the mathematical description of a catenoid provides the analytical solution for the surface area. The catenoid can be described by its radius  $r(z)$  which varies along the axis of rotation  $z$  according to the catenary equation

$$r(z) = C_1 \cosh\left(\frac{z + C_2}{C_1}\right), \quad (3.24)$$

where the coordinate  $z$  covers the height  $H$  of the catenoid, see Figure 3.7. The unknown constants  $C_1$  and  $C_2$  can be determined by introducing the radius of the upper and the lower bound, assumed to be equal in our case. In the present derivations  $z$  ranges from  $-H/2$  to  $H/2$ , leading to  $C_2 = 0$ .  $C_1$  then represents the minimal radius  $r_0 = r(z = 0)$ , which occurs for reasons of symmetry at  $z = 0$ . Note that even for these assumptions Equation (3.24) cannot be solved analytically for  $r_0$ . Instead Equation (3.24) simplifies to

$$R = r(z = \pm H/2) = r_0 \cosh\left(\frac{H}{2r_0}\right), \quad (3.25)$$

which then has to be solved for a given pair of geometry parameters  $R$  and  $H$ . For the parameters given in Figure 3.7, the unknown  $C_1$  can be determined to be  $C_1 = r_0 = 0.552434124$ .

The analytical solution of the surface area of the catenoid then is

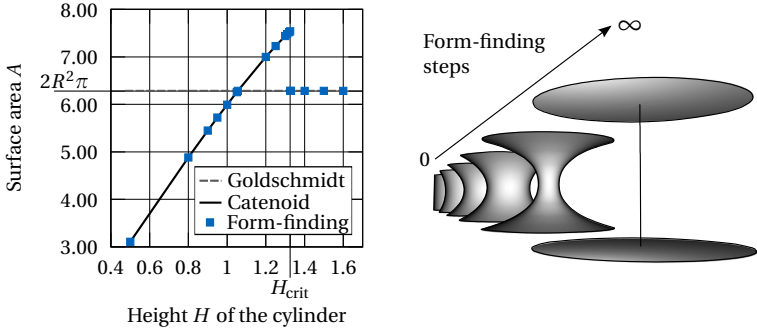
$$A_{\text{catenoid}} = r_0^2 \pi \sinh\left(\frac{H}{r_0}\right) + r_0 \pi H. \quad (3.26)$$

As can be seen in Figure 3.8(a), in the range of  $H < H_{\text{critical}}$  the computed surface areas from form-finding nicely match the analytical solution, thus underlining the accuracy of the applied approach and of the developed elements.

At the limit  $H_{\text{critical}}$  the catenoid collapses into two disconnected circular disks as displayed in Figure 3.8(b). These disks have a surface area of  $A_{2\text{disk}} = 2\pi R^2$ , which obviously stays constant independent of  $H$ . The result of two separated disks represents the so-called *Goldschmidt*-solution [63].

The critical height  $H_{\text{critical}}$  can also be confirmed by physical experiments, see *e.g.* Müller et al. [101], and mathematically be determined by an analysis

### 3.4 Evaluation of the developed components



(a) Evolution of the surface area with increasing height for the configuration from Figure 3.7(a) (b) Evolution of the collapse for an initial height  $H > H_{crit}$  throughout the form-finding steps

**Figure 3.8:** Form-finding of a catenoid: surface area as a function of the height  $H$  and evolution of the collapse for a height  $H > H_{crit}$

of the catenary equation, see *e.g.* Isenberg [75]. From Equation (3.25) one obtains

$$\frac{H}{R} = 2 \cdot \frac{r_0}{R} \cdot \operatorname{arccosh} \left( \frac{R}{r_0} \right) \quad (3.27)$$

which provides a maximum ratio of  $\frac{H}{R} \approx 1.32548684$ . The sharp reproduction of this limit in the form-finding simulation, see Figure 3.8(a), underlines the reliability and accuracy of the developed element and the form-finding approach.

Obviously the constriction of  $r_0$  towards zero, which can be observed in the collapsing process in Figure 3.8(b), is challenging for the elements, since they suffer severe distortion during this deformation. Ultimately the affected surface elements are degenerated to lines. For the formulated isogeometric membrane elements no convergence problems related to this constriction effect have been observed which demonstrates the great robustness of the developed membrane elements even for severe parametric distortions. The obtained values of the surface area before and after the critical limit nicely match the analytical solutions as can be seen in Figure 3.8(a).

A close inspection of the area evolution in Figure 3.8(a) shows an interesting phenomenon: For a range of approx.  $1.055 \leq H/R \leq 1.325$  the obtained surface area is bigger than the two-disk-solution. At a first glance this behavior seems to contradict the requirements for a minimal surface, since a solution with smaller surface area exists. Closer evaluation of these possible solutions provides the explanation that the catenoid only represents a *local minimum* in this range of the height  $H$ , whereas the *global minimum* is not reached in the form-finding analysis. Since the starting configuration has been a cylinder, the form-finding procedure is "caught" in this local minimum and cannot proceed to the global minimum, represented by the *Goldschmidt*-solution.

Form-finding in its nature is very closely related to a general optimization problem, see also Bletzinger et al. [25, 28]. The starting configuration has a significant influence on whether a global or a local optimum is found. In order to demonstrate this behavior, consider the modified starting configuration in Figure 3.9(a). Instead of a complete cylinder, an additional parameter is introduced by the radius  $R_{\text{inner}}$  of an inner cylinder that is linked to the outer rings by a circular disk with a corresponding hole. By controlling this radius  $R_{\text{inner}}$  we can control whether the *Goldschmidt*-solution or the catenoid solution is obtained as result of the form-finding analysis, for  $R_{\text{inner}}$  smaller resp. bigger than the limit determined in Figure 3.9(b). Thus the complete range of theoretically possible solutions can accurately be explored with the present approach and elements.

#### **Geometry approximation for the surface area of the catenoid**

Based on the discussion in Section 2.2.5 the approximation quality of the NURBS-based geometry description shall be investigated with the help of the form-finding of the catenoid. In order to demonstrate the convergence behavior of the geometry description, the surface area resulting from a form-finding analysis with different discretizations (see Section 2.2) shall be assessed against the analytically derived surface area  $A_{\text{catenoid}}$  from Equation (3.26), termed  $A_{\text{analytical}}$  in the following. As a starting configuration for the form-finding the cylinder from Figure 3.7 is used. In the ring direction, a polynomial degree  $p = 2$  is applied and the ring is divided in 16 elements. Since a circle can be described exactly by a NURBS of polynomial degree  $p = 2$ , no error is introduced by the discretization in the ring direction and further refinement is hence useless. In the merid-

### 3.4 Evaluation of the developed components

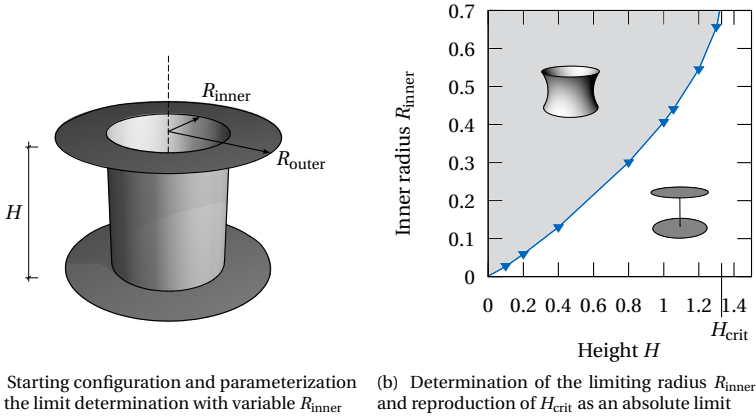


**Figure 3.9:** Controlling the obtained minimal surface – either the catenoid or the *Goldschmidt*-solution – by varying  $R_{\text{inner}}$

ian direction, the polynomial degree  $p$  is varied and a refinement  $r$ , *i.e.* a subdivision along the meridian, is introduced, see Figure 3.10(a). For all parameterizations, a sufficiently large number of form-finding steps with highest solution accuracy has been carried out, thus only leaving the geometry approximation as a source of deviation.

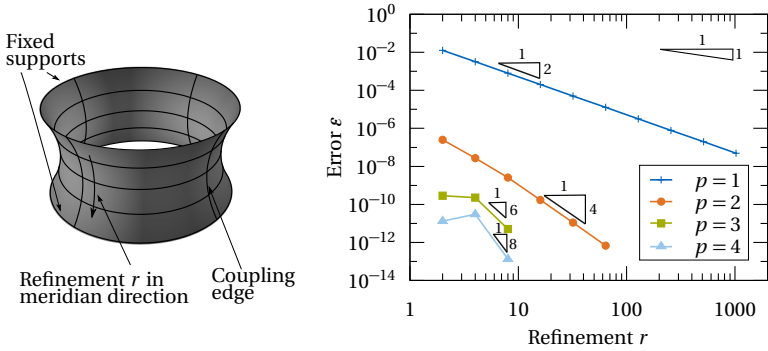
As a measurement for the deviation a relative error  $\varepsilon$  is introduced as

$$\varepsilon = \frac{|A_{\text{computed}} - A_{\text{analytical}}|}{A_{\text{analytical}}}. \quad (3.28)$$

In Figure 3.10(b) the relative error  $\varepsilon$  is plotted for polynomial degrees  $p$  from 1 to 4 with increasing refinement  $r$ . As expected, for all polynomial degrees the error decreases, ultimately to machine precision. It should be noted that a polynomial degree of  $p = q = 1$  would be identical to the solution of the form-finding problem using "classical" FEA with bi-linear elements.

The order of convergence to be expected for this evaluation of the surface area is  $2(p - m)$ , where  $p$  is the polynomial degree and  $m$  the order of derivatives occurring in the present evaluation, see Strang et al. [135] and Zienkiewicz et al. [152]. For the surface area evaluation in Equation (3.26)

### 3 Integration of geometry and structural behavior with IBRA



(a) Problem description (see also Figure 3.7(a)) and refinement parameters for the investigation (b) Evolution of the error  $\epsilon$  in the surface area for increasing refinement  $r$  and different polynomial degrees  $p$  in meridian direction

**Figure 3.10:** Approximation quality and convergence of the geometry representation of a catenoid

no derivatives occur, therefore  $m = 0$  and the slope of the error to be expected is  $2p$ . Within a certain range – between a too coarse parameterization on the one end and limits of numerical evaluation at around  $10^{-14}$  on the other end – this slope of  $2p$  can be observed in the log-log diagram in Figure 3.10(b). From this fit it can be concluded that the pure discretization error dominates the convergence behavior.

In general it can be stated that NURBS-based descriptions usually are very close to typical real membrane geometries and obviously most other shapes used in engineering, see *e.g.* the Olympic roofs in Section 3.5.2. Applying refinement strategies, the quality of the approximation can be improved quasi-arbitrarily.

### 3.5 Application examples for the shape definition and analysis of lightweight structures with IBRA

To demonstrate the abilities and potential of analyzing lightweight structures and defining their shape with the isogeometric B-Rep analysis, three examples are presented. In addition to the advantages of using IBRA, shortcomings and possibilities for future developments are discussed.

### 3.5.1 Generation of an inflated bubble cluster

Besides interesting characteristics in terms of speed and accuracy of the computation discussed in the previous sections, the most promising potential of IBRA lies in the power of integrating design and analysis within one single model. The example of the formation process of a bubble cluster reveals this potential.

As illustrated in the overview displayed in Figure 3.11 this cluster of three intersecting bubbles is defined through an interaction of geometrical and mechanical operations.

In step (1) a circular disk is modeled within the CAD-environment. The circular disk is trimmed out of a rectangular patch as depicted in Figure 3.12(left). This circular disk is given the mechanical properties of a thin elastic membrane, supported along its trimming edge. Applying an internal pressure as a follower load from below on the initially flat membrane, in step (2) it is inflated to a single bubble as displayed in Figure 3.12(right).

Once the bubble has reached the desired size resp. an acceptable stress level, the obtained geometry as the result of a mechanical operation – still an intact NURBS-based CAD geometry – is again manipulated in the CAD-environment: In step (3) the bubble is copied (two times) and the resulting bubbles are finally intersected. Figure 3.13 shows this intersection for two bubbles and the detail of the control point polygon of a trimmed bubble.

The trimming edges from the intersection are used to enforce the coupling between the bubbles in step (4). A displacement-coupling B-Rep edge element as mentioned in Section 3.3.2 is therefore modeled along the intersection lines, penalizing a relative displacement between the coupled bubbles. As illustrated in Figure 3.14 the applied penalty factor  $\alpha_{\text{disp}}$  for the displacement – corresponding to a spring stiffness of coupling springs [6, 31] – allows controlling the gap between the patches: Decreasing  $\alpha_{\text{disp}}$  leads to a larger gap between the patches. The coupling points are illustrated in orange in Figure 3.14.

Besides the coupling, a refinement of the bubble cluster is also performed in step (4) in order to be able to represent the displacements that might occur in subsequent loading scenarios, see Figure 3.11.

Finally in step (5) the bubble cluster is subjected to wind suction with varying intensity across the respective bubbles. Under this load the whole cluster is pulled in one direction (here towards the back and the right)

### 3 Integration of geometry and structural behavior with IBRA

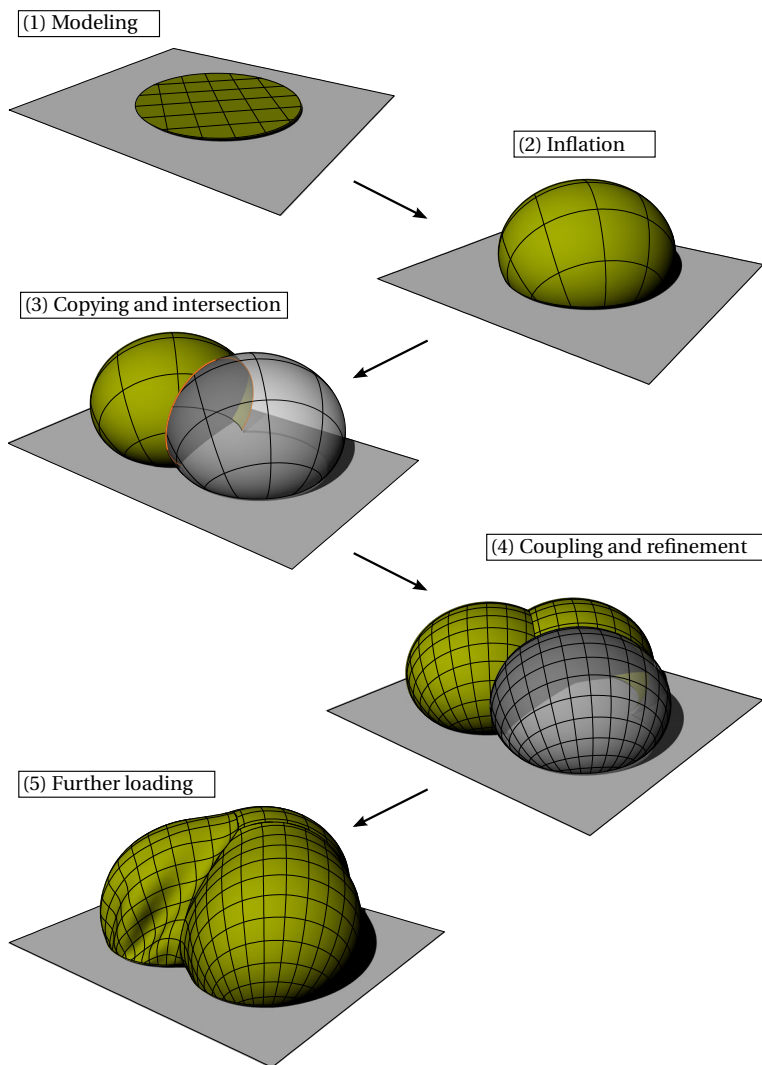


**Figure 3.11:** Generation of a bubble cluster as a combination of geometrical and mechanical operations

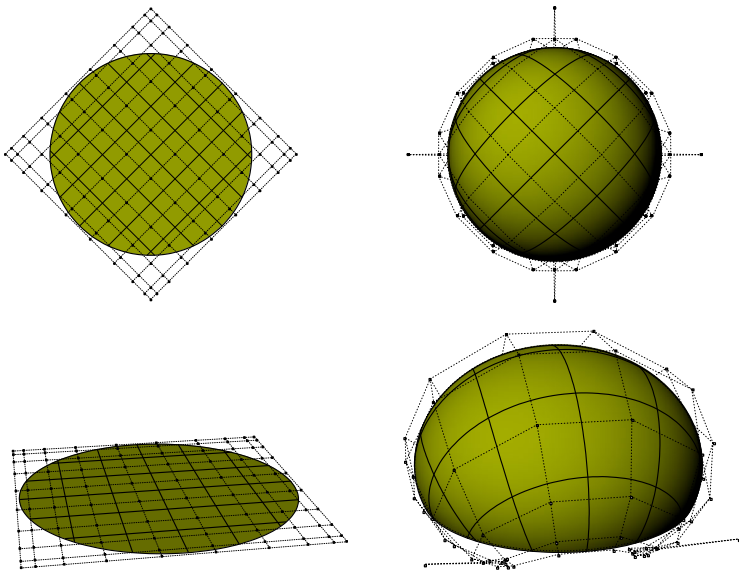


**Figure 3.12:** Detail of step (1) and (2) in top view and perspective with the control point net. With the exception of the four corner points of the initial circular disk are affected by the inflation and change their spatial position.

which eventually leads to the occurrence of wrinkles as can be seen in Figure 3.11. The pattern of these wrinkles follows the orientation of the principal stresses, thus forming a kind of "tension cord".

As displayed in detail in Figure 3.15 substantial refinement, *i.e.* an enriching in DOFs (see Section 2.2.1), is required in order to permit the representation of the deformation pattern that yields those wrinkles<sup>2</sup>.

The example of the bubble cluster illustrates the potential that lies in using one common model for design and analysis: Not only the conversion between different models is omitted – and with it an important source of

<sup>2</sup> However with membrane elements lacking bending rigidity an analysis of these wrinkles and their wavelength would require specialized wrinkling models, see Section 2.5.1, or the usage of a shell element formulation with correspondingly small thickness.

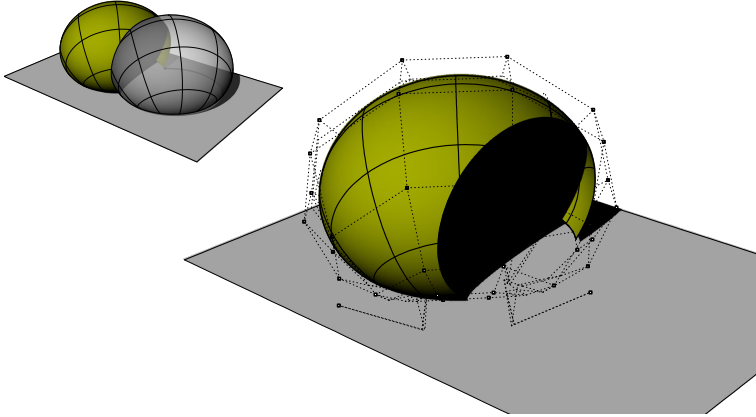


**Figure 3.13:** Intersection of the copied bubbles in step (3): The intersection is realized by trimming along the intersection line, as for the two bubbles on the left. The control point net of a trimmed bubble is depicted on the right.

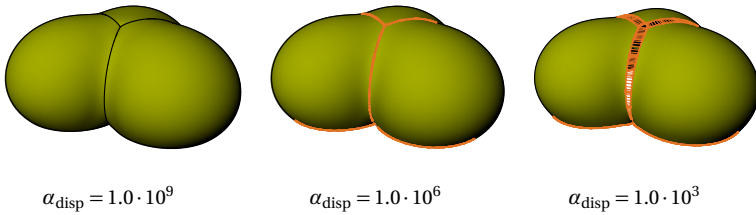


**Figure 3.14:** Controlling the "watertightness" with the help of the penalty factor  $\alpha_{\text{disp}}$  for the displacement coupling of the B-Rep coupling edges in step (4).

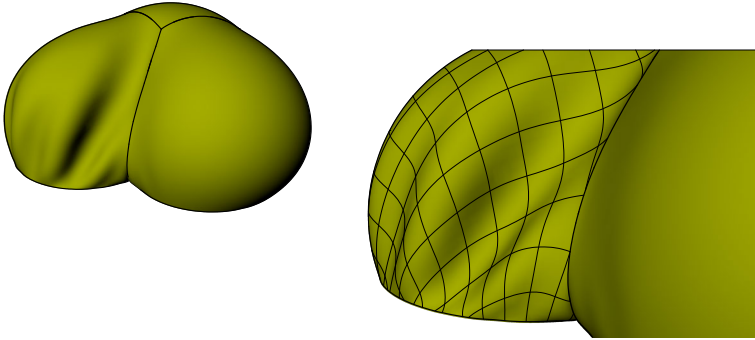


**Figure 3.15:** Wrinkles for the case of a varying wind suction load in step (5). The occurrence of wrinkles and their wavelength strongly depend on the applied refinement, displayed on the right.

error and inconsistencies – but also the advantages of both "worlds", the geometrical design and the mechanical analysis, come to use. Eventually, by alternately applying geometrical modifications and mechanical analyses, an easy and fast way of creating physically motivated structures is established.

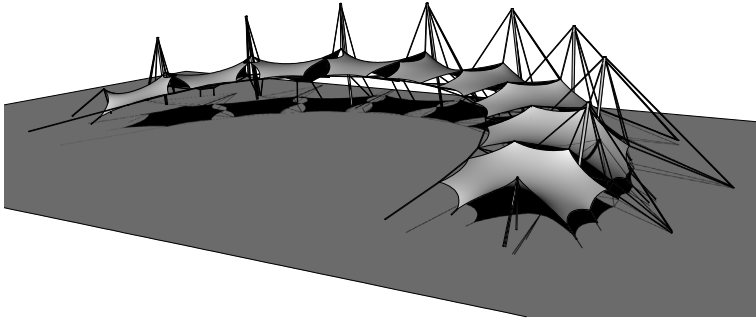
However, the common model still has to fulfill the requirements for the analysis. As illustrated with the example of the wrinkles, substantial refinement from the design model to the analysis model might be necessary in order to yield mechanically correct results. On the downside, a refined model with a significantly high number of DOFs might be far less attractive for design purposes, due to both issues of speed and ease of manipulation.

#### 3.5.2 Form-finding of the roof of the *Olympiastadion München*

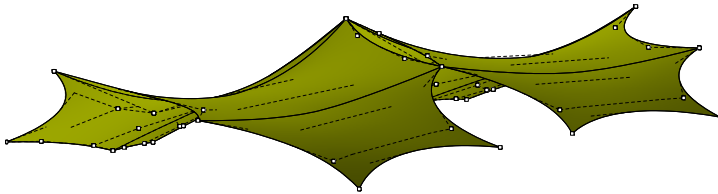
The *Olympiastadion München*<sup>3</sup> (Olympic Stadium Munich) was built as the main venue for the 1972 Summer Olympics. It is mainly known for its roof landscape which has become iconic for lightweight architecture.

Figure 3.16 depicts the result of a numerical form-finding (see Section 2.5.3) of the roof of the Olympic Stadium. Despite the roof being executed as a cable net (see e.g. Tomlow [141]), the general shape of the roof can closely

<sup>3</sup> design by Behnisch & Partner, Otto; engineering Leonhardt, Andrä und Partner



**Figure 3.16:** Form-finding of the roof of the *Olympiastadion München* as an isotropically prestressed membrane (recalculation)



**Figure 3.17:** Detailed view of two segments of the roof of the Olympic Stadium with the corresponding control point net

be determined by form-finding with isotropically prestressed membrane patches, resulting in minimal surfaces.

As discussed in Section 2.2.5 the NURBS-based surface description used in IBRA is very well suited for a good approximation of membrane geometries. Owing to this quality of the geometry description, the form-finding of the Olympic Stadium can be realized with a very low number of control points and – in consequence – of DOFs. This leads to short computation times for the form-finding, even for very large structures like the Olympic Stadium. To give an order of magnitude, the entire roof displayed in Figure 3.16 is described with approx. 640 control points. An exemplary detailed view

### 3.5 Application examples for lightweight structures with IBRA

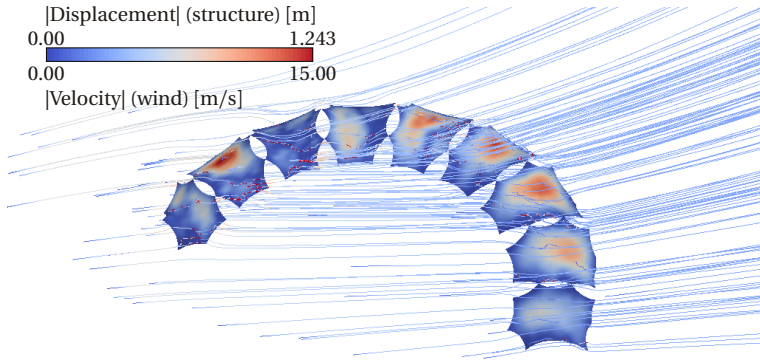


**Figure 3.18:** Application of the form-found IBRA model of the Olympic Stadium within a fluid-structure interaction simulation, see [109] (©C. Osorio, with kind permission)

of two segments with the corresponding control point net is depicted in Figure 3.17.

The form-found isogeometric model illustrated in Figure 3.16 is used by Osorio [109] within a fluid-structure interaction simulation, investigating the flow of wind around the flexible structure. Figure 3.18 displays an exemplary result by indicating the streamlines of the wind and the displacement of the roof under the wind load.

Within this investigation substantial refinement (to approx. 4000 control points) has been necessary in order to be able to reproduce the small wavelengths of the deformation of the roofs. This corresponds to the necessary refinement in order to permit the formation of the wrinkles in the bubble cluster from Section 3.5.1.

Comparative studies between a classical FEM-model of a triangulated mesh with the presented isogeometric model show very good agreement in the results of the static, dynamic and coupled simulations [109].

#### 3.5.3 Grid structures on surfaces of zero mean curvature

In their research on doubly curved grid structures, Schling et al. [129] investigate different layouts of line elements on doubly curved surfaces. These surfaces in general are advantageous for the design of networks of line

### 3 Integration of geometry and structural behavior with IBRA

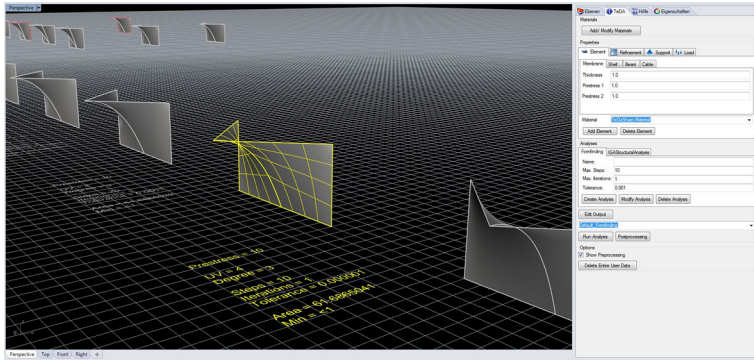


**Figure 3.19:** Accuracy assessments by Hitrec et al. [70] on the top half of the unit-cell from Figure 3.20 with regard to the minimal surface form-finding with *TeDA* [23] as a plug-in to *Rhino3D* [95]

elements since they allow the structure to bear loads like a shell, see also Section 4.1.1.

Within this research, lines of specific curvature – geodesic curves, principal curvature lines and asymptotic curves – are further examined. These curves dispose of an advantageous characteristic: they can easily be built out of planar strips since only twisting and bending around the weak axis are required. Among those lines *asymptotic curves* are curves with no normal curvature. They turn out to be especially attractive in terms of construction: Since they can be formed from straight plane strips perpendicular to the underlying surface, they are able to resist local loads by bending in their strong axis [129].

In addition, in the case of surfaces of zero mean curvature – *i.e.* minimal surfaces, see Section 2.5.3 – asymptotic curves on these surfaces are perpendicular to each other. In terms of structural design this means that all nodes are identical for an ideal meeting angle of 90°.

However, the determination of a network of asymptotic curves on a surface is a complex task on its own, which has to be solved in an iterative procedure [129].

For the determination of these asymptotic curve networks, the smooth NURBS-based surface descriptions of minimal surfaces that are form-

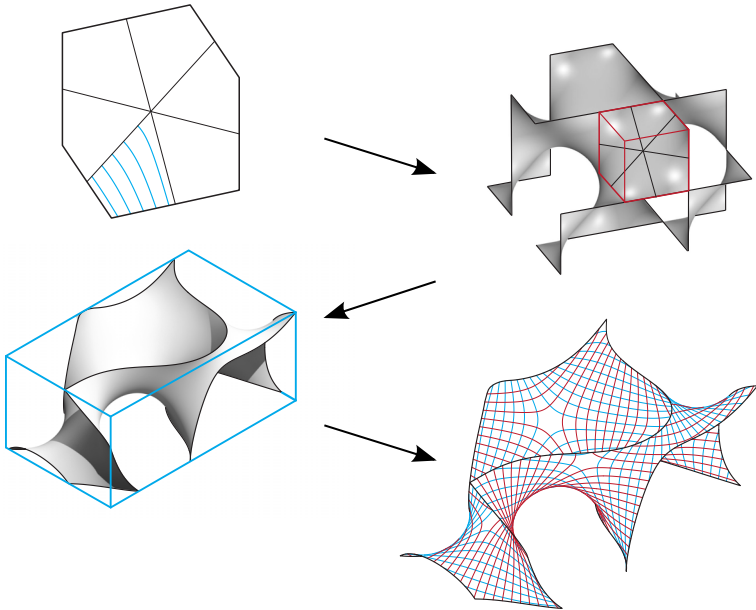


**Figure 3.20:** Definition process of the *Asymptotic Pavilion* from form-finding and asymptotic line determination on the unit-cell (top left) to the final layout of the asymptotic lines (bottom right) [70, 129] (©D. Hitrec [70],E. Schling [129], with kind permission)

found with the developments presented within this thesis have been used. This has turned out to be an ideal basis: On the one hand, Hitrec et al. [70] have realized comparative studies of the quality of the obtained surfaces (measured in terms of surface area as well as maximum mean curvature). A screen-shot of those comparative studies is displayed in Figure 3.19. Here it has been shown that the quality of the resulting surfaces with the developed IBRA form-finding is excellent, better than with any tested commercial environment. On the other hand, the smoothness of the surface description and direct availability of entities like continuous fields of surface normals is a big advantage in the development of the necessary algorithms for the determination of the network of asymptotic curves [70].

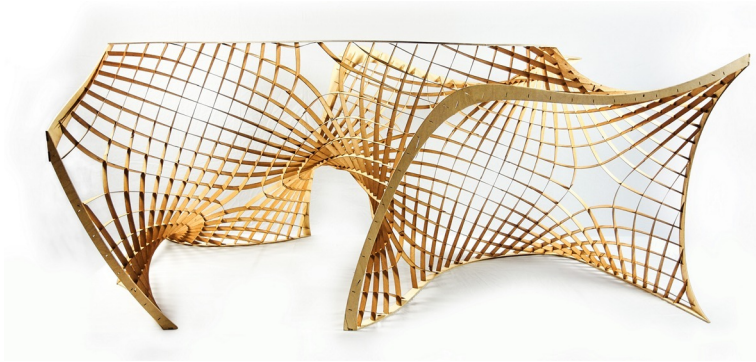


**Figure 3.21:** Mock-up of the *Asymptotic Pavilion* in scale 1 : 5, realized from plane, straight beech veneer strips (©D. Hitrec [70] and E. Schling [129], with kind permission)

Based on the "unit-cells" that are also depicted in Figure 3.19, Hitrec et al. [70] have developed the *Asymptotic Pavilion*. The form definition process based on the form-finding of a minimal surface is described in Figure 3.20. A first mock-up of the *Asymptotic Pavilion* in scale 1 : 5, shown in Figure 3.21, has been realized from plane, straight beech veneer strips to check for the ease of assembly and the principle load-bearing behavior.

### Summary and conclusion of Chapter 3

Within this chapter, the integration of geometry and structural behavior of lightweight structures with the help of a recent finite element technique, the *isogeometric B-Rep analysis* (IBRA), has been presented.

In regard of the application to membrane structures, notably the following aspects and developments have been in the focus:

- IBRA as an analysis technique has briefly been presented.
- The necessary components for the form-finding and analysis of membrane structures have been developed, mainly the formulation of a prestressed membrane element and an embedded cable element following the novel paradigm of *B-Rep edge elements*.
- The developed components have been successfully evaluated for their accuracy, robustness, speed and flexibility in application.
- With the help of selected applications the potential and ability of IBRA for a wide field of lightweight structures has been assessed.

Overall, IBRA has revealed substantial advantages in the design and analysis of membrane structures for the noted aspects like a smooth CAD-CAE-integration or the quality of the surface representation.



## THE INTERACTION OF DEFORMATION AND STRUCTURAL BEHAVIOR

Besides their geometry, lightweight structures and their load-bearing behavior also depend on their deformation. Lacking bending rigidity, tensile structures like structural membranes or cable nets rely on deformation to adapt to different load cases, see Section 2.5.1. The presence of prestress in those membrane structures already results from an initial deformation from the plane unstressed cutting-patterns to their spatial assembled configuration, see Sections 2.5.2 and 5.4.1.

Investigating the deformation of structures in general, two types of deformation can be distinguished:

- the deformation as the reaction of a structure to a specific load scenario as mentioned above and
- the planned deformation during the erection process of a structure that is used to modify and adjust the load-bearing behavior or shape of that structure.

Within this chapter, the latter kind of deformation will be discussed. Therefore selected realized examples for this kind of structures are presented at first. The analysis of the impact of deformation on the load-bearing behavior by means of a construction stage analysis is discussed focusing on geometric non-linearity. Based on these considerations, the consequences and prerequisites for the modeling and analysis of lightweight structures are investigated. Concluding this chapter, demonstrator examples illustrate the discussed effects and reveal critical aspects of the simulation of these structures.

**Remark I:** The structural analyses within this chapter have been performed with classical finite elements within the FE-code *Carat++* [29]. Nevertheless it should be mentioned that the findings of this chapter apply as well to isogeometric analysis (presented in Chapter 3), of course.

**Remark II:** In parts the content of this chapter has been published in Philipp et al. [113, 117] and Dieringer et al. [50] (co-authored). For the sake of easier readability these sources will not always be cited explicitly.

### 4.1 Deformation-based structures

Most structures in civil engineering are built from undeformed members: Relatively rigid elements like bricks or steel members are assembled or concrete is poured into formwork which is only removed when the concrete has reached sufficient stiffness and resistance. These structural elements deform under the applied loads. Commonly, deformation is considered an effect that has to be limited, which is also assessed in the verification of structures, see Chapter 5. It should be noted that – even for conventional structures – the deformation of structural elements during the construction stages might have to be considered, as discussed in Section 4.2.1.

In contrast, there are types of structures that actually gain their shape definition from the large deformations during their building process. The structures that are in the focus of the present chapter mainly rely on bending deformation, in order to create or increase the curvature of a structure. At a first glance, bending seems to contradict the principles of lightweight construction: Structures acting only along their center-line resp. mid-surface (see Figure 2.1) can be stressed – at least theoretically – until their ultimate stress  $\sigma_u$  is reached. Since the stress distribution is uniform, *i.e.*

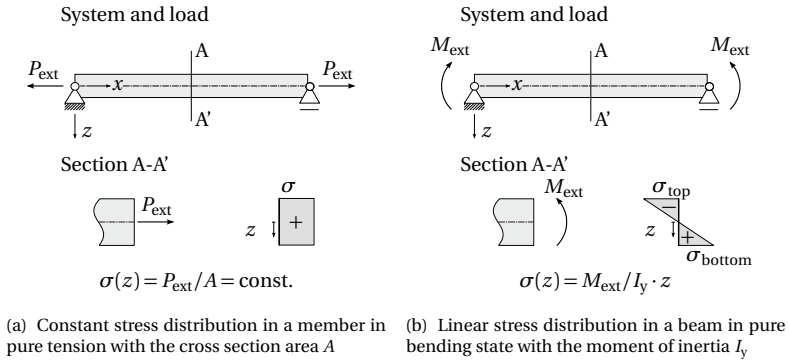


**Figure 4.1:** Stress distributions in a member in tension resp. bending assuming linear elastic material and plane cross sections

constant along the cross section, the whole member is utilized entirely as depicted in Figure 4.1(a). Assuming linear elastic material behavior and plane cross sections, bending stresses increase linearly from the center to the external edges of the member. When the ultimate stress  $\sigma_u$  is reached at the maximum distance from the center, close to the center the fibers are barely stressed yet. Consequently, the cross section is not uniformly utilized, see Figure 4.1(b).

#### 4.1.1 Gridshells – Creating curvature through bending

According to Happold et al. [67, p.101] the term *gridshell*<sup>1</sup> refers to "a doubly curved surface formed from a lattice of timber laths bolted together at uniform spacing in two directions". Obviously there are gridshells which are built out of curved members or even by assembling linear segments to a spatial structure. However this type of gridshells requires the production of initially curved elements resp. expensive connection details and very often also expensive scaffolding during the assembly.

Opposed to that approach is the concept of creating curvature, here doubly-curved shapes, through bending. The main motivation for the bending-induced curvature is the usage of initially straight members with the aim

<sup>1</sup> Often the term *lattice shell* is used instead in earlier publications, as in [67].

of reducing the cost of such structures. This advantage in cost is mainly due to the easier production and transportation of straight members. Evidently, several aspects need to be considered, when substantial bending is introduced in the members during construction:

- What are the limits of this bending during the erection of the structure? For efficient and economic structures it should be avoided that the mounting process leads to the highest stresses and hence determines the dimensions of the structure.
- How can the mechanism that has been used to realize the double curvature be blocked such that the structure becomes (more) stable after the mounting process?
- To what extent does the elastic deformation during the erection of the structure influence its load-bearing behavior?

Two selected examples are briefly introduced in the following to illustrate the possibilities and the range of application of creating curvature through bending.

#### **Multihalle Mannheim**

The *Multihalle Mannheim*<sup>2</sup> was built for the German federal garden show 1975. It certainly is a seminal project for this type of construction, as well due to its pioneering way of construction as by its dimensions, covering roughly 10000 m<sup>2</sup>. As described by Burkhardt et al. [39] and Happold et al. [67] the shape was determined through hanging-chain models by Frei Otto and his team, from where spatial coordinates of nodes of the gridshell were measured. On site, a uniform pin-jointed double-layer lattice of timber laths, spaced by 0.5 m, was laid out as depicted in Figure 4.2(left). With the help of forklifts and temporary scaffolding towers, the lattice was pushed into its final geometry, see Figure 4.2(right).

In order to lock the in-plane shear deformation, the joints were then fixed and additional diagonal steel cables were introduced in order to guarantee sufficient shear stiffness in the gridshell. Along the edge of the membrane, proper boundary conditions had to be realized to support the in-plane

---

<sup>2</sup> design by Mutschler, Langner, Otto; engineering by Ove Arup & Partners

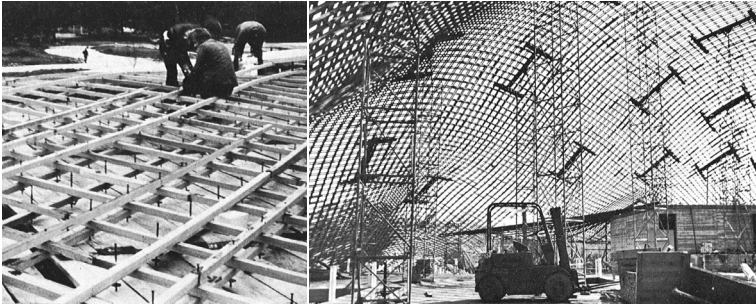


**Figure 4.2:** *Multihalle Mannheim*: lay-out of the lattice (left) and lifting with the help of forklifts and temporary towers (right) (both from [39], ©Atelier Frei Otto + Partner, with kind permission)

load carrying of the gridshell structure. Finally a PVC-coated polyester membrane was installed as cladding.

Since relatively small radii of curvature were realized in the shell (down to only 6 m), high bending stresses occur, even with full shear flexibility. These induced bending stresses have been the subject of intensive investigations. Relying on the mechanical characteristics of timber, Happold et al. [67] argue that an important part of the bending stresses relax due to creep in the material. Early computer models were set up to analyze the global behavior. Besides verification of the ultimate stresses, the shell structure is susceptible to instability, which was verified in a buckling analysis as described in Section 2.4.2.

The Multihalle can still be seen as one of the biggest examples of "bent curvature" ever realized. Especially with respect to the computational possibilities of that time, the Multihalle – as the roof of the Olympic Stadium in Munich presented in Section 3.5.2 – can be called one of the seminal works for further development of lightweight structural engineering.

### **Cathédrale éphémère de Créteil, Paris, France, 2013**

Within the last decades, gridshells as "*bending-active*" structures live to see a certain renaissance. As stated *e.g.* by Lienhard et al. [86] this is mainly due to increased computational possibilities, facilitating the shape definition and analysis of these structures, and to the material properties of fiber-

reinforced polymers (FRP). FRPs unite both properties required for highly curved gridshells made out of initially straight members, see [85, 86]:

- To be able to withstand the stresses induced by the initial bending, their strength-to-stiffness ratio (*i.e.* the ratio of permissible bending strength  $\sigma_u$  and Young's modulus  $E$ ) has to be high.
- Furthermore, the breaking strain  $\epsilon_u$  needs to be sufficiently high to be able to undergo the required deformations.

The long-term behavior of the material has to be adapted to the application, since creep may act beneficially, as it has been the case for the *Multihalle*, or may lead to a loss of prestress, which will be of interest for the hybrid structures discussed in Section 4.1.2.

The *Cathédrale éphémère de Créteil*<sup>3</sup> is a temporary religious building, covering 350 m<sup>2</sup>. Its construction process corresponds more or less to that of the *Multihalle*: Laying out a regular (square) two-layer grid, lifting it to its final position, stiffening, cladding. As described by Peloux et al. [111] and Tayeb et al. [139], the first important difference comes with the material applied: Here pultruded composite tubes from GFRP (glass-fiber reinforced polymers) have been used. With their competitive price and their very low weight, these are very attractive for the application in structures which need to be deformed and lifted "in one piece", as shown in Figure 4.3 (left). Earlier studies with pultruded FRP-tubes by Douthe et al. [54] and Tayeb et al. [138] have identified scaffold swivel couplers to be well suited as pin-joint connections between the layers. As bracing, a third layer of tubes is attached following the diagonals of the lattice once the grid is lifted to its final shape and the edges are fixed, see Figure 4.3 (middle). In combination, the bracing and the edges again allow the lattice to act as a shell globally. The overall dimensions allowed for the installation of a continuous PVC-coated membrane without *in situ* welded joints, see Figure 4.3 (right).

From both structures, the *Multihalle* and the *Cathédrale éphémère*, some common observations can be made. The possibility to build up gridshells from an initially flat lattice relies on the absence of in-plane shear stiffness.

---

<sup>3</sup> Ephemeral cathedral of Créteil (Paris, France): designed and engineered by T/E/S/S atelier d'ingénierie and the Navier Laboratory; more information on [www.thinkshell.fr](http://www.thinkshell.fr)



**Figure 4.3:** Ephemeral Cathedral of Cr eteil – a gridshell in FRP constructed through elastic bending: Lifting of the grid, bracing by a third layer and covering with a PVC-coated membrane  
( Camille Moissinac, used with kind permission)

Unlike for fabrics, which require a cutting-pattern generation as presented in Section 2.5.2, the absence of in-plane shear stiffness leads to large geometrical freedom. In principle, a doubly-curved and in consequence non-developable shape thus can be developed. However, the analysis of these gridshells still is very complex and even small geometric deviations might lead to failure through global buckling of the shell or compression buckling in the bent tubes, see Tayeb et al. [138].

Whereas in these structures the gridshell is autonomous, *i.e.* independent of its cladding membrane, the structures discussed in the following section try to short-circuit the internal forces rather than to hand them to the supports.

#### 4.1.2 Hybrid structures – The combination of tension and bending

As defined by Dieringer et al. [50, p.149], *"hybrid structures, in general, are structures which combine a certain number of principal structural elements or materials. The idea is to combine them in a way that each member is acting in its "preferred" structural state."* A beam out of reinforced concrete may be the most prominent example for a beneficial combination of materials: Whereas the steel reinforcement bar takes the tension stresses from bending, concrete takes the compression (and protects the steel against corrosion). In the present context of lightweight structures, the term "hybrid" refers to a beneficial combination of bent and tensile mem-



(a) Entry arch to the German federal garden show 1957 ([38], ©Atelier Frei Otto + Partner, with kind permission)



(b) *Bat-sail* developed by Off [107] with integrated GFRP rods to increase the covered area (©Robert Off / IMS-institute, with kind permission)

**Figure 4.4:** Full-scale examples for integrated bending-active elements in compression in lightweight membrane structures

bers. Several selected examples shall introduce this combined behavior and serve as a basis for the discussion of the mechanical effects that occur.

### Membrane restrained arches

The *Entry arch* to the German federal garden show 1957 (Cologne, Germany) by Frei Otto is a very prominent example for the combination of bending and tension: The very slender supporting arch<sup>4</sup> has been produced with an initial curvature. The arch is further loaded by the prestressed membrane, for which it serves as a line support, see Figure 4.4(a). Thus at the same time, the arch as a support with varying height introduces curvature into the membrane, whereas the membrane restrains the arch from tilting and lateral buckling.

Recent projects make even more accentuated use of this "symbiotic" effect: The *Bat-sail* by Off [107], illustrated in Figure 4.4(b), includes initially straight GFRP splines into the membrane. The very slender beams spread the opposite edges of the membrane and in return are compressed by that spreading. Owing to the very thin diameter of the rods, the restraining by the membrane is necessary to prevent buckling of the bending active members.

<sup>4</sup> The steel arch spans 34 m, with a tubular cross section of  $171 \times 14$  mm [38, 81].



**Figure 4.5:** *Umbrella for Marrakech*: Finalized structure and detail of inclusion of the bent arms (©J. Lienhard [85], used with kind permission)

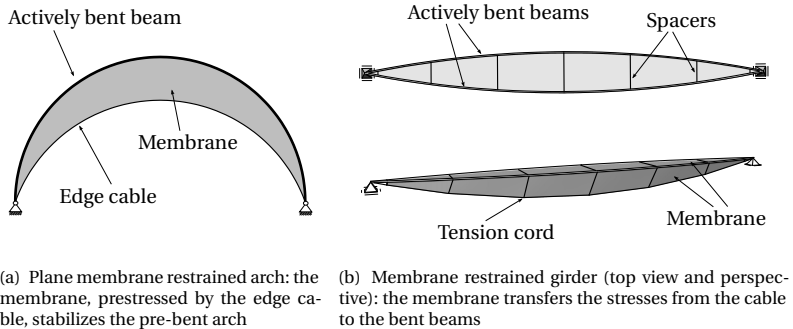


**Figure 4.6:** Plane membrane restrained arch and spatial membrane restrained girder (remade based on [3, 4])

An example of larger scale is the *Umbrella for Marrakech* as described by Lienhard et al. [87], illustrated in Figure 4.5. Here as well GFRP rods are introduced in pockets of the membrane. The free ends of the rods create additional corner points, increasing the covered area of the umbrella structure. Again, the membrane stabilizes the beams against buckling. An eccentric attachment of the beams to the membrane stabilizes the beam also against out-of-plane buckling, see Lienhard [85].

The investigations by Alpermann [2–4] on membrane stiffened arches give a more detailed insight into the interaction of bent members and

restraining tensile components. Besides stabilization against buckling, considerable reductions in deformation resp. a considerable increase of the stiffness can be obtained for the case of the plane arches, see Figure 4.6(a). Extending the idea to the spatial case leads to a membrane restrained girder, presented in [4], which is a combination of two bent rods, a tension cord, a restraining membrane and short spacers, as depicted in Figure 4.6(b). Here all members act in their favorable way. The stabilization against buckling of the upper belt by the membrane allows to significantly increase the ultimate load capacity of the girder as documented in [2].

### Selfstressed bowstring footbridge

The selfstressed bowstring footbridge by Caron et al. [40] makes use of the advantageous characteristics of FRP mentioned above and mainly follows the same idea as the membrane restrained girder. A mock-up of the selfstressed bowstring footbridge in scale 1 : 10 is shown in Figure 4.7.



**Figure 4.7:** Mock-up of the selfstressed bowstring footbridge in scale 1 : 10 (©J.-F. Caron [40], used with kind permission)

For the bow of the footbridge a pultruded pipe is used, whereas the rest of the structure consists of cables as tension members. The mounting process, illustrated in Figure 4.8, can briefly be described as follows: In a controlled buckling procedure (see Section 2.4.2) with the help of a pretensioning cable, the initially straight bow is bent, even beyond its final position. One longitudinal cable and a web of stay cables are attached without prestress. By releasing the pretensioning cable, the supports move apart and thus introduce prestress in the longitudinal cable and the web of stay cables. Hence the tension members "lock" the elastically bent bow, leading to the term *selfstressed*.

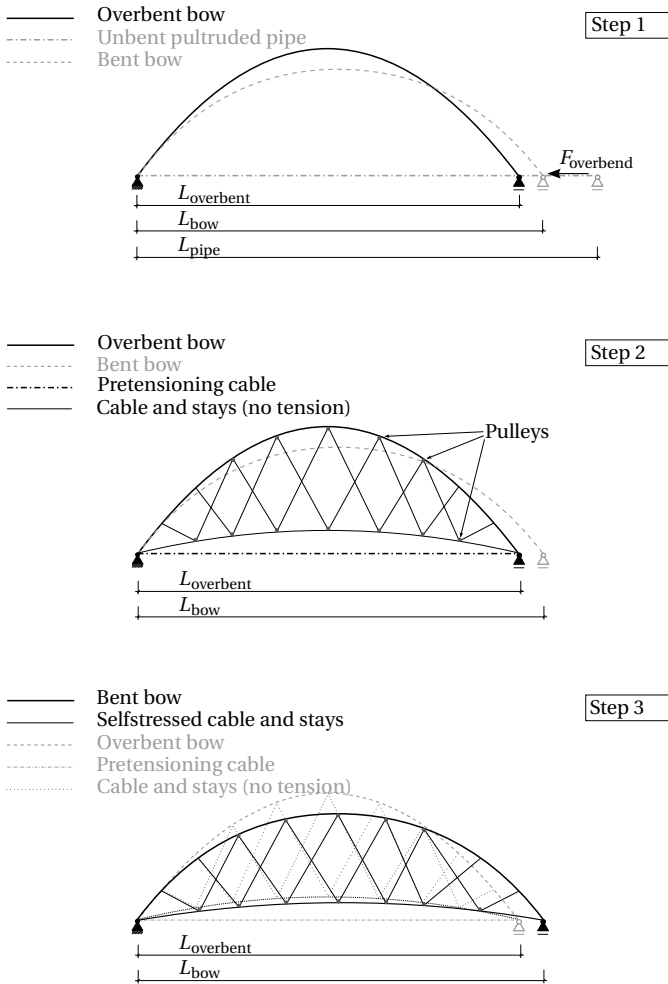


**Figure 4.8:** Selfstressed bowstring footbridge: description of the mounting process in 2D (remade based on [40])

Whereas all the steps for one arch cited above can be realized in a plane, *i.e.* lying on the ground, the spatial assembly and stabilization is realized through two of these arches leaning against each other, see [40].

### **Conclusions for the combination of tension and bending**

To conclude, both the *Marrakech umbrella* and the *Selfstressed bow-string footbridge* are examples for structures, where the bending of a member and the tensile components "interlock", *i.e.* after their mounting, the internal stress states – at least for the most part – short-circuit each other. Hence, the structure can be placed without excessive horizontal support forces due to prestress resp. pre-bending in the structure.

This use of pretension in bending (pre-bending) in order to prestress other structural members and thus define the shape and behavior of the structure is sometimes referred to as *active bending*, see *e.g.* Lienhard et al. [86].

Among the crucial contributions of the tensile components is the buckling stabilization of the elastically bent members under compression. As long as buckling is prevented, the stiffening effect of prestressing in compression and bending can be fully utilized, see Alpermann [2] and Lienhard [85].

Although the presented prototypes show very attractive characteristics, large scale structures beyond rather academic resp. sculptural applications have not yet been realized to my best knowledge. Several possible explanations for that can be given: At first, controlled buckling will be even more complicated to realize at a larger scale. Additionally, the FRP-profiles applied in the examples mentioned above are very sensitive with respect to local perturbations. The FRP-tubes show considerable creep and joints between sections are difficult to realize. Nevertheless, with advances in the material research of FRPs, the potential lying in this type of structures might be further exploited in the future.

In the following, the prerequisites and limits for the analysis of this type of structures, relying on their mounting procedure, shall be discussed.

## **4.2 Including deformation in structural analysis**

Commonly, deformation is seen as an effect to be considered resp. limited in structural analysis. In contrast, in the examples cited in Section 4.1, deformation is treated as a design handle. However, for both points of

view the ability of tracking deformations and their impact on the structure is crucial and increasingly challenging, the softer and lighter structures become.

This section gives an overview of existing approaches to consider deformations in the analysis of structures for the case where those deformations have a considerable impact on the load-bearing behavior. Therefore the application of construction stage analysis in structural engineering is introduced and its importance and limits are discussed. Special attention is paid to the aspect of geometric non-linearity in combination with construction stage analysis.

### 4.2.1 Construction stage analysis in structural engineering

Construction stage analysis, *i.e.* the consideration of the predetermined construction process in the analysis, is an aspect of structural analysis that is rarely considered up to now. However, the importance of construction stage analysis is increasing for several reasons: Besides ever lighter structures with higher, possibly planned deformations (see Section 4.1) and special construction techniques like incremental launching in bridge construction, also the available tools for structural analysis have changed.

With increasingly powerful modeling and computation environments available, structural analysis is frequently realized with the help of integral spatial structural models. Bischoff [22] describes this trend and notes that the control over the flow of forces is lost, at least in parts, when these integral models are compared to the analysis of separate extracted (often plane) partial models, which has been standard up to now.

Commonly integral models are modeled as one piece, so to say in a "*gravity-free environment*", and then loaded, see Löwenstein [90]. Thus, the deformation from earlier stages (*e.g.* the compression of lower stories of a high-rise building) is not taken into account for the analysis of later stages (here the top stories). This can lead to considerable deviations in the displacements and in the resultant forces as is documented *e.g.* in [22, 90].

**Construction stages for a multi-story frame**

With the prototypic example of a multi-story frame (based on the example discussed by Bischoff [22] and Löwenstein [90]), different approaches to take the effect of the construction sequence into account are discussed.

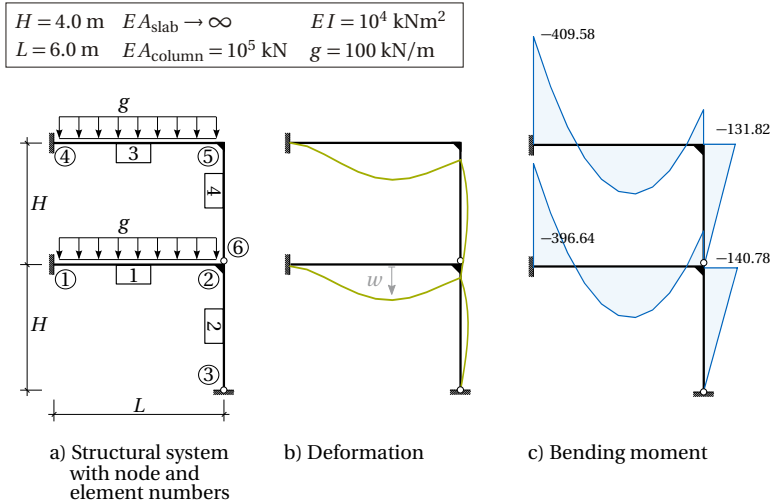


**Figure 4.9:** Prototypic example for the construction stage analysis of a multi-story frame and results of an integral analysis of the system (example based on [90])

Therefore, the system described in Figure 4.9(a), representing a simplified two-story building, is analyzed. The clamped supports at the left represent the connection of the slabs to the core of the building which is assumed infinitely stiff. This common assumption is justified by comparing the stiffnesses in the structure. The slabs themselves are considered as beams with an infinite axial stiffness  $EA_{\text{slab}}$ , a bending stiffness  $EI$  and a self-weight  $g$  which is taken into account as the exclusive load case. The supporting columns share the same bending stiffness but have a finite axial stiffness  $EA_{\text{column}}$ . Moreover their self-weight is neglected.

The first approach to the problem consists in analyzing the integral problem, which is illustrated in Figure 4.9(b) and (c). Here the structure is

assumed to be constructed in one piece and self-weight is only applied after completion of the structure.

Obviously the integral model does not reflect the construction sequence of the building. Commonly multi-story buildings are built in stages where each story represents one stage. Under this assumption, there are two construction stages<sup>5</sup> to be considered.

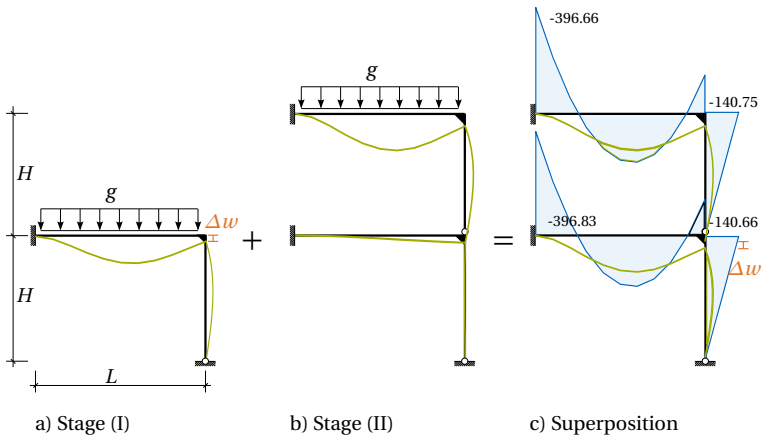


**Figure 4.10:** Construction stage analysis of the multi-story frame through *change of system* as a superposition; the resulting bending moments are indicated in blue (example based on [90])

A first attempt to account for the impact of the construction sequence, the "*Change of system*" [90], is illustrated in Figure 4.10. Here each construction stage is treated separately, acting on those parts of the final structure, which have already been built up to the considered stage. It is important to point out that for each analysis the system is considered in its undeformed, initial state, see Figure 4.10(b).

The results for each construction stage correspond to the superposition of the respective quantity in all stages up to the one under inspection. In Figure 4.10 this superposition has been realized for the displacements  $w$

<sup>5</sup> In general *construction stages* of a structure reflect characteristic moments in its *construction process* which at its turn is measured with a pseudo-time  $t$ .

and the bending moments  $M_y$ . The gap  $\Delta w$  at the junction of the first and the second story corresponds to the displacement from the first construction stage. In reality, this gap would have been closed through local adaptations, either by producing the column of the second floor longer (i.e. with a length  $L_{\text{column } 2} = H + \Delta w$ ) or by the use of shim plates.

An alternative method for the construction stage analysis consists in the "Compensation of deformations" [90]. Here the adjustments on site for taking the "gaps" into account are considered in the analysis. Each construction stage represents an individual problem.

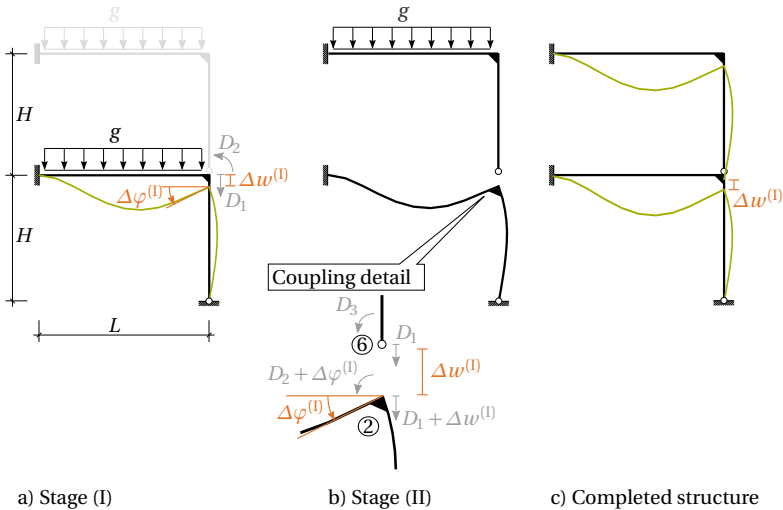


**Figure 4.11:** Construction stage analysis of the multi-story frame through *compensation of deformations* (example based on [90])

As illustrated in Figure 4.11 (a), the first stage is equivalent to the analysis with the *change of system*-approach [90]. The resulting deformations are characterized by the degrees of freedom (DOFs)  $D_1$  and  $D_2$ . For the next stage, they are stored as initial deformations  $\Delta w^{(1)}$  and  $\Delta \varphi^{(1)}$ , respectively. The superscript in Roman numbering indicates the corresponding construction stage from which the initial displacements result.

The detail represented in Figure 4.11(b) illustrates the assignment of degrees of freedom for the structural system of the second construction stage: The first story is already deformed by the load from step (I), expressed through  $\Delta w^{(I)}$  and  $\Delta\varphi^{(I)}$ . The second story is coupled to the first through the assignment of corresponding DOFs to double nodes<sup>6</sup>: Although they share the same DOF (here  $D_1$ ), the foot-point of the column of the second story (node 6) and the corner of the lower frame (node 2) are distant by the gap  $\Delta w^{(I)}$  which is applied as an initial deformation. Using the same DOF assures that the two nodes share the same deformation but preserve this gap. In the present case the initial rotation  $\Delta\varphi^{(I)}$  does not have an effect since the stories are linked through a hinge and hence the rotations of nodes 6 and 2 are independent anyway. Nevertheless it is quite convenient to apply the initial rotation  $\Delta\varphi^{(I)}$  since in consequence each stage delivers only the additional deformations introduced during their realization.

The results of the completed structure can be read directly from the last step: Since the initial deformations accounted for in the coupling of the doubled nodes already included earlier stages, the whole history is represented by the deformations and resultant forces obtained in the last stage. Figure 4.11(c) shows the deformed configuration of the completed structure, which is the result of the analysis of stage (II). Note that the bending moment is not represented for the finalized structure in Figure 4.11(c) since for linear computations following Th.I.O., the results are equivalent to those in Figure 4.10(c), obtained by the construction stage analysis with the *change of system*.

The simple prototypic example of a two-story frame already underlines the importance of taking construction stages into account when *e.g.* comparing the different resulting bending moments  $M_y$ . Construction stage analysis reveals considerably different results especially in cases where larger deformations occur due to softer structures or larger spans. Consequently, for the analysis of challenging structural concepts within civil engineering, reliable and robust construction stage analysis modules are required. However, of the approaches presented above, only the *compensation of deformations* may be applied to the analysis of geometrically

---

<sup>6</sup> Here double nodes refer to two (or more) nodes that share the same geometric position, but are linked to the different attached elements. They can be used to control the coupling or to model transition conditions between elements like hinges.

non-linear problems, since the other approach – the *change of system* – relies on superposition.

### Construction stages in bridge engineering

In bridge engineering, construction stage analysis is already commonly used and readily available in commercial software packages. There are several reasons, why taking the construction sequence into account is even more important for bridges than in building engineering.

Depending on their method of construction (*e.g.* incremental launching, free cantilevering or formwork on multi-span steel girders, see [96]), the structural system may change during the construction sequence.



**Figure 4.12:** *Pont de Normandie* (France), during construction in the cantilevering phase and before juncture of the two free ends  
(©Bouygues Construction, used with kind permission)

As an example, the cable-stayed *Pont de Normandie*<sup>7</sup>, built as a free cantilever, is taken. During construction, the two ends of the bridge deck act as cantilevers under horizontal wind loads. As illustrated in Figure 4.12 the final cantilever length before juncture is approximately half the bridge span. After juncture, the bridge deck between the two pylons has changed its structural system and the maximum bending moment under the same wind load decreases considerably.

Many bridges realized in all methods of construction also include temporary supports, like the red supporting towers depicted in Figure 4.13. Once these temporary supports are removed, the structural system changes

<sup>7</sup> concept and design by M. Virlogeux, architecture by C. Lavigne; see [96]

completely: The free spans the bridge has to carry increase with important effects on the resultant forces and displacements.

More in general, different members of the bridge may change their structural properties during the construction sequence: They may be removed (like the temporary supports mentioned above), added later-on (e.g. casting concrete on a steel girder with formwork) or tensioned to different levels (stay-cables resp. tension cables), just to name a few examples.



**Figure 4.13:** *Viaduc de Millau* (France), showing considerable deformations in the bridge deck during incremental launching  
(©CEVM Eiffage / Foster+Partners / JL DERU – photo-daylight.com, used with kind permission)

Whereas these examples represent a more or less sudden change of the structural system and thus represent a new construction stage, there are also continuous effects which require attention: Time-dependent effects as a consequence of stresses like the relaxation of stay-cables or creep resp. different maturities of concrete can be of crucial importance in bridge engineering, as documented by Buonomo et al. [37], Cremer et al. [47], and Mehlhorn et al. [96]. Note that these time-dependent effects are – as well as material non-linearity – not considered within the present thesis. An exemplary study of these effects in bridge engineering can be found in [1].

One of the goals of a construction stage analysis in bridge engineering is a reliable and accurate prediction of the deformations. Owing to the large spans, these cannot be neglected. As described by Buonomo et al. [37]

and Cremer et al. [47], the engineering of the *Viaduc de Millau*<sup>8</sup> included an in-depth simulation of the launching procedure in order to reliably predict the deformations (see Figure 4.13) and the tension in the stay-cables that is required to eventually obtain the planned even trajectory. The consideration of elastic deformation under self-weight of the bridge is even more important in case there are no possibilities of adjusting the trajectory after finalization. Therefore many bridge profiles are produced with a planned camber, such that eventually under self-weight, they show a smooth, even trajectory [94, 96].

Overall, many of the effects dealt with in the construction stage analysis in bridge engineering focus on system non-linearity (*i.e.* the change of systems by adding members, changing positions, etc.) resp. material non-linearity (like creep, relaxation, etc.) and on the verification of the intermediate stages. However – unlike the construction stage analysis in building constructions discussed above – the impact of the intermediate stages on subsequent steps and the consideration of geometric incompatibilities is commonly regarded of less importance.

### 4.2.2 Geometric non-linearity and construction stage analysis

As discussed in the previous section, construction stage analysis (CSA) is sometimes used in the engineering of structures. However, depending on the specific discipline and the investigated structure, CSA is applied rather rarely respectively with different aims.

Dealing with lightweight structures, the most relevant effect to be considered is their geometrically non-linear behavior. As discussed and exemplified in Section 4.1, the applied erection method and with it the construction sequence may heavily influence the load-bearing behavior and capacity of lightweight structures.

Looking at the methods for CSA that have been presented in detail in Section 4.2.1, their general applicability to geometrically non-linear structures can be assessed in the following.

The *change of system*-approach relies on superposition of the individual stages. Implicitly, the use of superposition necessitates linear behavior of the structure. In case of non-linear structures, where the stiffness  $\mathbf{K}$  of

---

<sup>8</sup> design by Foster+Partners, engineering by Bureau Greisch

the system is a function of the state, expressed in the deformation  $\mathbf{u}$ , *i.e.*  $\mathbf{K} = \mathbf{K}(\mathbf{u})$ , this assumption of linear behavior is no longer valid.

The *compensation of deformations*-approach keeps track of the deformation throughout the different construction stages, accounting for occurring kinks resp. gaps. In principle the deformation state  $\mathbf{u}$  is suitable to describe the state of a structure. Consequently, the *compensation of deformations* shall further be discussed and enhanced for non-linear modeling and analysis of actively bent structures in the following.

### 4.3 Modeling and analysis of deformation-based structures

Whereas most conventional structures are designed in their undeformed state, there are structures which rely on deformation as a shape-defining principle. Among these, the structures making use of bending in their erection resp. formation process (actively bent structures) are in the focus of the following derivations. Enlarging the focus beyond bending, one may also speak of *deformation-based structures* in general.

#### 4.3.1 Element formulations applied in the simulation of deformation-based structures

For the structures that are discussed within this chapter and have been presented in Section 4.1.2, several structural elements are required, notably

- a prestressed membrane,
- cables, also accounting for prestress,
- columns, able to withstand compression and
- beams for line members with bending rigidity.

All of these elements share the prerequisites of geometrically non-linear kinematics, accounting for the large deformations that occur for the structures in mind. Moreover, their respective DOFs should permit an easy and consistent coupling of the different structural elements.

For the membrane, the element formulation with prestress (isotropic or anisotropic using a projection scheme) presented by Dieringer [49] is used. The triangular resp. quadrilateral element with linear shape functions accounts for large displacements with its geometrically non-linear kinematics.

Cables (with prestress) and columns are both modeled using a truss element formulation, also described in [49]. The two-node element with linear shape functions is also formulated with fully non-linear kinematics.

For the beams, the corotational element formulation by Krenk [82] is applied, which has briefly been introduced in Section 2.4.3 along with selected benchmarks. It also disposes of two nodes, where at each node three translations and three global rotations are used as DOFs.

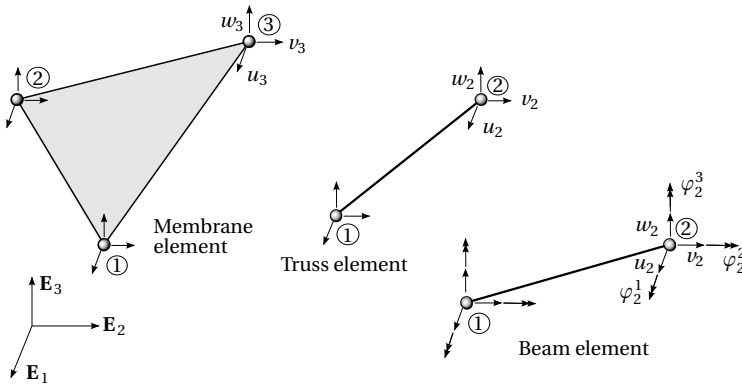


**Figure 4.14:** Element formulations with their respective (globally oriented) DOFs applied for the analysis of hybrid structures

It is important to mention that these element formulations are well suited to be applied together in a structure, since they all dispose of the same DOFs (three displacements per node; in addition three rotations for the beam). Hence a direct coupling at each common node by simply referring to the same DOFs is possible. The applied element formulations with their respective DOFs are depicted in Figure 4.14.

The correct formulation and implementation of these elements, especially of the membrane and truss element, in the in-house FEA-environment

*Carat++* [29] have been successfully demonstrated in numerous projects from academic to industrial scale. Among these, the dynamic analysis of full-scale models of foldable umbrella structures under wind as documented in Dieringer et al. [50] and Philipp et al. [117] shall be particularly mentioned in this context.

### 4.3.2 Update of configurations and coupling of elements

As described in Section 4.2.1, the core aspect of construction stage analysis is the update from one step resp. construction stage to the subsequent one. In the following the information that is necessary to perform these updates for the analysis of structures with non-linear behavior are elaborated in detail.

#### Update of configurations

In an abstract sense, non-linear structures show large deformations  $\mathbf{u}$  and considerable changes in their internal forces  $\mathbf{f}_{\text{int}}$  in each step. Therefore in principle two major possibilities to keep track of the different steps and their impact on the subsequent stage ( $i + 1$ ) exist<sup>9</sup>:

- Take the resulting geometry  $\mathbf{x}^{(i)}$  as starting configuration  $\mathbf{X}^{(i+1)}$  for the next step and prescribe the internal forces  $\mathbf{f}_{\text{int}}^{(j)}$  as given "prestress"  $\mathbf{f}_{\text{int}0}^{(i+1)}$  to the stage ( $i + 1$ ). This approach is referred to by *restart with initial stresses* or abbreviated as *InitStress* in the following.
- Keep the original geometry  $\mathbf{X}_{\text{orig}}$  and apply the (accumulated) deformation  $\mathbf{u}^{(i)}$  as initial displacement  $\mathbf{u}_0^{(i+1)}$ . This option is referred to by *restart with initial displacements* respectively abbreviated as *InitDisp* in the following.

Referring to the approaches presented in Section 4.2.1 the latter method, the *restart with initial displacements*, corresponds to the *Compensation of deformations*-approach. The *Change of system* finds its approximate

---

<sup>9</sup> Here and in the following the terms "stage" and "step" are used quite synonymously: Whereas "stage" refers rather to a built state of a structure, "step" recalls the notion of a pseudo-time  $t$ , reflecting the mounting process.

correspondence in the *restart with initial stresses*. However, the *InitStress*-approach already accounts for the change in geometry through deformation from earlier steps.

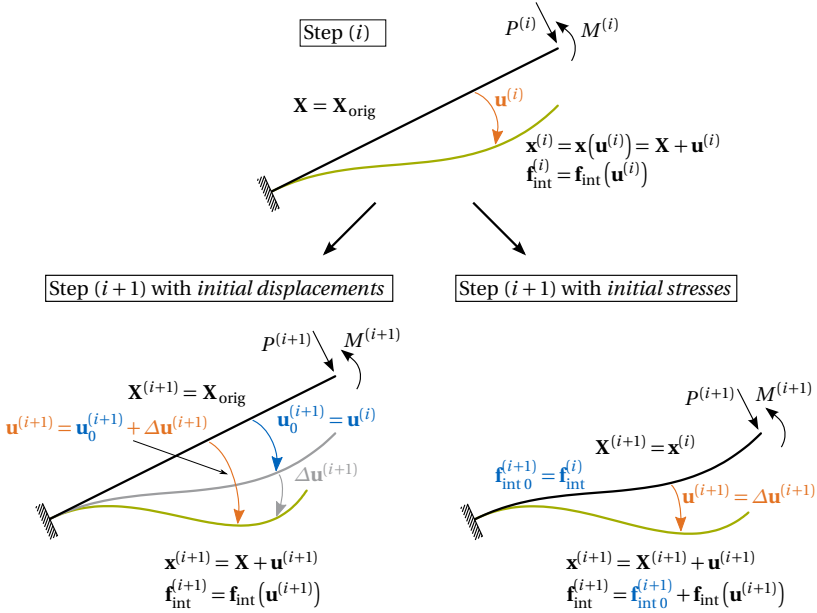
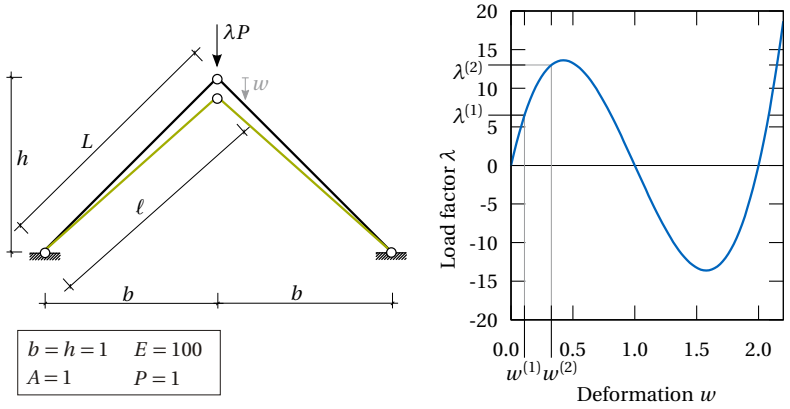


**Figure 4.15:** Different methods for the configuration update after an initial step (i) for the case of geometrically non-linear structural behavior. The respective initialized parameters are highlighted in blue.

The two update methods are illustrated in Figure 4.15 for the prototypic example of a cantilever under combined loading. After an initial step (i) the final state from that step is to be transferred to the subsequent step (i+1) with a new load combination. The parameters that are used to transfer the state from one step to the next are highlighted in blue. As can be seen with the green deformed configurations, the final resulting geometries  $\mathbf{x}^{(i+1)}$  (and with them the respective final internal force states  $\mathbf{f}_{\text{int}}^{(i+1)}$ ) differ. In the following a worked-through example of a simple *von Mises* truss shall



(a) *Von Mises* truss example and deformed configuration for a load factor  $\lambda = \lambda^{(1)} = 6.5$  (b) Analytical load-displacement graph ( $\lambda$ - $w$  graph) for the *von Mises* truss example

**Figure 4.16:** Description and analytical solution for the discussed *von Mises* truss example

highlight in more detail the differences between the two update methods and the limits of application.

### The von Mises truss as analytical example for the configuration update

Figure 4.16 shows the so-called *von Mises* truss example, a famous academic problem (see e.g. [48, 59, 82, 149] for intense discussions), which is characterized by one single DOF  $w$  for reasons of symmetry. The internal virtual work of a single truss member  $i$  can be written as

$$\delta W_{\text{int},i} = \int_{V_0} S_{11} \cdot \delta \epsilon_{\text{GL}} dV = A_i L_i (S_{11,i} \cdot \delta \epsilon_{\text{GL},i}), \quad (4.1)$$

where  $L_i$  and  $A_i$  are the length and cross section of the member  $i$ , respectively. In the two members constant strains  $\epsilon_{\text{GL}}$  (measured as Green-Lagrange strains<sup>10</sup>) and stresses  $S_{11}$  along the elements are assumed. In

<sup>10</sup> Note that for the sake of easier readability in the present context the Green-Lagrange strains are indicated as  $\epsilon_{\text{GL}}$  in contrast to the nomenclature in Chapter 2

Equation (4.1) the integration over the volume is replaced by the pre-integrated member contribution, making use of the constant strains and stresses in the truss element.

The strains  $\epsilon_{GL,i}$  in the member ( $i$ ) can be expressed as a function of the reference length  $L_i$  and the current length  $\ell_i$ ,

$$\epsilon_{GL,i} = \frac{1}{2} \frac{\ell_i^2 - L_i^2}{L_i^2}. \quad (4.2)$$

As indicated in Figure 4.16(a) the respective lengths are computed as

$$L_1 = L_2 = L = \sqrt{b^2 + h^2} \quad \text{and} \quad \ell_1 = \ell_2 = \ell = \sqrt{b^2 + (h - w)^2}. \quad (4.3)$$

Hence the equilibrium equation  $R_{\text{int}} - R_{\text{ext}} = 0$  with the external force  $R_{\text{ext}} = \lambda P$  can be expressed as

$$\lambda P = EA(h - w) \frac{2hw - w^2}{(b^2 + h^2)^{3/2}} = \frac{EA}{L^3} (w^3 - 3w^2h + 2h^2w). \quad (4.4)$$

Inserting the parameters indicated in Figure 4.16(a), Equation (4.4) simplifies to

$$\lambda P = 25\sqrt{2}(w^3 - 3w^2 + 2w), \quad (4.5)$$

which is plotted in Figure 4.16(b) for  $P = 1.0$  and varying  $\lambda$ .

In order to investigate the effects of the different configuration updates described above, two load factors  $\lambda^{(i)}$  representing two separated stages resp. steps are chosen:  $\lambda^{(1)} = 6.5$  and  $\lambda^{(2)} = 13.0$ . In Table 4.1 the numerical results for the displacement  $w$  for the selected load factors  $\lambda^{(i)}$  are given. From the solution in Equation (4.5) the analytical results for the load steps are known and serve as reference for comparisons.

The first step with a load factor  $\lambda^{(1)} = 6.5$  yields the displacement  $w^{(1)} = 0.1091417$ , as illustrated in Figure 4.16(a) in green. For the restart of step (2) two different updates are performed. The restart geometry after application of the configuration update is the same for both methods. In the case of *InitDisp* the update is realized by the initial displacement  $w_0^{(2)}$  which is identical to the prescribed change in geometry  $w^{(1)}$  that has been used to

### 4.3 Modeling and analysis of deformation-based structures

**Table 4.1:** Numerical results for the *von Mises* truss example with the parameters indicated in Figure 4.16(a)

$\lambda$	$w_{\text{analytical}}$	$w_{\text{InitDisp}}^{(2)}$	$w_{\text{tot,InitStress}}^{(2)}$
6.5(= $\lambda^{(1)}$ )	0.1091417	0.1091417	0.1091417
13.0(= $\lambda^{(2)}$ )	0.3256631	0.3256631	0.2607719

redefine the configuration for the *InitStress* approach. For the restart with initial stresses the internal force  $N_{\text{InitStress } 0}^{(2)}$  is directly prescribed as

$$N_{\text{InitStress } 0}^{(2)} = \frac{\ell^{(1)}}{L} \left( EA \cdot \epsilon_{\text{GL}} \left( w^{(1)} \right) \right), \quad (4.6)$$

where the factor  $\ell^{(1)}/L$  transfers the – unphysical – 2<sup>nd</sup> Piola-Kirchhoff stresses to the new configuration. The length  $\ell^{(1)}$  after deformation in step (1) is determined from Equation (4.3) with the displacement  $w^{(1)}$ . Consequently the vertical component  $N_{\text{InitStress } 0,z}$  is determined as

$$N_{\text{InitStress } 0,z}^{(2)} = \frac{h - w^{(1)}}{\ell^{(1)}} N_{\text{InitStress } 0}^{(2)} = \frac{h - w^{(1)}}{\ell^{(1)}} \frac{\ell^{(1)}}{L} \left( EA \cdot \epsilon_{\text{GL}} \left( w^{(1)} \right) \right). \quad (4.7)$$

For the restart with an initial displacement the resultant force is

$$N_{\text{InitDisp}}^{(2)} = \frac{\ell^{(2)}}{L} \left( EA \cdot \epsilon_{\text{GL}} \right), \quad (4.8)$$

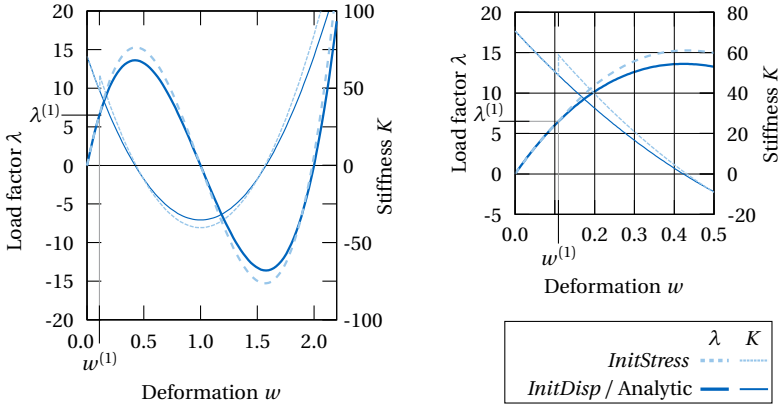
where now  $\ell^{(2)}$  results from the initial displacement  $w_0^{(2)} = w^{(1)}$  and consequently  $\ell^{(2)} = \ell^{(1)}$  for the restart. Again the factor  $\ell^{(2)}/L$  transfers the stresses to the new configuration. Hence the vertical component is derived as

$$N_{\text{InitDisp},z}^{(2)} = \frac{h - w^{(1)}}{\ell^{(2)}} \frac{\ell^{(2)}}{L} \left( EA \cdot \epsilon_{\text{GL}} \left( w^{(1)} \right) \right), \quad (4.9)$$

which is obviously identical to  $N_{\text{InitStress } 0,z}^{(2)}$  from Equation (4.7). Accordingly, both update methods yield the correct total displacements of  $w = 0.1091417$  at the start of stage (2) as can be read from Table 4.1.

Hence the update of the force state is correctly realized and equilibrium is established with both approaches. For structures with a linear or at least nearly linear behavior, characterized by a constant system stiffness

#### 4 Interaction of deformation and structural behavior



(a) Load-displacement graph and stiffness  $K$  for the different configuration update methods (b) Detailed view: discontinuous stiffness for *InitStress* after configuration update

**Figure 4.17:** Load-displacement diagram and stiffness  $K$  for the *von Mises* truss example with the respective update methods after stage (1) with  $\lambda^{(1)} = 6.5$

matrix  $\mathbf{K} \neq f(\mathbf{u})$ , the two approaches may hence be used equivalently. This again corresponds to the findings from the construction stage analysis in Section 4.2.1.

However, the stiffness of the system, which for the present single DOF example is a scalar  $K$ , is affected by the configuration update. As plotted in Figure 4.17 in dark blue, the configuration update by an initial displacement yields the same load-displacement relation  $\lambda$ - $w$  as the analytical solution. This is also reflected in the function of the stiffness  $K$  for which the analytical expression is determined from the residual force in Equation (4.4) as

$$K_{\text{analytical}} = \frac{\partial R_{\text{analytic}}}{\partial w} = \frac{EA}{L^3} (3w^2 - 6hw + 2h^2). \quad (4.10)$$

For the *InitStress* update, at  $\lambda^{(1)}$  the stiffness suddenly increases, as can be seen in the dashed light blue graphs in Figure 4.17. This increased stiffness is reflected in a slight kink in the load-displacement graph (thicker light blue lines). Although globally the behavior is still close to the analytical

#### 4.4 Applications for the simulation of the mounting process

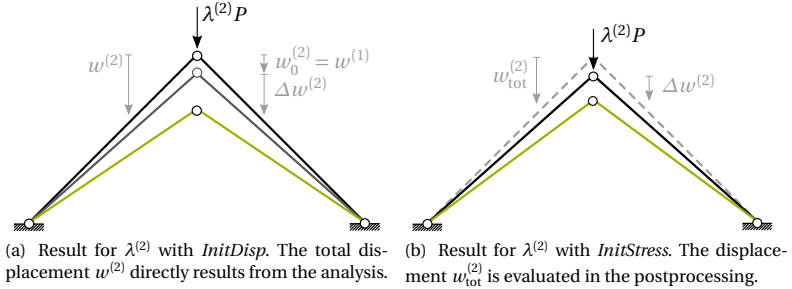


**Figure 4.18:** Final stage in step (2) with  $\lambda = \lambda^{(2)} = 13.0$  after restart with different methods for the configuration update

solution, the system behaves too stiff. This behavior can be expressed in numbers through the results in Table 4.1. For the ultimate load value of stage (2),  $\lambda^{(2)} = 13.0$ , the analytic result and the result from the *InitDisp* update coincide at  $w_{\text{analytical}}^{(2)} = w_{\text{InitDisp}}^{(2)} = 0.3256631$ , whereas the *InitStress* update underestimates the displacement by roughly 20%. Figure 4.18 illustrates the different update approaches as well as the respective results for the *von Mises* truss example.

From the example of the *von Mises* truss it can be concluded that – at least for structures with considerably non-linear behavior, *i.e.* large displacements and a stiffness  $\mathbf{K}$  that depends on the displacement state  $\mathbf{u}$  – the update by *initial displacements* is necessary to provide mechanically accurate multi-stage analyses. However, the analysis with initial displacements also entails additional challenges for the modeling and computation, as will be discussed in the next section.

#### 4.4 Applications for the simulation of the mounting process

Based on the analytical investigations carried out in the previous section, a prototypic membrane structure with an integrated bending-active member is analyzed. With the help of this example, different strategies for the correct mechanical modeling of the mounting process are presented, applied and compared.

#### 4.4.1 A follow-up structural analysis after the form-finding of hybrid structures

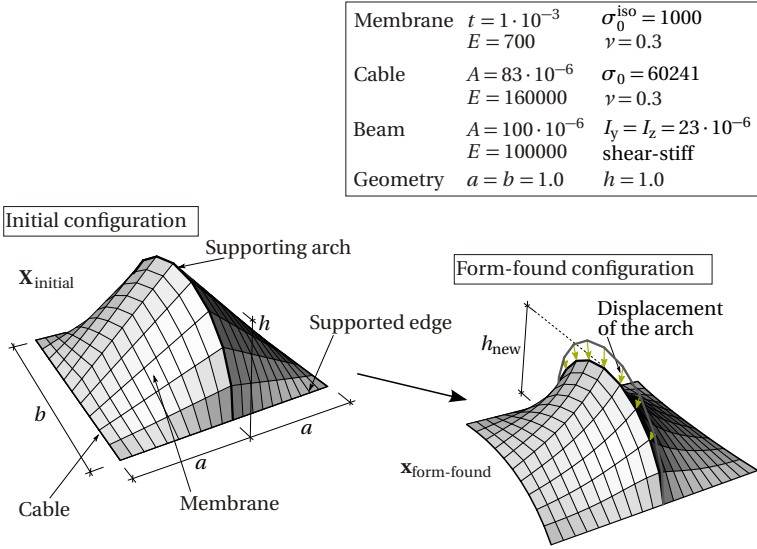
As introduced in Section 2.5.1 the structural analysis for the different loading scenarios of a membrane structure (see Chapter 5) is performed on the form-found shape of equilibrium. Whereas in pure tensile structures only prestressed membranes and cables are applied in between fixed supports, recently the integration of elastic members into the design process of structural membranes has gained more attention. These *hybrid structures* unite elastic deformation and the material-independent stress field of the form-found members in one single process. For a detailed discussion on hybrid structures, the necessary adaptations in the form-finding process and their design possibilities, see Dieringer et al. [50], Lienhard [85], and Philipp et al. [113, 117]. Within this section, the focus is on the update of the configuration from form-finding to the follow-up structural analysis by initial displacement (method *InitDisp*) as introduced in the previous section.

Figure 4.19 shows the prototypic structure of a membrane that is supported by a central arch and delimited by edge cables along two opposite ends of the membrane. For this arch, the element formulation by Krenk [82] that has been introduced in Section 2.4 is used. In its unloaded configuration the shape of the arch follows a semi-circle of radius  $R = h = 1.0$ . The dimensions and relevant mechanical properties are listed in Figure 4.19.

During the form-finding, the membrane and the cables act through their prestress whereas the arch reacts by its internal elastic forces due to the encountered deformation. The form-found shape in Figure 4.19 on the right shows the shape of equilibrium, where now the arch is compressed and bent, mainly resulting in a normal force  $N$  and a bending moment  $M$ . To give an order of magnitude, the apex of the arch deflects vertically by  $w_{\text{apex}} = -0.19451$  to give the new height  $h_{\text{new}} = 0.80549$ .

Before introducing an external load in a follow-up structural analysis the modeling of the restart with initial displacements as illustrated in Figure 4.20 is considered in detail. For the elastic member (the arch), the deformation encountered during the form-finding (see Figure 4.19), *i.e.* the difference between the initial configuration  $\mathbf{X}_{\text{initial}}$  and the form-found configuration  $\mathbf{x}_{\text{form-found}}$ , is applied as initial displacement  $\mathbf{u}_0$ . Note that

#### 4.4 Applications for the simulation of the mounting process



**Figure 4.19:** Form-finding of a *hybrid structure* with an elastic supporting arch modeled with beam elements. The displacements of the arch are highlighted in the form-found configuration.

– depending on the involved element formulations – the vector  $\mathbf{u}_0$  also might include other DOFs like initial rotations  $\varphi_{i0}$ .

As described in Section 2.5.3 the reference configuration  $\mathbf{X}_{\text{updated}}^{\text{mem+cab}}$  of the form-finding elements, *i.e.* the membrane and the cables, is updated to the configuration  $\mathbf{x}_{\text{form-found}}$ . In contrast, the reference configuration  $\mathbf{X}_{\text{orig}}^{\text{beam}}$  is the same as in the initial configuration. After applying the initial displacements  $\mathbf{u}_0$ , the geometry of the form-found shape as well as the internal stress state in all members is restored.

Besides the different configurations, Figure 4.20 also illustrates the consequences for the modeling: Disposing of two different reference configurations, the membrane and the supporting arch are now topologically separated, *i.e.* they do not share the same nodes anymore<sup>11</sup>.

<sup>11</sup> Note that the represented configuration does not reflect an equilibrium state. Equilibrium is only re-established after application of the initial displacements and the respective coupling of the DOFs

#### 4 Interaction of deformation and structural behavior

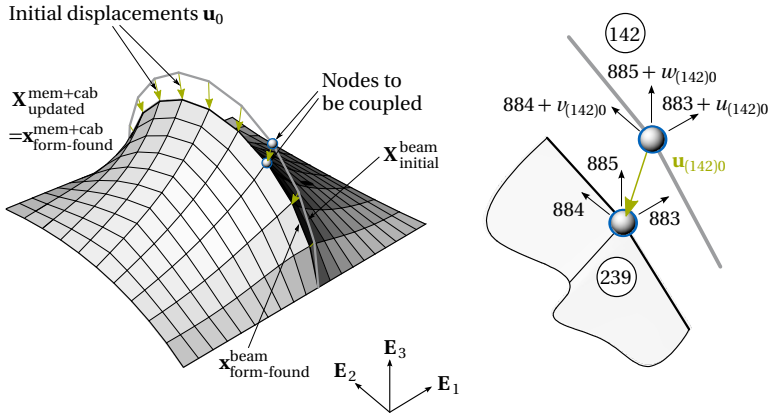


**Figure 4.20:** Configuration update by initializing displacements after form-finding. The detailed view shows the attribution of DOFs and initial displacements for exemplary doubled nodes.

During form-finding a common node and with it the nodal DOFs were shared by membrane and beam elements, thus ensuring the connection. Since for the update two separate initial configurations are required, the concerned nodes have to be doubled, leading to two related nodes like the ones highlighted in blue in Figure 4.20. A coupling of those nodes is realized by assigning the same DOFs. However, the initial displacement is only assigned to the node of the elastic member, here the beam. Figure 4.20(right) illustrates this doubling and coupling of the nodes for the example of the highlighted node: After the form-finding the original node 142 is doubled to give node 239. Node 142 stays attached to the beam and is assigned the initial displacements  $\mathbf{u}_{(142)0} = [u, v, w, \varphi_x, \varphi_y, \varphi_z]^T_{(142)0}$ . After this initial displacement, the two nodes are located at the same position. By referring to the same DOFs as indicated they share the same deformation in the sequel.

Summing up, an analysis accounting for the different stages by initial displacements has to double the concerned nodes (while keeping the correct

topological attribution of the elements), assign multi-point coupling conditions and attribute the respective initial displacements.

In a follow-up structural analysis of this example one of the two membrane fields is loaded by a snow-type surface load of  $p = 3.0$ . The displaced structure is depicted in Figure 4.21 on the right, showing the considerable deformations of the membrane. As required, the supporting arch stays attached to the membrane and – due to the asymmetric loading – also shows a slight displacement in the  $x$ -direction.

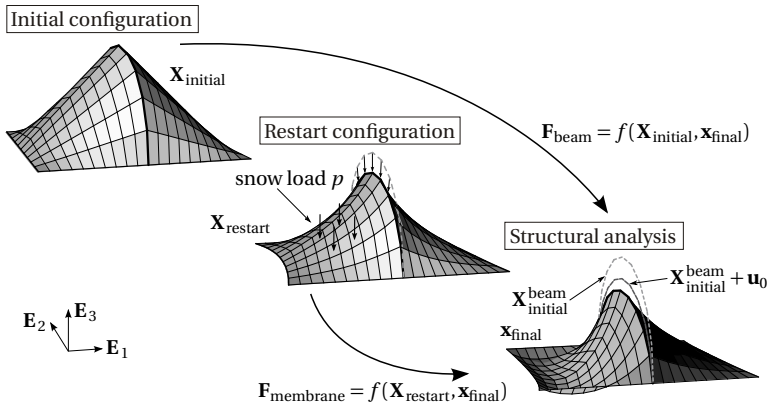


**Figure 4.21:** Different mechanical configurations for the arch supported membrane and the result of a structural analysis under a one-sided snow load  $p$ . The different mechanical configurations also affect the respective deformation gradients  $\mathbf{F}$ .

As a mechanical consequence of the different reference configurations  $\mathbf{X}$ , the corresponding deformation gradients  $\mathbf{F}$  (see Equation (2.32)) are different, even if the current configurations  $\mathbf{x}$  coincide. These different configurations and the corresponding deformation gradients  $\mathbf{F}$  are schematically sketched in Figure 4.21.

Hybrid structures which combine purely form-found components (membrane, cable) with elastic members (beams) commonly dispose of several different reference configurations  $\mathbf{X}$  for their members, requiring the proposed configuration update technique. Even pure tensile structures would necessitate that kind of analysis: The prestress that has been introduced

as a design parameter ( $\sigma_0$  or  $n_0$ , for instance) already is the result of a mounting from the plane, unstressed cutting patterns to their spatially assembled configuration, see Section 2.5.1. Hence all members – the separate membrane strips as well as the cables – dispose of different reference configurations. In consequence, a mechanically accurate simulation of the mounting process from those cutting patterns has to start from the unstressed configuration and describe the erection process by initial displacements and coupling of DOFs as described with the present prototypic example.

### **Critical aspects of the configuration update by initial displacements**

In the previous section, the construction stage analysis with initial displacements in combination with a multi-point constraint have been used to perform a mechanically accurate structural analysis after form-finding. In this example the configuration update could be realized by an initial displacement since an equilibrium configuration – the one that had resulted from form-finding – was known beforehand. However, this procedure might be critical in general for several reasons.

The required initial displacements  $\mathbf{u}_0$  and rotations  $\varphi_0$  can be large. Consequently, applying them in one single load step might present a considerable challenge for the element formulations and for the convergence of the equilibrium problem on the one hand. Whereas initial displacements have turned out to be less critical, the application of large initial rotations in one step may lead to severe problems in convergence as described in Section 2.4.1. On the other hand, the application of the initial state in several steps *a priori* contradicts the concept of the multi-point constraint coupling from the beginning of the analysis.

Moreover, in many cases, a "meeting configuration" of the different members to be coupled which is in equilibrium is not known beforehand. Especially for more complex mounting scenarios with several different elastic members to be coupled, an advantageous intermediate "meeting configuration" might be less obvious than it has been the case for the previous example. Consequently, structures with a complex deformation history often rely on "*exhaustive physical form-finding experiments*" [85, p. 79]. Thus before starting the computational analysis, a good approximation

of those intermediate self-equilibrated meeting configurations stages is determined.

For these reasons as well as for a general simplification of the problem set-up by omitting complex definitions of couplings and initial displacements, an alternative approach is proposed in the next section.

#### 4.4.2 Guided movements and coupling of structural elements with contracting cables

In the physical form-finding of bending active structures as well as in actual mounting processes, different members – be it two flexible rods or a structural membrane and the primary structure – are forced to meet at selected points. Inspired by these mounting procedures, the concept of contracting cables in order to direct guided movements and to realize the coupling of structural elements will be presented.

Contracting cables have already been applied e.g. by Lienhard et al. [84] as "*ultra-elastic contraction elements*". Bauer et al. [15] make use of a similar approach by penalizing the distance between two geometric points for mounting analyses of lightweight structures with IBRA, see Chapter 3. It should be noted that ultimately the two approaches are closely related, since both aim on adding an additional constraint – two geometrical points have to coincide – by different means: The contracting cables solve this problem by mechanical modeling whereas penalizing affects the equation system directly.

In most cases, the nodes to be coupled are intended to move to the same position. In consequence a contracting cable between those nodes would have to reduce its length to  $\ell_{\text{contracted}} = 0$ , which has to be feasible with the applied strain measure  $\epsilon$ . In the present element formulation the Green-Lagrange strain  $\epsilon_{\text{GL}}$  has been used, see Equation (2.34).

As illustrated in Figure 4.22 for line elements, characterized by their lengths  $L$  resp.  $\ell$ , the Green-Lagrange strain measure shows no singularities and is also well-defined for a length  $\ell = 0$ , where it is determined to be

$$\epsilon_{\text{GL}}(\ell = 0) = \frac{1}{2} \frac{0 - L^2}{L^2} = -\frac{1}{2}. \quad (4.11)$$

#### 4 Interaction of deformation and structural behavior

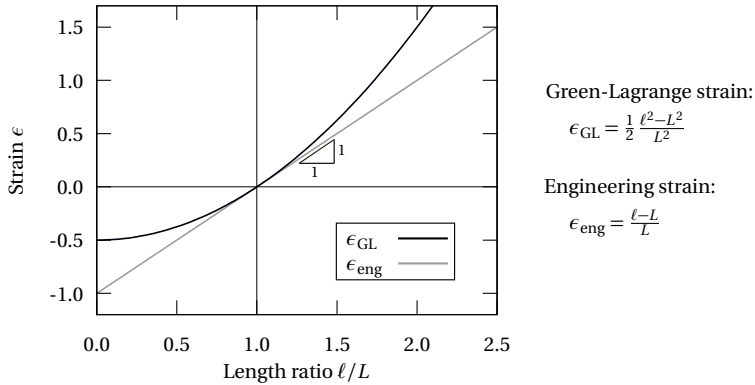


**Figure 4.22:** Plot of the Green-Lagrange strain  $\epsilon_{GL}$  for line elements, with the engineering strains  $\epsilon_{eng}$  as a reference

In combination with the Young's modulus  $E_{cable}$  and applying the St. Venant Kirchhoff material law, see Equation (2.40), the corresponding stress required to obtain this length  $\ell = 0$  is

$$S_{compression}(\ell = 0) = E_{cable} \cdot \epsilon_{GL}(\ell = 0) = -\frac{1}{2} \cdot E_{cable} \cdot \quad (4.12)$$

For the contracting cables this force shall be applied as a prestress  $S_0$ . Since the goal is to exert force on the members to be joined and not on the cable itself, the Young's modulus  $E_{cable}$  of the cable is reduced as much as numerically possible. Thus, eventually the prestress is entirely acting on the two attached nodes with the force

$$N_{contraction} = \frac{\ell}{L} \cdot S_0 A = \frac{\ell}{L} \cdot N_0^{PK2}, \quad (4.13)$$

where  $\ell/L$  transfers the unphysical 2<sup>nd</sup> Piola-Kirchhoff stresses to 1<sup>st</sup> Piola-Kirchhoff stresses. The resulting force is oriented along the straight connection between the geometric location of those nodes in the current configuration.

In order to join two points, the prestress  $S_0$  could be chosen arbitrarily high in theory. However using too high values might lead to numerical instabilities. Nevertheless, the application of contracting cables that will

be shown with the help of selected examples, has turned out to be quite robust and flexible.

### Cantilevers with large deformations

For the first example, a reference solution has to be established at a first place. Therefore the system depicted in Figure 4.23 is analyzed. The obtained displacements indicated in Figure 4.23 match the reference results by Krenk [82] very well.

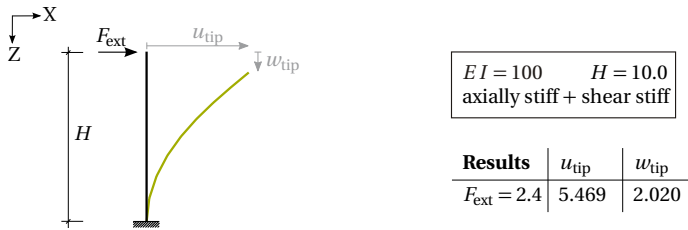


**Figure 4.23:** Cantilever with a tip load: Problem definition and deformed configuration with numerical results

Now the external load  $F_{ext}$  is "replaced" by a contracting cable spanned between the free ends of two cantilevers as depicted in orange in Figure 4.24. With a distance of  $B = 12.0$  between the two cantilevers, a full contraction of the cable corresponds to a larger bending of the cantilevers than in the reference case from Figure 4.23. Due to the symmetric problem setup, only the tip-deformations of the left cantilever are tracked.

At first, in scenario (I) this complete contraction to  $\ell_{cable} = 0$  is examined. Choosing a very high level for the prestress  $N_0^{PK2}$  (here  $N_0^{PK2} = 10000$ ), the two cantilevers touch nearly perfectly: The resulting tip-displacement in x-direction is  $u_{tip} = 5.998$ , which corresponds very well to the expected  $u_{ideal} = B/2 = 6.000$ . It is interesting to note that the current length of the cable in that scenario, measuring the persisting gap, has diminished to ultimately  $\ell_{cable} \approx 0.004$ . Seen in terms of the large deformations and possible applications in the analysis of actively bent structures, this is deemed by far sufficient.

As second scenario, indicated as (II), the considerations on the magnitude of the applied force are investigated: In order to reach the same

#### 4 Interaction of deformation and structural behavior

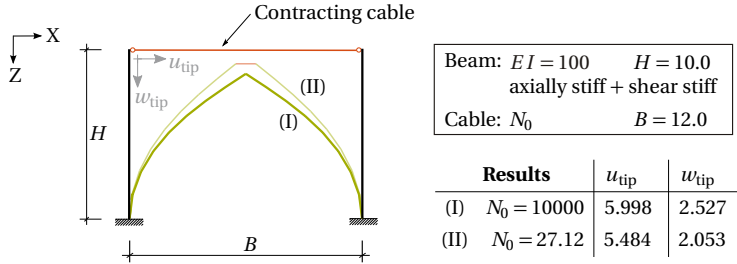


**Figure 4.24:** Two cantilevers connected by a contracting cable attached to their tips: Problem definition and deformed configurations for (I) closing the gap and (II) comparing to the problem from Figure 4.23.

tip-displacement in x-direction as for the force-loaded cantilever from Figure 4.23, *i.e.*  $u_{tip}^{force} = 5.469$ , the required prestress force in the contracting cable shall be determined: The reference displacement  $u_{tip}^{force}$  leaves a gap between the two tips. This gap corresponds to the current length  $\ell_{cable}$  of the cable which is in consequence

$$\ell_{cable} = L_{cable} - 2 \cdot u_{tip}^{force} = 12 - 10.938 = 1.062 . \quad (4.14)$$

Knowing that the external force corresponding to the reference deformation has been  $F_{ext} = 2.4$ , the corresponding PK2-prestress force can be determined as

$$N_0^{PK2} = \frac{L_{cable}}{\ell_{cable}} \cdot F_{ext} = \frac{12}{1.062} \cdot 2.4 = 27.12 \quad (4.15)$$

by inverting Equation (4.13). As indicated in Figure 4.24, the application of this prestress  $N_0^{PK2} = 27.12$  in the cable leads to a tip-displacement  $u_{tip} = 5.484$  which meets the reference solution quite well.

With these results it can be stated that the concept of contracting cables works accurately and robustly in order to pull two nodes towards each other, either to the same position or to a desired distance.

### Examples for shape control by contracting cables

Beyond the pure control of geometric distance, the concept of contracting cables can also be used to align resp. couple rotations. With the help of additional auxiliary lever arms, the forces exerted by contracting cables can act as moments as the following examples will demonstrate.

The first example is oriented along the pure bending of a cantilever which has been presented as a benchmark for the applied beam element in Figure 2.15 in Section 2.4.3. Now two of these cantilevers are bent to form a semi-circle with the help of two contracting cables as illustrated in Figure 4.25.

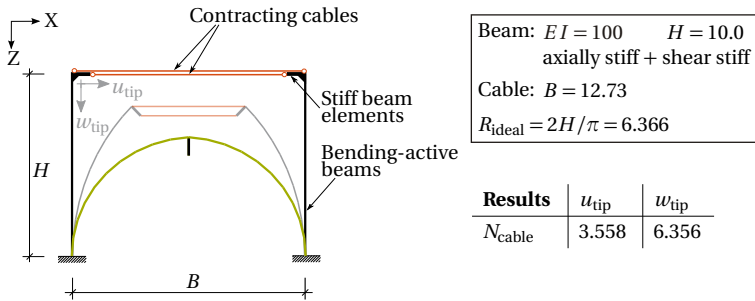


**Figure 4.25:** Bending of two cantilevers to a semi-circle with the help of contracting cables and auxiliary stiff beam elements

The two cantilevers are situated at a distance  $B = 2 \cdot R_{ideal} = 12.73$  which corresponds to the diameter of the ideal semi-circle. Two lever arms (indicated by the thicker lines in Figure 4.25) are attached to the tips of the cantilevers, modeled as "infinitely" stiff beams. Two contracting cables are applied: Cable 1 (sketched slightly above its actual position) links the tips of the cantilevers whereas cable 2 (sketched slightly below) is attached to the free ends of the stiff lever-arms. Figure 4.25 shows an intermediate configuration to clarify the different attachment points of the contracting cables.

The deformed configuration in Figure 4.25 is very close to the desired semi-circle. As the tip-displacements show, the position of the tip is accurate to 1% compared to the location on a perfect semi-circle.

As a second example, a prototypic bending-active bridge, depicted in Figure 4.26, is analyzed in order to illustrate the concept of *controlled buckling* mentioned in Section 4.2. Like in the selfstressed bowstring footbridge, see Figures 4.7 and 4.8, the upper bow of the bridge is lifted by a controlled buckling. Therefore the lower bending-active element is installed as two separated pieces which in total are shorter than the upper bow. These pieces are attached to the upper bow at the two outer nodes, assuring the transfer of the bending moment between the bows.

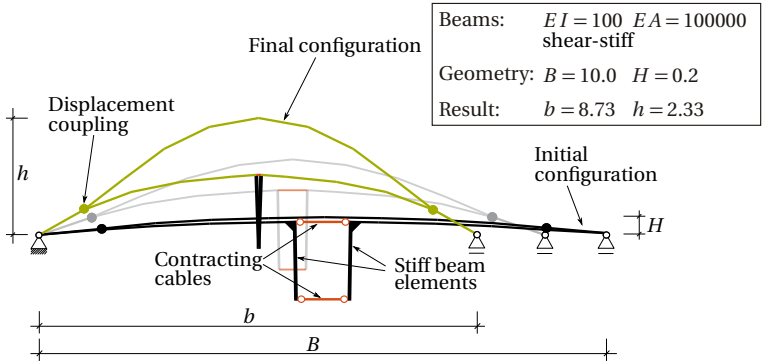


**Figure 4.26:** Prototypic self stressed bridge: Through the difference in length the upper bow "buckles" more, whereas the lower bow is closed using stiff beams and contracting cables

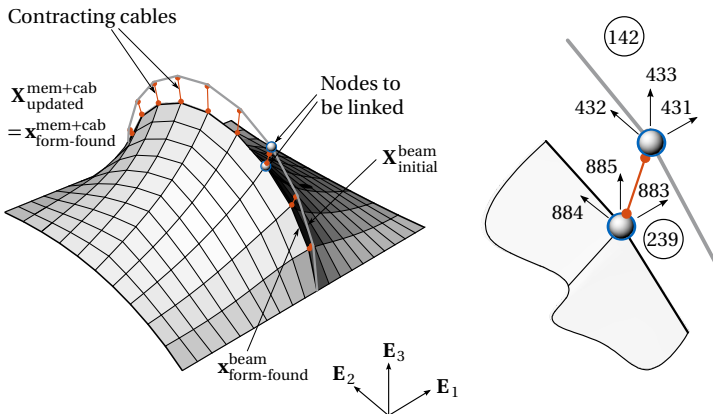
Additional stiff lever arms at the free end of the pieces are used to ensure the common rotation of the two ends. Two contracting cables are applied and force the juncture of the lower bow. This shortening of its chord forces the upper bow to lift. Since this lifting can be regarded as a forced bending due to a compressive normal force, it is called a *controlled buckling*. Note that an initial camber as illustrated in the starting configuration in Figure 4.26 is required to facilitate the initialization of the lifting process.

Figure 4.26 again shows an intermediate configuration (in lighter colors) and the final self stressed bridge. The gap in between the pieces of the lower bow and the free ends of the auxiliary lever arms is almost perfectly closed by contraction of the guiding cables.

### Contracting cables for initializing the restart after form-finding

Finally, the concept of contracting cables is used for the configuration update after the form-finding. To that end, the structure discussed in Section 4.4.1 is taken as an example. Instead of applying the initial displacements and multi-point constraints as illustrated in Figure 4.20, the doubled nodes are now coupled by contracting cables.

In Figure 4.27 these cables are illustrated. In the detailed view in Figure 4.27 (right) the DOF numbering shows that the coupling of the membrane nodes, here node 239, and the nodes on the beam, here node 142, is no longer realized by distributing the same DOFs, but by controlling the distance between the nodes with the help of a contracting cable.



**Figure 4.27:** Arch supported membrane from Figure 4.19 with contracting cables (orange) for the restart after form-finding

Although the introduction of the contracting cables is accompanied by mechanical challenges due to the high prestresses and the low stiffness, it can largely simplify the initialization and coupling procedure. In the present case, restarting with contracting cables instead of initial displacements has resulted in the identical deformation under the snow load  $p$  as depicted in Figure 4.21.

### Summary and conclusion of Chapter 4

Within this chapter, the interaction of deformation and structural behavior has been analyzed, focusing on lightweight structures. A review of realized examples has pointed out the potential of structures that actively make use of bending for their shape definition and the related challenges for their modeling and computation.

In order to analyze these structures, several aspects of their modeling and analysis have been discussed and compared:

- different methods for the construction stage analysis, focussed on their ability for the application in geometrically non-linear structures;
- configuration updates for multi-stage analyses like a structural analysis following the form-finding of a hybrid structure;
- contracting cables as an elegant and innovative technique to realize more complex mounting scenarios and explore *a priori* unknown equilibrium paths.

Together with accurate and robust non-linear element formulations, the findings of this chapter can be considered a basis for complex mounting analyses of structures like the ones presented. The discussed limitations of the different analysis and modeling techniques shall help to better estimate the reliability of implemented approaches when these are applied to geometrically non-linear structures and their mounting analysis.

## THE SAFETY VERIFICATION OF MEMBRANE STRUCTURES CONSIDERING THEIR NON-LINEAR BEHAVIOR

The verification of safety is one of the core requirements for the realization of structures. In that context Terwel [140, p. 17] states that

*"structural safety can be defined as the absence of unacceptable risk associated with failure of (part of) a structure".*

Whereas for structures with linear behavior prescriptions for the assessment of safety are provided for many materials within various standards, only few and limited guidelines exist for those structures exhibiting non-linear behavior due to large deformations.

Within this chapter, the safety verification of membrane structures considering their non-linear behavior is discussed. The current design practice w.r.t. non-linear structural behavior and the general context of the

Eurocodes will be presented. The focus of this chapter will then be on approaches for the safety verification of structural membranes.

**Remark:** In parts the content of this chapter has been published in Philipp et al. [119] and presented in my unpublished contributions to the German mirror group for CEN/TC 250/WG 5 for the preparation of a future *Eurocode for Membrane structures*, see Stranghöner et al. [136]. For the sake of easier readability these sources will not always be cited explicitly.

## 5.1 General design practice in civil engineering

To a large extent the current design practice for civil engineering structures relies on existing codes and standards. In the European building industry the *Eurocodes* provide standards for various types of structures and materials, e.g. steel, concrete and timber<sup>1</sup>. In the following, the basis of and principal approach to safety verification with the Eurocodes will be presented.

### 5.1.1 The semi-probabilistic method

As stated by the European Commission [58], for the Eurocodes (EC) "*the approach of structural reliability is based on the semi-probabilistic method (limit-state performance design and partial factors method)*". Hence the reliability analysis within the Eurocodes is placed between deterministic methods and full probabilistic methods<sup>2</sup>, see EC 0 (EN 1990) "Eurocode – Basis of structural design" [106].

The main concept behind the semi-probabilistic method is to define a probability of failure  $P_f$  that represents an acceptable level of safety<sup>3</sup> (see Figure 5.1(b)). This probability of failure can be linked to a reliability index  $\beta$ . To give an order of magnitude, for "usual" buildings (reliability class RC2) an annual failure probability in the order of  $10^{-6}$  is deemed acceptable [106]. All further verifications of specified limit states<sup>4</sup> in the different Eurocodes are designed in such a way that they assure this level of probability of

---

<sup>1</sup> In the basic Eurocode EC0 [106] a list of currently existing Eurocodes is provided.

<sup>2</sup> An exemplary application of a reliability approach to the assessment of membrane structures is presented by Gosling et al. [64].

<sup>3</sup> The applied definition of safety will be discussed in Section 5.1.2.

<sup>4</sup> The definition of these limit states leads to the term *limit state design*.

failure. Hence the probability of failure is used to determine resp. calibrate *partial factors* (often also called *factors of safety*). These are then applied and will implicitly assure the desired probability of failure. The implicit, indirect consideration of a probability of failure leads to the term "semi-probabilistic".

In the context of limit state design for structural membranes, two major limit states can be distinguished, the *serviceability limit state* (SLS) and the *ultimate limit state* (ULS). While the first (SLS) is focused on functioning, comfort and appearance, the second (ULS) concerns the safety of people and of the structure. Both verifications are based on the definition of relevant design situations and load cases [106].

### 5.1.2 The principal concept of the Eurocodes

In earlier design approaches, a *global safety factor concept* was used instead of the previously introduced semi-probabilistic method of the Eurocodes. This concept of global safety factors is illustrated in Figure 5.1(a): Assuming both the *effects of action*  $E$ <sup>5</sup> due to *actions*  $F$  and the resistance  $R$  being subject to statistical variations, the definition of mean values (e.g. the mean stress  $\mu_E$ ) and fractile values (e.g. the 95% fractile of the stress,  $E_{95\%}$ ) were used for verification. As described in Figure 5.1(a), this concept led to two values for the quantification of safety, the central factor of safety  $\gamma_0$  as difference between the two mean values  $\mu_E$  and  $\mu_R$ , and the nominal factor of safety  $\gamma_{\text{nom}}$  as difference between the respective fractiles, e.g.  $E_{95\%}$  and  $R_{5\%}$ .

The semi-probabilistic method still relies on distributed probabilities for loads and resistances: Fractile values are used to define the "characteristic" values for the actions and resistances,  $F_k$  and  $R_k$ , respectively.

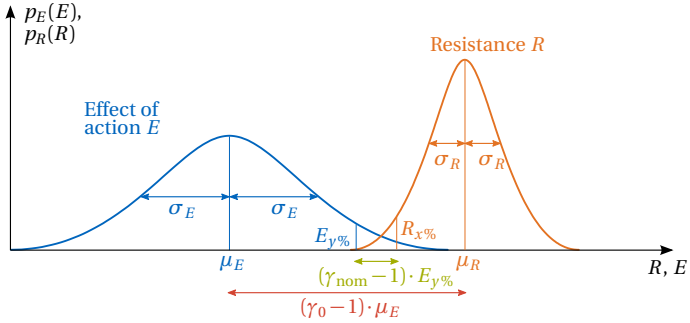
These characteristic values are directly used to verify the *serviceability limit state*: Applying characteristic material properties (e.g. Young's modulus  $E$  or Poisson's ratio  $\nu$ ) and characteristic (*i.e.* unfactored) loads, entities like the deflection under that load are computed and assessed against given limits.

The verification for the *ultimate limit state* is based on a comparison of a design value of an effect of action,  $E_d$ , and a design value of the correspond-

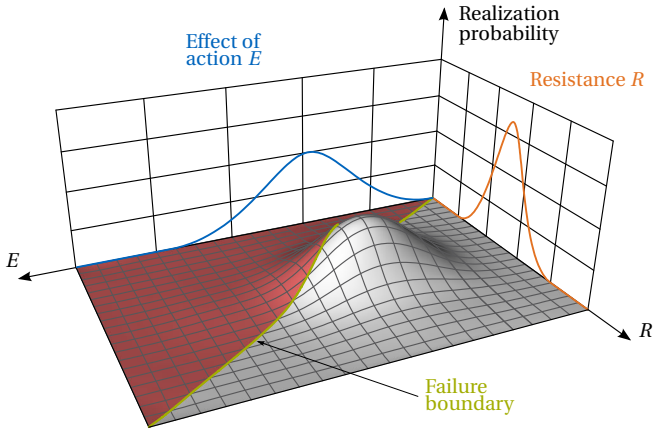
---

<sup>5</sup> As cited in [106] an effect of action  $E$  may act on individual structural members (e.g. stresses, strains, moments) or on the whole structure (e.g. deflections).

5 Safety verification of membrane structures



(a) Global safety factor concept: mean values  $\mu_E$  and  $\mu_R$ , standard deviations  $\sigma_E$  and  $\sigma_R$ , corresponding probabilities of realization  $p_R(R)$  and  $p_E(E)$ , and defined factors of safety  $\gamma_{nom}$  and  $\gamma_0$



(b) Failure probability  $P_f$  (volume under the red surface) as a function of the variations of effects of actions  $E$  and resistance  $R$ , and failure boundary (green) delimiting the failure domain

**Figure 5.1:** Concepts of safety: global safety factor concept and failure probabilities (schematic sketches)

ing resistance,  $R_d$ . This basic verification concept is usually expressed as

$$E_d = E_d\{G \oplus Q\} \leq R_d = \frac{R_k}{\gamma_M}, \quad (5.1)$$

where  $R_d$  is defined through the characteristic resistance  $R_k$  and the partial factor  $\gamma_M$ . This partial factor  $\gamma_M \geq 1.0$  reflects the uncertainties in the definition of the material properties. The better material properties can be predicted, the smaller  $\gamma_M$  can be assumed. As an example, the partial safety factors for steel and timber are defined as  $\gamma_{M,steel} \approx 1.0$  to  $1.1$  resp.  $\gamma_{M,timber} \approx 1.3$ , reflecting the larger variation of material properties in timber.

The design value of the effect of action,  $E_d$ , is the outcome of a load combination of permanent and variable actions  $G$  and  $Q$ , respectively. These actions are collected in load combinations (indicated by the combinatorial sign " $\oplus$ " in Equation (5.1)) that reflect relevant scenarios the structure might be faced with during its projected lifetime. In addition, partial factors  $\gamma_F$  are applied to the respective loads in order to account for the uncertainties in the load values. As an example the classical partial factors for self weight and variable actions are  $\gamma_G = 1.35$  and  $\gamma_Q = 1.5$ , respectively, again reflecting the larger variation of the latter. Combination factors  $\psi$  represent the probability of occurrence in the respective load combinations, *e.g.* a combination of self weight of the structure, wind and traffic load. In the Eurocodes for the respective materials, detailed instructions for the detailing and design of structures are provided, as well as specific values for the various partial factors.

## 5.2 Non-linear behavior and verification approaches

As has already been discussed, architectural membranes and other prestressed tensile structures draw their load-bearing capacities out of their shape – generally doubly curved – and their ability to undergo large deformations. In order to reliably simulate these large deformations, the need for a geometrically non-linear analysis is obvious. However this need for non-linear analysis has important consequences on possible verification approaches. In the following, these consequences on load combinations as well as on the determination and proceeding of design values  $E_d$  of effects of actions will be discussed.

### 5.2.1 Linear behavior and related simplifications

As presented in Section 5.1.2, a core ingredient to the philosophy of the Eurocodes is the concept of load combinations. Regarding the analysis of geometrically non-linear structures it is important to state that without linear behavior of the structure, the widely used superposition approach is not applicable any longer, see also Section 4.2.2. At a first glance, this may be considered a minor inconvenience, however the consequences to the computational effort are much more severe: A major simplification made in the Eurocodes is to state that for the determination of the effects of actions a factoring of the action  $F$  is – at least in most cases – equivalent to factoring the effects  $E$  of this action, as expressed in Equation (6.2) of the EC0 [106]:

$$E_d = \gamma_{Sd} \cdot E\{\gamma_{f,i} \cdot F_{rep,i}; a_d\} \xrightarrow[\text{behavior}]{\text{linear structural}} E_d = E\{\gamma_{Sd} \cdot \gamma_{f,i} \cdot F_{rep,i}; a_d\} \quad (5.2)$$

Here  $i$  is the summation index for different loading actions,  $E_d$  is the design value of the effect of action due to the load case which is composed of actions  $F_{rep}$  applied to the design geometry  $a_d$ .  $F_{rep}$  is the representative value of the action that is multiplied by the partial factor  $\gamma_f$  which accounts for possible unfavorable deviations from the representative value<sup>6</sup>. At the left hand side of Equation (5.2), the resulting effect of action  $E$  is factored by a partial factor  $\gamma_{Sd}$  for the uncertainties in modeling. At the right hand side the underlying actions  $F$  are factored by  $\gamma_{Sd}$  which is commonly summarized in one single partial factor

$$\gamma_F = \gamma_{Sd} \cdot \gamma_f. \quad (5.3)$$

To give a prototypic example, the design value  $E_d$  of a combination of self weight  $G$  and two variable actions  $Q_1$  and  $Q_2$ ,

$$E_d\{G \oplus Q_1 \oplus Q_2\} = f(G, Q_1, Q_2, \gamma_G, \gamma_{Q1}, \gamma_{Q2}), \quad (5.4)$$

with their respective weighting factors  $\gamma_G$  and  $\gamma_{Q\alpha}$  can then – with the assumption of linear structural behavior, *i.e.* a linear relation between action  $F$  and effect of action  $E$  – be broken down to

$$E_d\{G \oplus Q_1 \oplus Q_2\} = \gamma_G f(G) + \gamma_{Q1} f(Q_1) + \gamma_{Q2} f(Q_2). \quad (5.5)$$

<sup>6</sup> Note: For alignment with the commonly used terms, in the sequel no distinction will be made between the characteristic value  $F_k$  and the representative value of the action,  $F_{rep}$ ; only one single action  $F$  will be used.

Even for a large number of combinations, as usually required by current verification standards, each relation  $f(F)$  only needs to be evaluated once. The required combinations are then superposed from these evaluations in the postprocessing.

### 5.2.2 Review of verification concepts for geometric non-linearity

Before focusing on structural membranes it seems of interest to review general prescriptions and applied verification concepts for geometric non-linearity. This provides a basis for the discussion of structural membranes as well as a possible comparison for the elaborated approaches.

#### Classification of non-linearity in Eurocode 0

Setting the principal frame for all material-specific Eurocodes, Eurocode 0 [36, 106] addresses the issue of non-linear structural behavior by indicating a distinction between two different types of non-linear behavior:

*"For non-linear analysis (i.e. when the relationship between actions and their effects is not linear), the following simplified rules may be considered in the case of a single predominant action:*

- a) When the action effect increases more than the action, the partial factor  $\gamma_F$  should be applied to the representative value of the action.*
- b) When the action effect increases less than the action, the partial factor  $\gamma_F$  should be applied to the action effect of the representative value of the action.*

*NOTE Except for rope, cable and membrane structures, most structures or structural elements are in category a)."*

[36, §6.3.2(4)]

Hence a distinction is made between structures where the effect of action  $E$  increases more than the representative value of the action  $F_{\text{rep}}$  (category

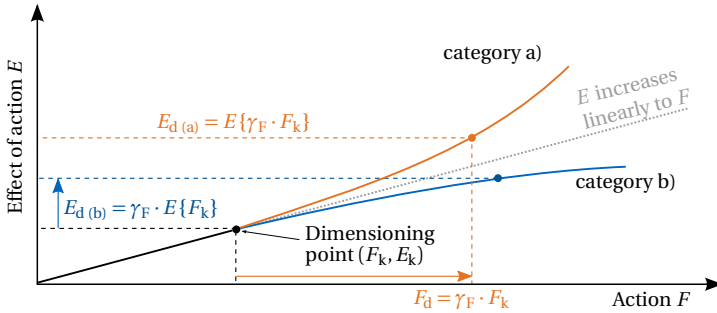


**Figure 5.2:** Schematic representation of the two types of non-linear behavior of structures proposed in the EC 0 [106]

a) respectively less (category b). The behavior characterized by category a) often is termed *over-linear* while category b) describes *under-linear* behavior, see also Stranghöner et al. [136] and Uhlemann et al. [144].

The simplified representation in Figure 5.2 illustrates the difference between the two types of behavior. As mentioned above, for the case of a linear behavior of the structure (indicated by the gray dotted line), the two cases coincide and thus the simplification from Equation (5.2) can be applied.

In case of non-linear structural behavior, it is important to correctly classify the type of structure to one of the above categories. However, the prescriptions w.r.t. tensile structures given in EC 0 (see citation above) are quite vague. A reliable and unique classification of a structure can be problematic, since the direct output of a non-linear simulation based on non-factorized characteristic actions  $F_k$  is only the dimensioning point  $(F_k, E_k)$ , not a complete graph as shown in Figure 5.2. In a more abstract sense, this classification of the non-linear behavior requires the determination of the slope resp. of the curvature of the  $F$ - $E$ -graph. Two related approaches will be discussed in Section 5.3.2.

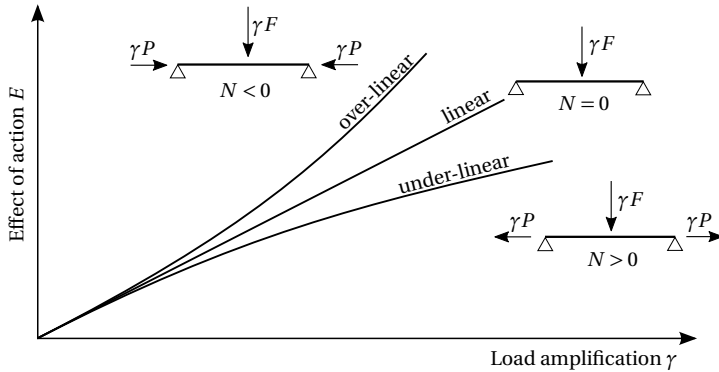


**Figure 5.3:** Classical notion of non-linear relation of effects of action  $E$  and load amplification  $\gamma$  in static analysis

### Geometrical non-linearity with Theory of Second Order

The notion of non-linear behavior as sketched in Figure 5.3 and as specified in Eurocode 0 is mainly based in the non-linear analysis of elements with bending rigidity: For slender structural elements, the consideration of geometrically non-linear effects is deemed necessary.

For steel, concrete or timber structures the common approach to geometric non-linearity is an analysis following Theory of Second Order (abbr. Th.II.O.; also referred to as *second-order analysis*), see e.g. Eurocode 3 "Design of steel structures – Part 1-1: General rules and rules for buildings" [104]. For a brief introduction to an analysis according to Th.II.O., refer to Section 2.4.

Depending on the external longitudinal force  $P$  in Figure 5.3, different effects of the resultant normal force  $N$  on the displayed member can be observed: While in the case of tension, *i.e.* a normal force  $N > 0$ , the deformation and with it the bending stresses are reduced, in case of compression, *i.e.*  $N < 0$ , an increase of the effects of action is observed. Consequently in most standards, an analysis according to Th.II.O. is compulsory for members in compression since it is a matter of safety, whereas for members in tension it may be used for a more economic design.

Besides specific, often problem-dependent simplified approaches, where individual stability checks of equivalent members resp. tabulated amplification factors are applied, for non-linear analyses according to Th.II.O. the basic approach can be summarized as follows:

- Load combinations according to Equation (5.4) are assembled including the application of partial factors  $\gamma_F$ ,
- the effects of action (here stresses  $\sigma_{Ed}$ ) under this load ensemble are derived applying the non-linear strain measure and (iteratively) establishing equilibrium in the deformed configuration assuming unfavorable imperfections,
- these stresses  $\sigma_{Ed}$  are assessed against design limit stresses  $\sigma_u/\gamma_{M0}$ .

Hence the prescriptions from Eurocode 0 cited in the previous section are implicitly fulfilled: By factoring the actions  $F$  the over-linear behavior assumed for slender members in compression is taken into account.

### Verification of cable structures

In their load-bearing behavior cable structures as prestressed tensile structures are "close relatives" to structural membranes. However, in contrast to the latter, for cable structures established standards and verification guidelines exist. In the present context the implemented standard is Eurocode 3 "Design of steel structures – Part 1-11: Design of structures with tension components" [35, 105] (EN 1993-1-11), which gives guidance for the verification approach considering non-linear behavior and prestress.

Dealing with prestressed structures reveals the question of how to treat prestress (see also Section 5.4.1): Is it to be considered an action, and consequently increased through a partial factor, or rather a resistance? EN 1993-1-11 gives the prescription that *"permanent actions, which should consist of actions from gravity loads "G" and prestress "P" should be considered as a single permanent action "G+P" to which the relevant partial factors  $\gamma_{Gi}$  should be applied"* [35, §2.2(2)], which in consequence results in increasing the prestress for the verification in ULS, see also Kathage et al. [78].

Kathage et al. [78] and Schmidt et al. [130] state that for cable structures the ultimate limit state (ULS) and the serviceability limit state (SLS) are

much closer related than for most other structures. In fact, often the SLS is dominating and solely determining the design verification for prestressed cable net structures or, as phrased in EN 1993-1-11, "*serviceability checks may govern over ULS-verifications*" [35, §2.2(1)].

As stated in EN 1993-1-11, SLS prescriptions may be used to assure that stresses remain in the elastic range, *i.e.* below an ultimate elastic stress  $\sigma_u$ . As a lower bound tensile forces in all members have to be assured in all states<sup>7</sup> (cf. the cable net example in Section 5.3.2). These "indirect" ULS verifications become possible due to the generally under-linear structural response to actions.

However, based on stochastic investigations of a spoke-wheel cable roof, Schmidt et al. [130] formulate criticism of the verification prescriptions from EN 1993-1-11: Following SLS-prescriptions the verification condition from EN 1993-1-11 can be reformulated to

$$\sigma_{Ek} \leq \frac{\sigma_{uk}}{1.5 \cdot \gamma_R \cdot \gamma_F} \quad (5.6)$$

where  $\sigma_{uk}$  is the characteristic ultimate stress of the cable material and  $\gamma_R$  and  $\gamma_F$  are the partial factors for the resistance and the action, respectively (see also [78]). The stresses  $\sigma_{Ek}$  result from the same loading scenarios as in ULS, but applying characteristic, *i.e.* unfactored loads. Equation (5.6) implicitly fulfills the condition of Eurocode 0 [106] for structures with under-linear behavior: the partial factor is "*applied to the action effect of the representative value of the action*" [106, §6.3.2(4)].

This fixation of the safe-sided simplification from the basic Eurocode 0 including the prescription of fixed amplification factors for the verification of cable net structures in the EN 1993-1-11 is criticized by Schmidt et al. [130]: Through its conservative approach, economic design making use of the "*strongly under-linear relation between action and actually resulting stress resultants*" [130, p.724, transl.] is no longer possible and consequently the prescriptions from EN 1993-1-11 are considered pessimistic and not well suited.

---

<sup>7</sup> This condition certainly is of even more importance than it is the case for preventing wrinkling of membrane structures which can still be stabilized through tensile stresses in the second direction, see also Sections 2.5.1 and 3.5.1.

### 5.3 Membrane structures and the Eurocode framework

As mentioned above, in Europe the design of structures generally is codified in the *Structural Eurocodes* (EC) which exist for the most widely applied materials like steel, concrete or timber. However, such a unified standard does not yet exist for membrane structures. Based on first attempts towards a unified design and verification approach (like the *TensiNet Design Guide* by Forster et al. [60]), CEN/TC250/WG5<sup>8</sup> has initiated the development of a new Eurocode. This code intends to provide guidance for the very particular design and simulation demands of structural membranes.

#### 5.3.1 Review of verification guidelines for membrane structures

In contrast to most other materials used in the building and construction industry, currently in Europe there is no unified standard for the verification of architectural membranes. Some standards and design guides exist on national level, like the ITBTP<sup>9</sup> recommendations [12] (France) or the German practice, combining the DIN 4134 [103] and the dissertation by Minte [99]. Most of these standards and guidelines (and also the ASCE<sup>10</sup> 55-10 [5] (USA)) are based on a stress factor approach that compares the results of an analysis with characteristic loads (*i.e.* unfactored, representative actions) to a permissible strength, corresponding to the global safety factor concept presented in Section 5.1.2.

As an example, one may take the approach from the ITBTP guide [12],

$$T_C \leq T_D = \frac{k_q \cdot k_e}{\gamma_t} \cdot T_{rm} = \frac{T_{rm}}{\gamma_{stress}}, \quad (5.7)$$

where the design strength  $T_D$  is derived from the (characteristic) tensile strength  $T_{rm}$ , reduced by the factors  $k_q$  and  $k_e$  (with  $\{k_q, k_e\} < 1$ ), as well as the so-called safety coefficient  $\gamma_t$ , also taking into account the environmental degradation. The design strength  $T_D$  represents the permissible strength that is ultimately assessed against the calculated tensile force  $T_C$

<sup>8</sup> CEN .. European committee for standardization; TC250 .. Technical Committee "Structural Eurocodes"; WG5 .. Working Group 5 for Membrane Structures

<sup>9</sup> Institut technique du bâtiment et des travaux publics, France

<sup>10</sup> American Society of Civil Engineers, USA

under the respective load combination, assuming characteristic values for the actions. The quality factor  $k_q$  adjusts the member capacity to the execution quality and the quality of the fabric itself; the scaling factor  $k_e$  reflects the increased risk of critical defect with increasing surface area. For the sake of comparison, the individual factors –  $k_q$ ,  $k_e$  and  $\gamma_t$  – may be summarized in one stress reduction coefficient  $\gamma_{\text{stress}}$  (often termed "stress factor"), as demonstrated in Equation (5.7).

Although the various standards and guidelines show differences in their respective prescribed load combinations and the way in which the stress reductions are applied, they can basically be compared to the procedure described in Equation (5.7), summarizing the respective factors and coefficients to the overall stress factor  $\gamma_{\text{stress}}$ . As stated *e.g.* by Forster et al. [60] and Gosling et al. [64], the mentioned guidelines agree on comparable "levels of uncertainty", reflected in the respective stress factors  $\gamma_{\text{stress}}$  as they are schematically represented in Table 5.1.

**Table 5.1:** Comparison of the respective stress factors  $\gamma_{\text{stress}}$  in selected verification approaches.

Standard	Factors	Incorporated influences	$\gamma_{\text{stress}}$
ASCE 55-10 [5]	$L_t, \beta$	life cycle factor, strength reduction; based on different load combinations	4.0 to 7.8
ITBTP Design Guide [12]	$k_q, k_e, \gamma_t$	execution quality, scale factor, environmental degradation	(4.0)5.0 to 7.0
German practice, based on DIN 4134 [103] and Minte [99]	$A_{\text{res}}$ ( $\gamma_t, \gamma_M, A_i$ )	loading uncertainties, material safety, test scaling, influence of time, environmental degradation, temperature	2.9 to 6.4

In summary one may conclude that permissible stresses are obtained by reducing the characteristic strength of the textile by a reduction factor  $\gamma_{\text{stress}}$  in the order of 4.0 to 7.0 (the extreme values of 2.9 and 7.8 from Table 5.1 are rather rare cases). This already provides a basis for a common European approach. However the underlying global safety factor concept is not in line with the contemporary semi-probabilistic method at the basis of the Eurocodes, see Section 5.1.2. Moreover, the inclusion of safety margins as well as other effects in one single factor  $\gamma_{\text{stress}}$  as displayed

prototypically in Equation (5.7) renders the identification of the existing "structural reserves" in a membrane structure virtually impossible.

Throughout all reviewed guidelines, the analysis and verification of different load scenarios is required. This definition of scenarios does not release the designing engineer from his responsibility to keep in mind the whole structure and the situations it might face in the future, see also Bown et al. [30]. However, as also cited in Forster et al. [60] and Stranghöner et al. [136], several scenarios are generally to be considered:

- assessment of strength of stressed fabrics, cables and other members;
- assessment of deformation in order to avoid contact of the tensile components with the surrounding structure as well as excessive deformation in general;
- ensuring a fully taut state in order to avoid dynamic flutter of the membrane and to avoid wrinkles;
- avoidance of progressive collapse due to failure of any component;
- avoidance of ponding, *i.e.* ensuring positive drainage from all areas and under all conditions.

Since these scenarios are more or less unanimously accepted, they will not be further discussed within this thesis.

### 5.3.2 Classification of the non-linear behavior of tensile structures

As cited in Section 5.2.2, EC0 [106] provides a classification into two types of non-linear behavior. Following the prescriptions in Section 6.3.2 of the EC0, cable and membrane structures are to be classified as structures with under-linear behavior (see Figure 5.2), or – expressed in the words of the EC0 – as structures for which "*..* the action effect increases less than the action *..*" [106, §6.3.2(4)].

#### Reduced cable net as an analytical example

In order to underline this assumption and demonstrate some effects of non-linearity, a reduced model of a classical hyper as illustrated in Figure 5.4 will be discussed as a prototype. The simplifications made from the hyper

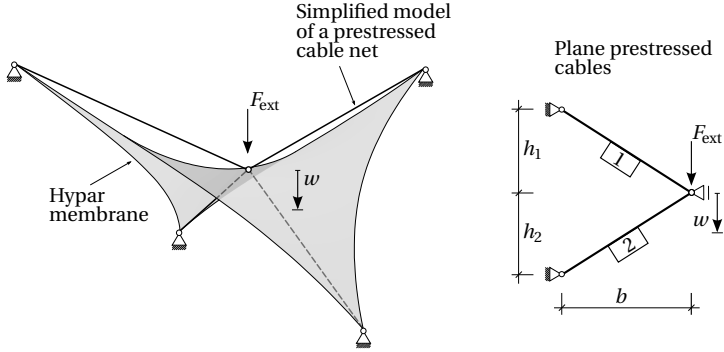


**Figure 5.4:** Reduction of a hypar membrane to a simplified cable net: At first the hypar membrane is reduced to a net of four cables (left). Applying symmetry conditions and rotating into a plane allows analyzing the system as a plane two-cable structure (right).

membrane to the model of two prestressed truss members (single DOF system) allow keeping the derivations intelligible, however conclusions to the principal behavior of the membrane can be drawn.

For the analysis of the non-linear behavior of this prototype structure, its residual force expression  $\mathbf{R} = \mathbf{R}_{\text{int}} + \mathbf{R}_{\text{ext}}$  is derived as a function of the displacement variables  $\mathbf{u}$  according to the derivations in Sections 2.3.4 and 4.3.2. In the present single DOF system the residual force vector  $\mathbf{R}$  reduces to a scalar  $R$ . In case of conservative loading, the external residual force  $R_{\text{ext}}$  is equal to the load  $F_{\text{ext}}$ , see Figure 5.4, representing *e.g.* a snow load. The internal virtual work of a single member  $i$  can be written as

$$\delta W_{\text{int},i} = \int_{V_0} \left[ (S_{11} + S_0) \cdot \delta \epsilon_{\text{GL}} \right] dV = A_i L_i \left[ (S_{11,i} + S_{0,i}) \cdot \delta \epsilon_{\text{GL},i} \right], \quad (5.8)$$

where  $L_i$  and  $A_i$  are the length and cross section of the member  $i$ , respectively. In the members constant strains (measured as Green-Lagrange strains<sup>11</sup>) and stresses (2<sup>nd</sup> Piola-Kirchhoff stresses from elastic deforma-

<sup>11</sup> Note that for the sake of easier readability in the present context the Green-Lagrange strains are indicated as  $\epsilon_{\text{GL}}$  in contrast to the nomenclature in Chapter 2.

tion,  $S_{11}$  and prestress  $S_0$ ) along the elements are assumed. In Equation (5.8) the integration over the volume has been replaced by the pre-integrated member contributions, making use of the constant strains and stresses in each member.

For truss members, the strains  $\epsilon_{GL}$  can be expressed as a function of the reference length  $L_i$  and the current length  $\ell_i$ :

$$\epsilon_{GL,i} = \frac{1}{2} \frac{\ell_i^2 - L_i^2}{L_i^2}, \quad (5.9)$$

and consequently for the individual members in Figure 5.4:

$$\epsilon_{GL,1} = \frac{1}{2} \frac{w^2 + 2h_1 w}{L_1^2} \quad \text{resp.} \quad \epsilon_{GL,2} = \frac{1}{2} \frac{w^2 - 2h_2 w}{L_2^2} \quad (5.10)$$

Introducing the simplifying assumptions of equal height  $h_i = h$ , initial length  $L_i = L$ , cross section  $A_i = A$ , and prestress  $S_{0,i} = S_0$  for the two members, the expression of the internal residual force  $R_{\text{int}} = \Sigma R_{\text{int},i}$  can be formulated as derived in Equation (2.56) as

$$\begin{aligned} R_{\text{int}} &= \frac{A}{L^3} (w + h) \left( \frac{E}{2} (w^2 + 2hw) + S_0 L^2 \right) \\ &+ \frac{A}{L^3} (w - h) \left( \frac{E}{2} (w^2 - 2hw) + S_0 L^2 \right) \\ &= \frac{EA}{L^3} (w^3 + 2h^2 w) + 2 \frac{w}{L} S_0 A. \end{aligned} \quad (5.11)$$

Additionally assuming linear elastic material (St. Venant-Kirchhoff material law, see Equation (2.41)), here the elastic stresses  $S_{11}$  have been replaced by  $S_{11} = E \epsilon_{GL}$ , introducing Young's modulus  $E$ .

For the evaluation of internal forces as effects of actions, the internal forces  $N_1$  and  $N_2$  of the respective members can be written as

$$N_i = \frac{\ell_i}{L_i} A_i S_i = \frac{\ell_i}{L_i} A_i (E \epsilon_{GL,i} + S_{0,i}) = \frac{\ell_i}{L_i} \left( \frac{EA}{2} \frac{\ell_i^2 - L_i^2}{L_i^2} + S_0 A \right), \quad (5.12)$$

where the current length  $\ell_i$  is a function of the unknown vertical displacement  $w$ . The factor  $\ell_i/L_i$  yields a physically meaningful force from the

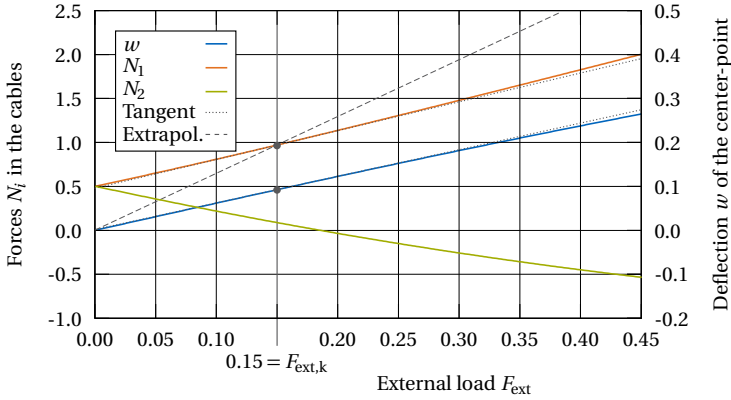


**Figure 5.5:** Effects of actions  $E$  for the cable net example and linear extrapolations w.r.t. dimensioning point  $F_{ext,k}$

PK2 stresses in the member. Note that in all presented developments, a deformation of the cross-section  $A$  is neglected (corresponding to Poisson's ratio  $\nu = 0$ ).

With these formulations at hand, selected effects of action  $E$  are analyzed regarding their possible verification according to the approach of Eurocode 0: (i) the displacement  $w$  and (ii) the normal forces  $N_1$  and  $N_2$  in the upper resp. lower cable, see Figure 5.4. Figure 5.5 shows the progression of these parameters under an increasing load  $F_{ext}$ .

At a first glance the deformation  $w$  seems to increase linearly with increasing  $F_{ext}$ . Fixing an arbitrarily chosen dimensioning point through a characteristic load  $F_{ext,k}$ , here  $F_{ext,k} = 0.15$ , allows introducing a linear extrapolation (indicated by the thin dotted lines in Figure 5.5), from which the slightly non-linear curve of  $w$  w.r.t.  $F_{ext}$  can be observed. As expected and in line with the prescriptions of EC0 for cable nets, under-linear behavior can be observed.

For the member forces  $N_i$  the global tendency can also be observed as expected:  $N_1$  (corresponding to the "tension cord") increases, whereas  $N_2$ , the force corresponding to the "compression arch", decreases under increasing load. For the ULS-verification of stresses resp. forces against

5 Safety verification of membrane structures

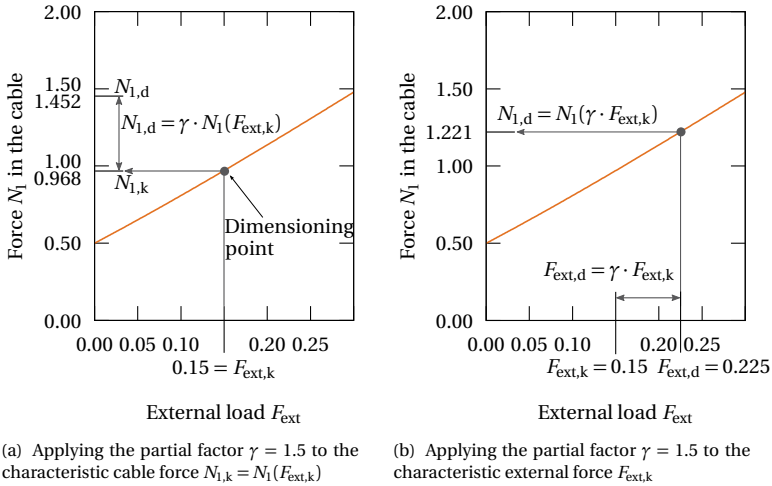


**Figure 5.6:** Application of the partial factor  $\gamma$  to the effect of action  $E$  resp. the action  $F$ , and resulting design values  $N_{1,d}$

material resistance  $R$  as stated in Equation (5.1) only the increasing force  $N_1$  is of interest. Taking again the characteristic load  $F_{ext,k}$  as evaluation point,  $N_1$  behaves under-linearly compared to the linear extrapolation (dashed line in Figure 5.5). However this under-linear behavior is mainly, if not exclusively, related to the "offset" of  $N_1$  due to the prestress force  $N_{1,0} = S_0 A$ . When compared to its tangent (dotted line in Figure 5.5), it can be seen that the graph of  $N_1$  is convex. Hence the general classification of cable net structures as under-linear is to be treated with care, since in large parts it depends on the magnitude of the prestress and the extrapolation range.

In that sense a comparison to the classical notions of non-linearity as illustrated in Figure 5.3 is difficult: In the classical definition, all loads are affected by one load amplification factor  $\gamma$ , unlike in the present case, where just the load  $F_{ext}$  is multiplied, whereas the prestress as a structural property stays constant.

To illustrate the two different approaches of determining the design value of  $N_1$ , the resulting design values  $N_{1,d}$  are displayed in Figure 5.6. It can be

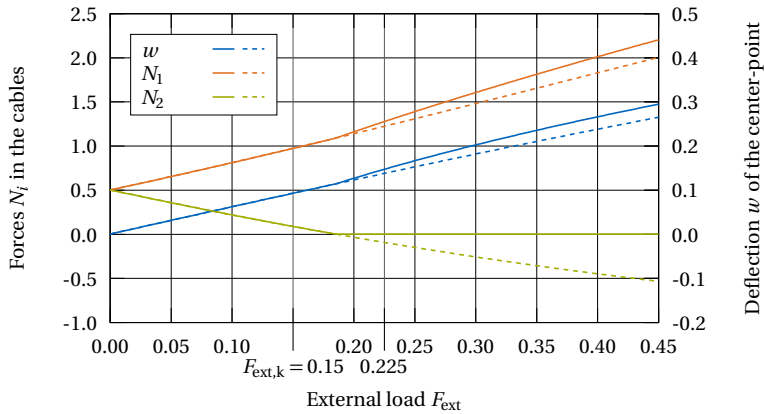


**Figure 5.7:** Effects of actions  $E$  for the cable net example under consideration of cable 2 going slack. The dashed lines represent the case where cable 2 still contributes in compression.

seen that by either factoring the action  $F$  or the effect of action  $E$ , they differ considerably.

For  $N_2$ , the force in the "compression arch", the elastic stresses absorb the prestress. Here, another relevant effect can be noticed: For an external force of  $F_{ext} \approx 0.18$  the prestress in member 2 is absorbed and the cable will go slack. Consequently, it will no longer contribute to the load-bearing of the structure, *i.e.* the system changes and the entire load has to be carried by member 1. As illustrated in Figure 5.7, where now the failure of cable 2 is considered, the increase of  $N_1$  accelerates, indicated by the kink in the graph. The same effect can be observed for the displacement  $w$ . The comparison with the dashed graphs, which indicate the respective trend without considering cable 2 going slack, shows that this effect certainly is not negligible. However, it cannot be taken into account by factoring the effect of action  $E$  directly, see Figure 5.6(a).

The fundamental change of the structural system introduces a new source of non-linearity in the system. This so-called *system non-linearity* is accompanied by a sudden change in the stiffness (see also Section 4.2.1 on construction stage analysis). Obviously for prestressed cable net structures

as well as for structural membranes the case of members going slack is to be avoided. However in the discussion on how to classify the non-linear behavior of structures and – on the long end – how to apply partial factors, effects affecting the overall structure have to be taken into account. Just like the prevention of exceeding a defined stress level, the prevention of these effects needs to be assured with a certain probability.

Following the prescriptions of Eurocode 0 [106], the ULS verification of  $N_1$  is placed in category b) and the assessment follows the procedure illustrated in Figure 5.6(a): stresses are determined based on characteristic loads  $F_k$ , factored by a partial safety factor  $\gamma$  and then these stresses are assessed against admissible stresses.

From this very simplistic and reduced example, one can already conclude that the current design practice – *i.e.* application of safety factors on the effects of action  $E$  rather than on the action  $F$  itself – complies with the basic instructions for non-linear structures of the Eurocode 0. However, occurring *system non-linearity* by members going slack, see Figure 5.7, cannot be tracked with this approach. The following real-life example of a four-point sail investigates the principle behavior for a full-scale example.

### Evaluation of stresses for a four-point sail

For the evaluation of stresses, the full-scale example of a simple hyper with an extension of 6 by 6 m and 4 m height is taken. The form-finding is performed with isotropic prestress in the membrane and a prestress ratio of  $n_{0, \text{membrane}}/N_{0, \text{cable}} = 1/10$ , yielding the shape that is displayed in Figure 5.8. The structure is loaded by a snow-load  $s$ . The magnitude of  $s$  is increased from 0 to  $0.48 \text{ kN/m}^2$ . Besides all material and cross-sectional data for the static analysis, Figure 5.8 indicates the evaluation points where the stresses are measured. These are distributed along the two principal load-bearing directions, the *tension cord*, spanning from high-point to high-point, and the *compression arch* perpendicular to it.

As stresses, the principal stresses  $\sigma_I$  and  $\sigma_{II}$  are considered, representing the extremal stresses at each point of the structure. Investigations of the stresses plotted in Figure 5.9 show that the highest stresses occur in the tension cord close to the high-point (point 806 in Figure 5.8) whereas the most severe loss of prestress occurs in the compression arch close to the center (point 396 in Figure 5.8). These two points are selected for further

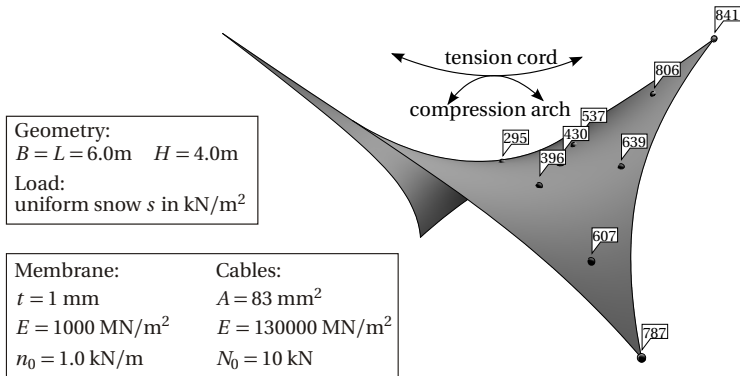


**Figure 5.8:** Four-point sail with model parameters, principal load-bearing directions and indication of evaluation points

verification of the stresses, assuming a dimensioning load (characteristic load) of  $s_k = 0.24\text{ kN/m}^2$ .

Analyzing the first principal stress  $\sigma_1$  in the tension cord (point 806), a convex load-stress curve can be observed. However, in comparison with a linear interpolation which is depicted as the gray dotted line in Figure 5.10, the shifted starting point of the linear evaluation (due to prestress) suggests an under-linear progression of the stress. Following the instructions from Eurocode 0, an exemplary application of a partial factor  $\gamma_F$  on the principal stress as an effect of action is shown in Figure 5.10 (in green).

As intended by the categorization from Eurocode 0 and recently reworked in Stranghöner et al. [136] and Uhlemann et al. [144], the factoring of the effect of action is on the "safe side", *i.e.* the linear extrapolation yields higher design stresses than an equivalent increase of the load would do. However Figure 5.10 also shows that the extrapolated design stress is only slightly larger than it would have been for an increased load (orange). If the partial factor  $\gamma$  was 1.75 or even higher, factoring the stresses under the characteristic load would not be conservative anymore.

This effect – just like it has been the case for the example of the reduced cable net – becomes even more accentuated when the second principal stresses  $\sigma_{II}$  in the compression arch (point 396 in Figure 5.8) are considered.

5 Safety verification of membrane structures

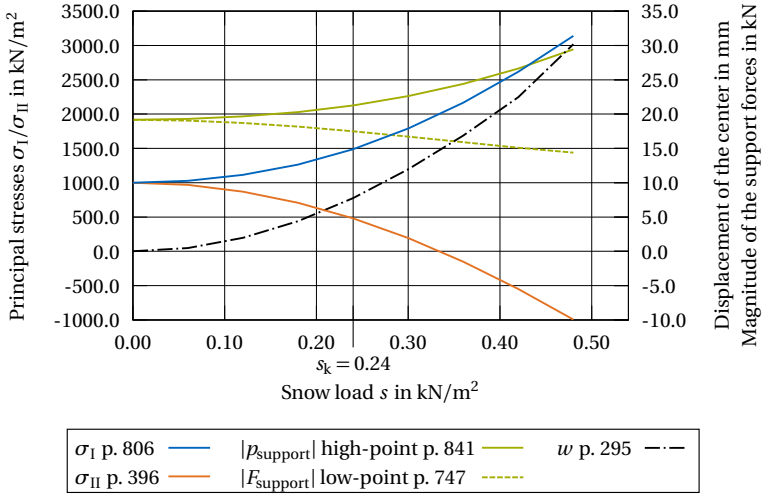


**Figure 5.9:** Selected principal stresses, displacement at the center and support forces with increasing snow load  $s$

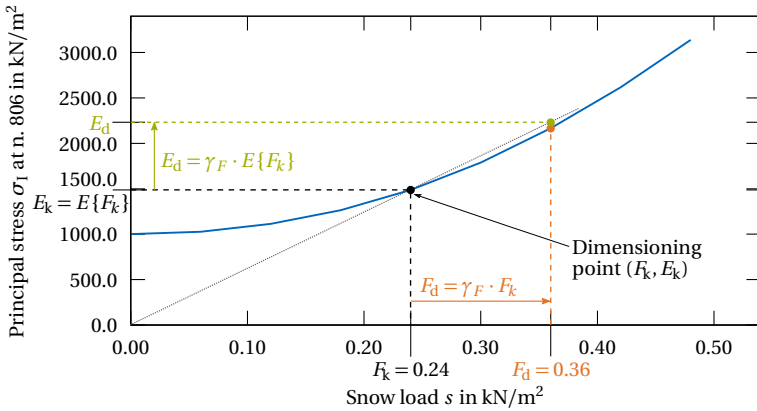


**Figure 5.10:** Maximum principal stresses in the tension cord and possible design values according to Eurocode 0

Under a load of  $s \approx 0.33$ , corresponding to a load factor of  $\gamma_F \approx 1.375$ , the compression arch is not fully taut anymore since  $\sigma_{II}$  drops below 0. These negative stresses in general are to be avoided in order to prevent wrinkles and the accompanying change of the structural system, see e.g. Stranghöner et al. [136], as already discussed for the cable net example above.

### **Conclusions from the reduced cable-net and the four-point sail**

From these two examples, several conclusions can be drawn with regard to a future standardization of the verification of structural membranes: In general it can be stated that the current design practice of factoring the stresses and other effects of action computed under a characteristic load resp. load scenario is in line with the general prescriptions of the Eurocode 0 [106] and its classification in under- and over-linear structural behavior. However – depending on the load factor  $\gamma_F$  to be applied – this classification and the resulting prescriptions for factoring might only be applicable in a narrow range of the load intensity.

Consequently comparisons with factored loading scenarios could be envisaged: On the one hand these would allow to gain more insight on whether the extrapolation is safe-sided. On the other hand these comparisons would help to avoid effects like parts of the membrane going slack, entailing a change of the load-bearing behavior. Looking at the non-linear effects and at the example from Figure 5.7, the resulting change of the load-bearing behavior cannot be covered by a factoring of the effect of action and has to be avoided at least for any loading scenario that may occur regularly.

### **Sensitivity analysis for assessing non-linear structural behavior**

As the discussions in the previous sections have shown, tensile structures cannot be uniformly classified into one of the categories for non-linear behavior according to Eurocode 0 [36]. In consequence an individual assessment of each structure could become necessary. However, the determination of the whole  $E(F)$ -graph by multiple evaluations for different load levels is very time-consuming, motivating the need for simpler methods.

In that regard Uhlemann et al. [144] propose a one-step sensitivity analysis as displayed in Figure 5.11 in orange. Starting from the dimensioning point

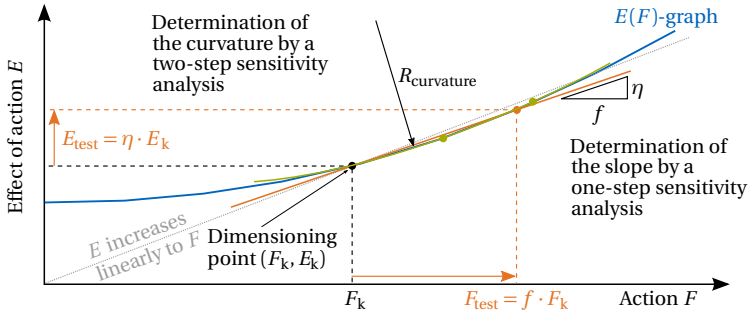


**Figure 5.11:** Classification according to Eurocode 0 with the help of a one- or two-step sensitivity analysis illustrated in orange and green, respectively

$(F_k, E_k)$  a second point on the  $E(F)$ -graph is determined by evaluating the system with an increased load  $F_{\text{test}} = f \cdot F_k$ , where  $f$  is an "arbitrary load increase factor" [144, p.5]. The resulting effect of action  $E_{\text{test}}$  is normalized with the characteristic value to give the "stress increase factor" [144, p.5]  $\eta = E_{\text{test}}/E_k$ . Comparing the ratio  $\eta/f$  to 1 allows a classification of the structure:

- For  $\eta/f > 1$  the structure behaves over-linearly,
- for  $\eta/f < 1$  the structure behaves under-linearly, and
- a ratio of  $\eta/f = 1$  is equivalent to linear structural behavior and corresponds to the gray dotted linearization in Figure 5.11.

This one-step sensitivity analysis as proposed by Uhlemann et al. [144] corresponds to the determination of the slope with the help of a secant. As can be seen by comparing the blue  $E(F)$ -graph to the gray dotted linear relation, this determination of the slope through a discrete differential quotient strongly depends on the evaluation interval and can thus be misleading.

A more complete image can be obtained by including second-order information with the help of a two-step sensitivity analysis as proposed in [119]:

As illustrated in Figure 5.11 in green, evaluating two more points reveals information on the curvature of the graph, *i.e.* whether it is concave or convex. In addition to the slope, this information considerably increases the conclusive range for a classification of the type of non-linearity.

### 5.3.3 Further aspects related to verification

As has been discussed in the previous section, already the classification of a structure into over- or under-linear behavior is delicate to be made. Whether it is possible to come to a unique classification for a structure, independent of the range of extrapolation, is highly questionable. Additionally, several other aspects related to the verification of structural membranes should be mentioned in this context and considered on the way towards a standardization of the verification of architectural membranes as representatives for structures with highly non-linear behavior.

#### The existence of a predominant action

By following category b) of Eurocode 0 for under-linear behavior (see Figure 5.2) and consequently factoring the effects of action  $E$  under a combination of characteristic actions  $F_i$ , only one uniform partial factor  $\gamma$  may be applied, leading to

$$E_d = \gamma \cdot E_k (F_{1,k} \oplus F_{2,k} \oplus F_{3,k} \oplus \dots) . \quad (5.13)$$

Thus the possibility to apply different partial factors to the respective actions  $F_i$  within a load combination is lost. One prerequisite for the application of the classification in Eurocode 0 [36, §6.3.2(4)] is the existence of "*a single predominant action*".

In general snow and wind-loads are the most important variable loads acting on structural membranes. Since these loads are commonly factored by the same partial factor of  $\gamma_Q = 1.5$ , they may be considered as one single "combined" action  $Q$  in this context. Besides from snow and wind, the stress in the membrane mainly results from the prestress  $P$ , which is introduced during the mounting of the structure.

In that context Uhlemann et al. [144] argue that the contribution of prestress to the overall stress level in a fully utilized membrane is small compared to the influence of the variable loads. Consequently the requirement

of the existence of a predominant action is considered fulfilled and the rules from Eurocode 0 may be applied. This assumption may be true in many cases, however it can certainly not be generalized. Therefore, the contribution of the different actions should be carefully judged for each new application.

### **Load transfer to the supporting structure**

The problem of not being able to separate different actions is even more accentuated when it comes to the interaction of different types of structures. Membrane structures are mounted on some kind of primary structure, supporting the textile membrane. This primary structure has to be verified at its turn, applying the material specific code (for the case of steelwork this would be Eurocode 3 [104]). These established material-specific codes prescribe the use of adapted load combinations with individual partial factors for the different actions. Here the problem becomes obvious: If for the membrane the load factor has been applied globally on the stresses computed for characteristic loads, the necessary individual load factors for the verification of the primary (steel) structure cannot be applied anymore and in consequence the separation of different effects is not possible any longer.

Looking at the load transfer from the textile membrane to the underlying structure, two aspects may be observed. As the membrane transfers the surface loads to the primary structure through tensile forces, this transfer includes the magnitude of the force on the one hand and its orientation on the other hand, as illustrated in Figure 5.12. The question of the force orientation may seem of little importance, but when considering the large deflections that may occur, it might be of interest for the dimensioning of the primary structure. Thus, the question is: Which load from the membrane should be applied to the structure? In which orientation? As stated above, the approach usually taken for the membrane – *i.e.* simulating the membrane with characteristic loads and applying the load factor on the effects of actions  $E$  – generally leads to reasonable values for the membrane design. This approach should then be continued consistently for the primary structure. In addition to the load, the effects of the deformed geometry and with it the altered orientation of the interaction forces between membrane and primary structures have to be examined.

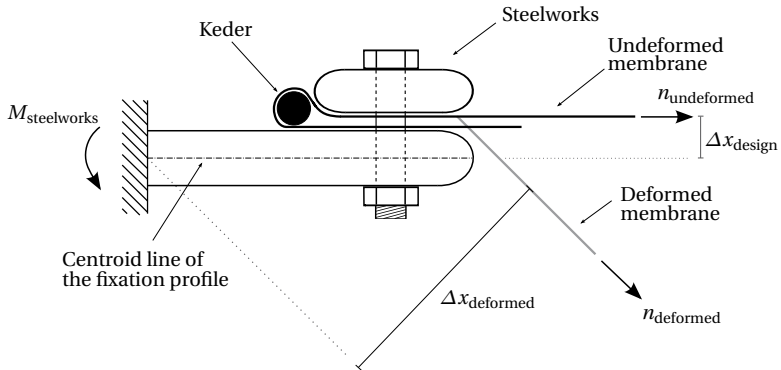


**Figure 5.12:** Schematic example of the impact of membrane deformation on eccentricities of the primary structure

In Figure 5.12 a schematic example of the load transfer from membrane to primary structure is presented. In order to determine the design value  $M_{steelworks,d}$  between the fixation profile and the general steelworks, the tension from the membrane has to be multiplied with its respective lever arm. It is obvious that even when assuming the same tensile force  $n$  for both the undeformed and the deformed state, the moment also depends on the lever arm  $\Delta x$ . While even for the design geometry an eccentricity  $\Delta x_{design}$  may have to be taken into account, this  $\Delta x$  might increase substantially during deformation.

It should be noted that for the case of *hybrid structures* as introduced in Section 4.1.2 the classification in a stiff primary structure and the prestressed secondary structure is not applicable any longer. In consequence, their analysis and assessment have to be realized for the integral structure as presented in Chapter 4. Being comparatively soft structures, the changing geometry under load (see Figure 5.12) may be even more important for hybrid structures. In that context robust and complete methods for the analysis of the mounting procedure of those hybrid structures as discussed in Section 4.3 and presented e.g. in Bauer et al. [15] and Philipp et al. [117] are necessary.

## 5.4 Methodological approach for the verification of safety with numerical models

To close this chapter, a different approach to the verification of safety is sketched, based on the example of the consideration of prestress for structural membranes.

Note that for the examples discussed in Section 5.3.2, a factoring of the prestress has not been taken into account. The prestress  $P$  has been applied as a characteristic value and only the snow load  $s$  has been multiplied by the corresponding load factor  $\gamma_Q$ .

### 5.4.1 Treatment of prestress in the context of safety verification

*A priori* it is clear that – just like all other parameters of a structure – the level of prestress cannot be guaranteed exactly. Whereas geometric deviations can be controlled rather easily, already the measurement of prestress in a mounted membrane is very difficult. Hence deviations<sup>12</sup> from a desired level of prestress have to be considered.

If the partial factors  $\gamma_F$  for actions are applied on the several single actions as described in Equation (5.4), the consideration of prestress requires special attention: As documented by Stranghöner et al. [136], two fundamentally different positions exist concerning the nature of prestress and consequently its treatment.

One position states that prestress  $P$  should be treated as an action since it contributes to the stresses in the structure. Consequently it has to be increased by a partial factor  $\gamma_{P,\text{unfavorable}} > 1.0$  for the consideration in a load combination. To give an order of magnitude, most standards propose a factor  $\gamma_{P,\text{unfavorable}}$  in the range of 1.2 to 1.35, see [103, 105, 106].

On the other hand prestress is fundamental for the load-bearing ability of structural membranes in combination with curvature. Therefore the opposed position states that prestress should be treated as a resistance and consequently rather be reduced by a factor  $\gamma_{P,\text{favorable}} \leq 1.0$ . Whereas some guidelines like the French Recommendations [12] propose a factor  $\gamma_{P,\text{favorable}} = 1.0$ , other propositions even reduce the prestress, by using a factor of e.g.  $\gamma_{P,\text{favorable}} = 0.8$  see the German National Annex to [106].

---

<sup>12</sup> Here time-dependent effects like loss of prestress due to creep are still neglected.

A detailed review of the different positions in this open discussion with their reasonings can be found in Stranghöner et al. [136]. As presented in Section 5.2.2, EN 1993-1-11 [105] gives prescriptions on that matter for the case of cable net structures.

### 5.4.2 Exploiting the numerical model for safety verification

A more general understanding of the nature of prestress can be found if prestress is not considered an input variable, but resulting from the assembly and mounting from separated cutting patterns to the completed structure, see Figure 2.18 and Section 2.5.2. Consequently prestress is the result of a process, which at its turn is influenced by various factors like material properties or the execution accuracy. Nevertheless this process can be simulated in the powerful analysis environments available nowadays. Thus in the context of verification of safety a treatment of non-linear behavior beyond general classifications and the discussion of factors could be reached.

Based on contemporary simulation environments, an approach to obtain meaningful verifications of safety could consist of the following combination of methods:

- (i) A structural model including all relevant construction stages (see Section 4.2) is able to reliably analyze the structure<sup>13</sup>. Here both the mounting procedure and relevant verification scenarios as listed in Section 5.3.1 need to be modeled. While setting up the model, the engineer implicitly defines the model parameters, *i.e.* relevant and possibly varying entities like geometric dimensions and material properties. These parameters are defined based on codes, early investigations and experience.
- (ii) Based on this structural model, a sensitivity analysis as proposed in Section 5.3.2 helps to gain insight on the sensitivity of structural responses (*e.g.* stresses or deflections) w.r.t. varying model parameters. Hence effects and sources of uncertainties can be identified: How would less stiff material influence the resulting stresses? What

---

<sup>13</sup> In general obviously also non-linear material behavior should be included in this model, although it is not within the scope of this thesis.

is the relation between a geometric deviation in the cutting pattern and the stresses under a snow load? With the help of the sensitivity analysis, these relations can be quantified (within the limit of the modeled parameters). Thus the impact and – consequently – the importance of different parameters can be indicated.

- (iii) The obtained sensitivities then need to be reflected against the "real" situation of the structure. In reality the model parameters correspond to scattering variables that often can be described with probability distributions.

Together with the determined sensitivities these distributions yield "model combinations", where unfavorable deviations of the variables might occur simultaneously.

Eventually for these combinations safety resp. an acceptable probability of failure (see Section 5.1.1) will have to be verified. In that context for each variable a combination of a high sensitivity (corresponding to an important impact) with a wide distribution (corresponding to important scattering of the variable of interest; *e.g.* a load intensity) requires more attention, whereas variables with a low sensitivity resp. a narrow distribution (*e.g.* the self weight of steel) might even be considered as fully determined.

For the first of these cases – high sensitivity and wide distribution – different conclusions can be drawn: Either a higher safety margin has to be accepted or the permissible tolerances need to be tightened (if possible).

It is obvious that economically it is – at least up to now – not possible to realize the entire proposed approach for every structure to be built. However, for more complex structures as discussed *e.g.* in Schmidt et al. [130] and especially in preparation of a future standard, see *e.g.* Gosling et al. [64], this combination of structural modeling, sensitivity analysis and the quantification of scattering variables in reality can help to gain substantial insight into the structural behavior which ultimately helps to provide safer and more meaningful verification requirements.

## Summary and conclusion of Chapter 5

Currently developments towards a unified standard for the design and safety verification of structural membranes are made. In that regard the basic concepts of safety verification considering non-linear structural behavior have been reviewed, focusing on tensile structures and the basic concepts of the Eurocodes.

As a contribution to the "*Prospect for European Guidance for the Structural Design of Tensile Membrane Structures*" [136], the following aspects have been elaborated and discussed more in detail:

- a presentation and comparison of currently existing verification guidelines for structural membranes;
- the classification of non-linearity according to Eurocode 0 [36] with an analytical example of a prestressed cable net;
- the different approaches to the application of partial factors with a full scale example of a prestressed structural membrane.

The development towards a Eurocode for structural membranes currently is focused quite much on the application of partial factors and the values to be applied for these factors. As has been discussed, the fixation of values still requires further investigations and discussion, whereas the scenarios to be considered are accepted more or less unanimously. In my opinion the most consistent approach towards reliable and economic verification concepts is a combination of sensitivity analysis and model calibration against real scattering of variables.

In general, the advances in analysis and modeling tools nowadays enable tension structure engineers to fulfill a more holistic part in the simulation and prediction of the structural behavior. The consideration of whole scenarios seems to better suit these possibilities than fixing all load combinations in prescribed verification cases, thus limiting the engineer in his responsibility and his freedom at the same time.



## CONCLUSIONS AND OUTLOOK

Lightweight structures are highly efficient solutions to structural challenges. They often dispose of pleasing aesthetics, characterized by their smooth curved shapes and an impressive slenderness as it is the case for the tensile structures and gridshells presented within this thesis. Therefore, lightweight structures offer an attractive playground for structural engineering, for which the following definition of James E. AMRHEIN [41, p. 16] holds especially true:

*"Structural Engineering is the art and science of molding Materials we do not fully understand; into Shapes we cannot precisely analyze; to resist Forces we cannot accurately predict; all in such a way that the society at large is given no reason to suspect the extent of our ignorance."*

Putting material modeling aside, AMRHEIN addresses the fields of geometrical design, structural analysis and verification of safety. In the case of lightweight structures, especially their geometrically non-linear behavior

entails considerable challenges compared to most conventional structures in civil engineering.

Within the present thesis, this non-linear behavior of lightweight structures and its impact on the design, analysis and verification have been discussed. For each of these fields, new developments and investigations have been made and critically assessed.

In order to enable an in-depth integration of geometry (within CAD) and structural behavior (with FEM) for the design and analysis of lightweight structures, *isogeometric B-Rep analysis* (IBRA) as a new analysis technique has been extended to the simulation of structural membranes. The developed components – notably a prestressed membrane element and a cable element following the novel paradigm of B-Rep edge elements – have been implemented in *Carat++* [29] and integrated in a plug-in to *Rhinoceros3D* [95] named *TeDA* [23]. In various applications the accuracy, robustness and ease of handling have been successfully demonstrated. At the same time the potential of IBRA for the design and analysis of lightweight structures has been critically assessed. (Chapter 3)

Lightweight structures and their load-bearing behavior are very sensitive w.r.t. their mounting procedure. In order to reliably simulate the state of the mounted structure in terms of deformed geometry resp. internal stresses, the deformation in the construction stages has to be tracked and their impact on the structure must be considered. Different established techniques for the configuration update between these stages have been presented, compared and discussed in detail, focusing on the application for geometrically non-linear behavior. Within selected examples, a mechanically consistent update method has been elaborated and evaluated in terms of accuracy and robustness. The introduction of side constraints – realized by the concept of contracting cables – has been discussed as an alternative approach together with its advantages in terms of convergence and handling in the application to highly deformable structures. (Chapter 4)

Existing concepts and guidelines for the verification in the presence of geometric non-linearity have been reviewed along with the underlying principles of the *Eurocodes*. As a contribution to the development of a future *Eurocode for Membrane Structures*, the classification of types of non-linearity and corresponding possible verification scenarios have been

investigated. The discussed examples, ranging from an analytical cable-net structure to a full scale structural membrane, have allowed to make propositions for future guidelines for the analysis and verification of tensile structures. (Chapter 5)

Of course this thesis cannot cover all aspects related to the non-linear behavior of lightweight structures resp. provide a perfect solution to all raised challenges, hence further research is required.

In the design process of lightweight structures, especially of structural membranes, the generation of cutting patterns is a crucial part. Here, the determination of cutting patterns on the basis of an isogeometric geometry description and making use of the applied B-Rep edge elements could bring substantial progress. The concept sketched in Section 3.3.3 of optimizing the cutting lines on the textile – corresponding to moving the trimming curves on the flat surface – seems very promising in this context. For the assembly of different structural members in a mounting simulation of the structure to be built, the data handling and robustness of the coupling still require further enhancement. A more general interpretation of the side constraints for geometric coupling as proposed by Bauer in [15] has already provided convincing first results.

Interpreting prestress as the resulting stress state from the mounting process could also be an important step towards a more consistent consideration of uncertainty and possible verification approaches: A sensitivity analysis of the mounting process can help to identify sensitivities of the structure w.r.t. variations in the model parameters like the material properties, the geometric execution accuracy or external loads. Based on these sensitivities and the distribution of the corresponding scattering variables in reality, a consistent and reliable verification approach could be established, beyond pure negotiations of values for partial factors.

Thus the structural engineer is placed in an active and creative position. In a long term this thesis shall have contributed to that aim by providing methods and investigations towards a more accurate and deeper integrated design, analysis and verification of lightweight structures.



## BIBLIOGRAPHY

- [1] S. Adanur, M. Günaydin, A. C. Altunişik, and B. Sevim. “Construction stage analysis of Humber Suspension Bridge.” In: *Applied Mathematical Modelling* 36.11 (Nov. 2012), pp. 5492–5505. DOI: 10.1016/j.apm.2012.01.011.
- [2] H. Alpermann. “Membranversteifte Tragwerke.” Dissertation. Berlin: Universität der Künste, Berlin, Feb. 2014.
- [3] H. Alpermann and C. Gengnagel. “Membranversteifte Bogentragwerke.” In: *Stahlbau* 78.8 (Aug. 2009), pp. 531–536. DOI: 10.1002/stab.200910066.
- [4] H. Alpermann and C. Gengnagel. “Membranversteifter Träger.” In: *Stahlbau* 81.5 (May 2012), pp. 373–378. DOI: 10.1002/stab.201201562.
- [5] American Society of Civil Engineers, ed. *Tensile membrane structures*. ASCE standard. OCLC: ocn651486957. Reston: American Society of Civil Engineers, 2010. ISBN: 978-0-7844-1097-4.
- [6] A. Apostolatos, R. Schmidt, R. Wüchner, and K.-U. Bletzinger. “A Nitsche-type formulation and comparison of the most common domain decomposition methods in isogeometric analysis.” In: *International Journal for Numerical Methods in Engineering* 97.7 (Sept. 2013), pp. 473–504. DOI: 10.1002/nme.4568.
- [7] F. Auricchio, L. Beirão da Veiga, J. Kiendl, C. Lovadina, and A. Reali. “Locking-free isogeometric collocation methods for spatial Timoshenko rods.” In: *Computer Methods in Applied Mechanics*

## Bibliography

- and Engineering* 263 (Aug. 2013), pp. 113–126. DOI: 10.1016/j.cma.2013.03.009.
- [8] M. R. Barnes. “Form Finding and Analysis of Tension Structures by Dynamic Relaxation.” In: *International Journal of Space Structures* 14.2 (June 1999), pp. 89–104. DOI: 10.1260/0266351991494722.
- [9] Y. Basar and W. Krätzig. *Mechanik der Flächentragwerke. Theorie, Berechnungsmethoden, Anwendungsbeispiele*. Braunschweig: Vieweg, 1985. ISBN: 978-3-528-08685-5.
- [10] K.-J. Bathe. *Finite element procedures*. OCLC: 732251900. Boston, Mass.: Bathe, 2006. ISBN: 978-0-9790049-0-2.
- [11] K.-J. Bathe and S. Bolourchi. “Large displacement analysis of three-dimensional beam structures.” In: *International Journal for Numerical Methods in Engineering* 14.7 (1979), pp. 961–986. DOI: 10.1002/nme.1620140703.
- [12] I. T. du Bâtiment et des Travaux Publiques (ITBTP), ed. *Recommandations pour la conception, la confection et la mise en oeuvre des ouvrages permanents de couverture textile*. OCLC: 494990269. Paris, France: SEBTP, 2009. ISBN: 978-2-35917-003-0.
- [13] A. M. Bauer, M. Breitenberger, B. Philipp, R. Wüchner, and K.-U. Bletzinger. “Embedded Structural Entities in NURBS-based Isogeometric Analysis.” In: *Computer Methods in Applied Mechanics and Engineering* (2017). submitted.
- [14] A. M. Bauer, M. Breitenberger, B. Philipp, R. Wüchner, and K.-U. Bletzinger. “Nonlinear isogeometric spatial Bernoulli beam.” In: *Computer Methods in Applied Mechanics and Engineering* 303 (May 2016), pp. 101–127. DOI: 10.1016/j.cma.2015.12.027.
- [15] A. M. Bauer, P. Längst, R. Wüchner, and K.-U. Bletzinger. “Isogeometric Analysis for Modeling and Simulation of Building Processes.” In: *"Interfaces: architecture.engineering.science" - Proceedings of the IASS Annual Symposium 2017*. (accepted). Hamburg, Germany, Sept. 2017.
- [16] Y. Bazilevs, V. M. Calo, Y. Zhang, and T. J. R. Hughes. “Isogeometric Fluid–structure Interaction Analysis with Applications to Arterial Blood Flow.” In: *Computational Mechanics* 38.4-5 (Sept. 2006), pp. 310–322. DOI: 10.1007/s00466-006-0084-3.

- [17] L. Beirão da Veiga, A. Buffa, J. Rivas, and G. Sangalli. “Some estimates for h–p–k-refinement in Isogeometric Analysis.” In: *Numerische Mathematik* 118.2 (June 2011), pp. 271–305. DOI: 10.1007/s00211-010-0338-z.
- [18] T. Belytschko, W. K. Liu, B. Moran, and K. I. Elkhodary. *Nonlinear finite elements for continua and structures*. Second edition. Chichester, West Sussex, United Kingdom: Wiley, 2014. ISBN: 978-1-118-63270-3.
- [19] D. Benson, Y. Bazilevs, M. Hsu, and T. Hughes. “Isogeometric shell analysis: The Reissner–Mindlin shell.” In: *Computer Methods in Applied Mechanics and Engineering* 199.5-8 (Jan. 2010), pp. 276–289. DOI: 10.1016/j.cma.2009.05.011.
- [20] D. Benson, S. Hartmann, Y. Bazilevs, M.-C. Hsu, and T. Hughes. “Blended isogeometric shells.” In: *Computer Methods in Applied Mechanics and Engineering* 255 (Mar. 2013), pp. 133–146. DOI: 10.1016/j.cma.2012.11.020.
- [21] M. Bischoff, K.-U. Bletzinger, W. A. Wall, and E. Ramm. “Models and Finite Elements for Thin-Walled Structures.” In: *Encyclopedia of Computational Mechanics*. Ed. by E. Stein, R. de Borst, and T. J. R. Hughes. Chichester, UK: John Wiley & Sons, Ltd, Nov. 2004. ISBN: 978-0-470-09135-7.
- [22] M. Bischoff. “Nicht auf Knopfdruck - Computerstatik am Gesamtmodell: Gedanken über Modellierung, Berechnung und Kontrolle.” In: *Deutsches IngenieurBlatt* 12.12 (2011), pp. 18–22.
- [23] K.-U. Bletzinger. *TeDA - Tool to enhance Design by Analysis*. web-page: [www.st.bgu.tum.de/en/lehre0/research/teda/](http://www.st.bgu.tum.de/en/lehre0/research/teda/). 2017.
- [24] K.-U. Bletzinger, F. Dieringer, and B. Philipp. “Numerische Methoden für Formfindung, Simulation und Zuschnitt von Membrantragwerken.” In: *Essener Membranbau Symposium 2012*. Ed. by N. Stranghöner and K. Saxe. Essen: Shaker, 2012, pp. 97–118. ISBN: 978-3-8440-1348-1.
- [25] K.-U. Bletzinger, M. Firl, J. Linhard, and R. Wüchner. “Optimal shapes of mechanically motivated surfaces.” In: *Computer Methods in Applied Mechanics and Engineering* 199.5-8 (Jan. 2010), pp. 324–333. DOI: 10.1016/j.cma.2008.09.009.

## Bibliography

- [26] K.-U. Bletzinger, J. Linhard, and R. Wüchner. “Extended and integrated numerical form finding and patterning of membrane structures.” In: *Journal of the International Association for Shell and Spatial Structures* 50.1 (Apr. 2009), pp. 35–49.
- [27] K.-U. Bletzinger and E. Ramm. “A General Finite Element Approach to the Form Finding of Tensile Structures by the Updated Reference Strategy.” In: *International Journal of Space Structures* 14.2 (June 1999), pp. 131–145. DOI: 10.1260/0266351991494759.
- [28] K.-U. Bletzinger, R. Wüchner, F. Daoud, and N. Camprubí. “Computational methods for form finding and optimization of shells and membranes.” In: *Computer Methods in Applied Mechanics and Engineering* 194.30-33 (Aug. 2005), pp. 3438–3452. DOI: 10.1016/j.cma.2004.12.026.
- [29] K.-U. Bletzinger. *Carat++*. web-page: <http://www.st.bgu.tum.de/en/lehre0/research/carat/>. 2017.
- [30] A. Bown, T. Makin, and D. Wakefield. “Beyond Static Analysis: Investigation of Membrane Structure Performance Using Time Stepping, Transient and Progressive Analyses.” In: *Procedia Engineering* 155 (2016), pp. 313–322. DOI: 10.1016/j.proeng.2016.08.034.
- [31] M. Breitenberger, A. Apostolatos, B. Philipp, R. Wüchner, and K.-U. Bletzinger. “Analysis in computer aided design: Nonlinear isogeometric B-Rep analysis of shell structures.” In: *Computer Methods in Applied Mechanics and Engineering* 284 (Feb. 2015), pp. 401–457. DOI: 10.1016/j.cma.2014.09.033.
- [32] M. Breitenberger. “CAD-integrated Design and Analysis of Shell Structures.” PhD thesis. München, Germany: Technische Universität München, Nov. 2016.
- [33] B. N. Bridgens and M. Birchall. “Form and function: The significance of material properties in the design of tensile fabric structures.” In: *Engineering Structures* 44 (Nov. 2012), pp. 1–12. DOI: 10.1016/j.engstruct.2012.05.044.
- [34] B. N. Bridgens, P. D. Gosling, and M. J. S. Birchall. “Membrane material behaviour: concepts, practice & developments.” In: *Structural Engineer* 82.14 (2004), pp. 28–33.

- [35] British Standards Institution. *Eurocode 3: Design of steel structures - Part 1-11: Design of structures with tension components; English Version BS EN 1993-1-11:2006*. BS EN 1993-1-11:2006. London: BSI, 2006.
- [36] British Standards Institution. *Eurocode: basis of structural design; English Version BS EN 1990:2002*. BS EN 1990:2002. London: BSI, 2002.
- [37] M. Buonomo, C. Servant, M. Virlogeux, J.-M. Cremer, V. de Ville de Goyet, and J.-Y. del Forno. "The design and the construction of the Millau Viaduct." In: *Proceedings of the International Symposium on Steel Bridges 2004*. Millau, France, June 2004.
- [38] B. Burkhardt, F. Otto, and I. Schmall, eds. *Zelte*. ger eng. Mitteilungen des Instituts für Leichte Flächentragwerke (IL) IL 16. OCLC: 247238266. Stuttgart: Institut für Leichte Flächentragwerke [u.a.], 1976. ISBN: 978-3-7828-2016-5.
- [39] B. Burkhardt and Sonderforschungsbereich Weitgespannte Flächentragwerke, eds. *Multihalle Mannheim: [zugleich ein Bericht des Teilprojektes "Erfahrungen am Bauwerk" des Sonderforschungsbereichs 64 "Weitgespannte Flächentragwerke" der Deutschen Forschungsgemeinschaft]*. Mitteilungen des Instituts für Leichte Flächentragwerke (IL) IL 13. OCLC: 246761872. Stuttgart: Institut für Leichte Flächentragwerke [u.a.], 1978. ISBN: 978-3-7828-2013-4.
- [40] J.-F. Caron, S. Julich, and O. Baverel. "Selfstressed bowstring footbridge in FRP." In: *Composite Structures* 89.3 (July 2009), pp. 489–496. DOI: 10.1016/j.compstruct.2008.11.009.
- [41] K. L. Carper, ed. *Forensic engineering*. 2nd ed. Boca Raton, FL: CRC Press, 2001. ISBN: 978-0-8493-7484-5.
- [42] B. K. Choi. *Surface modeling for CAD/CAM*. Advances in industrial engineering 11. Amsterdam ; New York: Elsevier, 1991. ISBN: 978-0-444-88482-4.
- [43] A. Coll Sans. "Robust volume mesh generation for non-watertight geometries." PhD thesis. Barcelona, Spain: Universitat Politècnica de Catalunya, May 2014.

## Bibliography

- [44] C. J. Costa. “Example of a complete minimal immersion in IR<sup>3</sup> of genus one and three-embedded ends.” In: *Boletim da Sociedade Brasileira de Matemática* 15.1-2 (Mar. 1984), pp. 47–54. DOI: 10.1007/BF02584707.
- [45] J. A. Cottrell. *Isogeometric analysis: toward integration of CAD and FEA*. Chichester, West Sussex, U.K. ; Hoboken, NJ: Wiley, 2009. ISBN: 978-0-470-74873-2.
- [46] J. Cottrell, T. Hughes, and A. Reali. “Studies of refinement and continuity in isogeometric structural analysis.” In: *Computer Methods in Applied Mechanics and Engineering* 196.41-44 (Sept. 2007), pp. 4160–4183. DOI: 10.1016/j.cma.2007.04.007.
- [47] J.-M. Cremer, V. de Ville de Goyet, and J.-Y. del Forno. *Le grand Viaduc de Millau*. Project report. Bureau d’études Greisch - Greisch Ingénierie, Mar. 2004, p. 16.
- [48] M. A. Crisfield. *Non-linear finite element analysis of solids and structures*. Chichester ; New York: Wiley, 1991. ISBN: 978-0-471-92956-7.
- [49] F. Dieringer. “Numerical methods for the design and analysis of tensile structures.” OCLC: 897478085. PhD thesis. München, Germany: Technische Universität München, 2014.
- [50] F. Dieringer, B. Philipp, R. Wüchner, and K.-U. Bletzinger. “Numerical Methods for the Design and Analysis of Hybrid Structures.” In: *International Journal of Space Structures* 28.3 (Sept. 2013), pp. 149–160. DOI: 10.1260/0266-3511.28.3-4.149.
- [51] F. Dieringer, R. Wüchner, and K.-U. Bletzinger. “Practical advances in numerical form finding and cutting pattern generation for membrane structures.” In: *Journal of the International Association for Shell and Spatial Structures (J. IASS)* 53.3 (Sept. 2012), pp. 147–156.
- [52] F. Dieringer, R. Wüchner, and K.-U. Bletzinger. “The eXtended Updated Reference Strategy for the Form Finding of Tensile Structures.” In: *Structural Membranes 2013 - VI International Conference on Textile Composites and Inflatable Structures*. München, Germany, Oct. 2013. ISBN: 978-84-941531-9-8.

- [53] W. Dornisch, S. Klinkel, and B. Simeon. “Isogeometric Reissner–Mindlin shell analysis with exactly calculated director vectors.” In: *Computer Methods in Applied Mechanics and Engineering* 253 (Jan. 2013), pp. 491–504. DOI: 10.1016/j.cma.2012.09.010.
- [54] C. Douthe, O. Baverel, and J.-F. Caron. “Form-finding of a grid shell in composite materials.” In: *Journal of the International Association for Shell and Spatial Structures* 47.150 (2006), pp. 53–62.
- [55] D. Eberly. *Rotation Representations and Performance Issues*. Tech. rep. Geometric Tools, LLC, 2008.
- [56] R. Echter, B. Oesterle, and M. Bischoff. “A hierarchic family of isogeometric shell finite elements.” In: *Computer Methods in Applied Mechanics and Engineering* 254 (Feb. 2013), pp. 170–180. DOI: 10.1016/j.cma.2012.10.018.
- [57] L. Euler. *Methodus inveniendi lineas curvas maximi minimive proprietate gaudentes (appendix, de curvis elasticis)*. Lausanne and Geneve, 1744.
- [58] J. R. C. of the European Commission. *Eurocodes: Building the future - The European Commission website on the Eurocodes*, <http://eurocodes.jrc.ec.europa.eu/showpage.php?id=11>. Jan. 2017.
- [59] C. Felippa. “Nonlinear Finite Element Methods.” University of Colorado at Boulder, USA, 2016.
- [60] B. Forster and M. Mollaert, eds. *European design guide for tensile surface structures: TensiNet*. OCLC: 249654651. Brussel: Vrije Univ. Brussel, 2004. ISBN: 978-90-808687-1-7.
- [61] N. D. Gibson. “How to get a membrane structure off the drawing board.” In: *Steel Construction* 8.4 (Nov. 2015), pp. 244–250. DOI: 10.1002/stco.201510034.
- [62] A.-K. Goldbach, M. Breitenberger, A. Widhammer, and K.-U. Bletzinger. “Computational Cutting Pattern Generation Using Isogeometric B-Rep Analysis.” In: *Procedia Engineering* 155 (2016), pp. 249–255. DOI: 10.1016/j.proeng.2016.08.026.

## Bibliography

- [63] C. W. B. Goldschmidt. *Determinatio superficiei minimae rotatione curvae data duo puncta jungentis circa datum axem ortae*. Göttingen, 1831.
- [64] P. Gosling, B. Bridgens, and L. Zhang. "Adoption of a reliability approach for membrane structure analysis." In: *Structural Safety* 40 (Jan. 2013), pp. 39–50. DOI: 10.1016/j.strusafe.2012.09.002.
- [65] P. Gosling et al. "Analysis and design of membrane structures: Results of a round robin exercise." In: *Engineering Structures* 48 (Mar. 2013), pp. 313–328. DOI: 10.1016/j.engstruct.2012.10.008.
- [66] L. Greco and M. Cuomo. "B-Spline interpolation of Kirchhoff-Love space rods." In: *Computer Methods in Applied Mechanics and Engineering* 256 (Apr. 2013), pp. 251–269. DOI: 10.1016/j.cma.2012.11.017.
- [67] E. Happold and I. Liddell. "Timber lattice roof for the Mannheim Bundesgartenschau." In: *The Structural Engineer* 3.53 (Mar. 1975), pp. 99–135.
- [68] E. Haug. *Finite Element Analysis of Nonlinear Membrane Structures*. UCB/SESM Reports 1972/07. Berkeley, California: University of California, Berkeley, Feb. 1972.
- [69] S. Heyden. *Implementierung eines corotational Balkenelements und Anwendung an hybriden und biegeaktiven Tragwerken*. Tech. rep. Lehrstuhl für Statik, Technische Universität München, Oct. 2015.
- [70] D. Hitrec and E. Schling. *Design Studio "Experimental Structures" – "Asymptotic Pavilion"*. Tech. rep. München, Germany: Lehrstuhl für Tragwerksplanung, Technische Universität München, Sept. 2016.
- [71] C. M. Hoffmann. *Geometric and solid modeling: an introduction*. The Morgan Kaufmann series in computer graphics and geometric modeling. San Mateo, Calif: Morgan Kaufmann, 1989. ISBN: 1-55860-067-1.

- [72] G. A. Holzapfel. *Nonlinear solid mechanics: a continuum approach for engineering*. Chichester ; New York: Wiley, 2000. ISBN: 0-471-82304-X.
- [73] T. J. R. Hughes, J. A. Cottrell, and Y. Bazilevs. “Isogeometric analysis: CAD, finite elements, NURBS, exact geometry and mesh refinement.” In: *Computer Methods in Applied Mechanics and Engineering* 194.39-41 (Oct. 2005), pp. 4135–4195. DOI: 10.1016/j.cma.2004.10.008.
- [74] T. J. R. Hughes. *The finite element method: linear static and dynamic finite element analysis*. Mineola, NY: Dover Publications, 2000. ISBN: 978-0-486-41181-1.
- [75] C. Isenberg. *The science of soap films and soap bubbles*. New York: Dover Publications, 1992. ISBN: 0-486-26960-4.
- [76] M. Itskov. *Tensor algebra and tensor analysis for engineers: with applications to continuum mechanics*. Third edition. Mathematical engineering. Heidelberg: Springer, 2013. ISBN: 978-3-642-30878-9.
- [77] A. Jrusjungiak. “Nonlinear Analysis of Pneumatic Membranes: From Subgrid to Interface.” PhD thesis. München, Germany: Technische Universität München, Oct. 2009.
- [78] K. Kathage and T. Misiak. “Bemessung von Zuggliedern nach DIN EN 1993-1-11 - Grenzzustände der Gebrauchstauglichkeit.” In: *Stahlbau* 81.8 (Aug. 2012), pp. 621–623. DOI: 10.1002/stab.201201592.
- [79] J. Kiendl, K.-U. Bletzinger, J. Linhard, and R. Wüchner. “Isogeometric shell analysis with Kirchhoff–Love elements.” In: *Computer Methods in Applied Mechanics and Engineering* 198.49-52 (Nov. 2009), pp. 3902–3914. DOI: 10.1016/j.cma.2009.08.013.
- [80] E. Klingbeil. *Tensorrechnung für Ingenieure*. OCLC: 180599935. Mannheim [u.a.]: BI-Wiss.-Verl., 1966. ISBN: 978-3-411-00197-2.
- [81] J. Knippers, J. Cremers, M. Gabler, J. Lienhard, and Institut für Internationale Architektur-Dokumentation, eds. *Atlas Kunststoffe + Membranen: Werkstoffe und Halbzeuge, Formfindung und Konstruktion*. 1. Aufl. Edition Detail. OCLC: 680747875. München:

## Bibliography

- Inst. f. Internat. Architektur-Dokumentation, 2010. ISBN: 978-3-920034-41-6.
- [82] S. Krenk. *Non-linear modeling and analysis of solids and structures*. OCLC: ocm60667968. Cambridge, UK ; New York: Cambridge University Press, 2009. ISBN: 978-0-521-83054-6.
- [83] F. Leonhardt. "Leichtbau - eine Forderung unserer Zeit." In: *Die Bautechnik* 18.36/37 (Aug. 1940), pp. 413–423.
- [84] J. Lienhard, R. La Magna, and J. Knippers. "Form-finding bending-active structures with temporary ultra-elastic contraction elements." In: June 2014, pp. 107–115. DOI: 10.2495/MAR140091.
- [85] J. Lienhard. *Bending-active structures: form-finding strategies using elastic deformation in static and kinetic systems and the structural potentials therein*. Forschungsberichte aus dem Institut für Tragkonstruktionen und Konstruktives Entwerfen, Universität Stuttgart 36. Stuttgart: ITKE, 2014. ISBN: 978-3-922302-36-0.
- [86] J. Lienhard, H. Alpermann, C. Gengnagel, and J. Knippers. "Active Bending, A Review on Structures where Bending is used as a Self-Formation Process." In: *International Journal of Space Structures* 28.3-4 (Sept. 2013). Ed. by C. Gengnagel, pp. 187–196. DOI: 10.1260/0266-3511.28.3-4.187.
- [87] J. Lienhard and J. Knippers. "Permanent and convertible membrane structures with intricate bending-active support systems." In: *Proceedings of the International IASS Symposium, Seoul, Korea*. Seoul, Korea, 2012.
- [88] J. Linhard. "Numerisch-mechanische Betrachtung des Entwurfsprozesses von Membrantragwerken." OCLC: 680674738. PhD thesis. München, Germany: Technische Universität München, 2009.
- [89] K. Linkwitz. "Formfinding by the "Direct Approach" and Pertinent Strategies for the Conceptual Design of Prestressed and Hanging Structures." In: *International Journal of Space Structures* 14.2 (June 1999), pp. 73–87. DOI: 10.1260/0266351991494713.
- [90] J. G. Löwenstein. "Bauen unter Gravitation - Verformungsausgleich im Baufortschritt." In: *mb AEC Software GmbH: mb-news* 4/2014 (2014), pp. 14–19.

- [91] G. Lumpe and V. Gensichen. *Evaluierung der linearen und nichtlinearen Stabstatik in Theorie und Software: Prüfbeispiele, Fehlerursachen, genaue Theorie*. Bauingenieur-Praxis. OCLC: 876292436. Berlin: Ernst, 2014. ISBN: 978-3-433-03053-0.
- [92] T. Maekawa. "Computation of Shortest Paths on Free-Form Parametric Surfaces." In: *Journal of Mechanical Design* 118.4 (1996), p. 499. DOI: 10.1115/1.2826919.
- [93] M. Mäntylä. *An introduction to solid modeling*. Principles of computer science series 13. Rockville, Md: Computer Science Press, 1988. ISBN: 0-88175-108-1.
- [94] G. Marzahn, H. Grassl, G. Buddenkotte, D. Schummer, and G. Bogdan. "Neubau der Talbrücke Nuttlar bei Bestwig – höchste Talbrücke in Nordrhein-Westfalen." In: *Tagungsband 24. Dresdner Brückenbausymposium 2014*. Dresden: Institut für Massivbau, Technische Universität Dresden, 2014, pp. 107–126. ISBN: ISBN 978-3-86780-369-4.
- [95] McNeel. *Rhinoceros*. web-page: [www.rhino3d.com](http://www.rhino3d.com).
- [96] G. Mehlhorn, M. Curbach, and F. Aigner, eds. *Handbuch Brücken: Entwerfen, Konstruieren, Berechnen, Bauen und Erhalten*. 3. Aufl. OCLC: 931640749. Wiesbaden: Springer Vieweg, 2014. ISBN: 978-3-658-03339-2.
- [97] C. Meier, A. Popp, and W. A. Wall. "A locking-free finite element formulation and reduced models for geometrically exact Kirchhoff rods." In: *Computer Methods in Applied Mechanics and Engineering* 290 (June 2015), pp. 314–341. DOI: 10.1016/j.cma.2015.02.029.
- [98] J.-B. Meusnier. "Mémoire sur la courbure des surfaces." In: *Savans Étrangers*. Vol. 10. Paris, 1785, pp. 477–510.
- [99] J. Minte. "Das mechanische Verhalten von Verbindungen beschichteter Chemiefasergewebe." Deutsch. PhD thesis. Aachen, Germany: RWTH Aachen, 1981.
- [100] K. Moritz. "ETFE-Folie als Tragelement." PhD thesis. München, Germany: Technische Universität München, 2007.

## Bibliography

- [101] F. Müller and R. Stannarius. "Collapse of catenoid-shaped smectic films." In: *Europhysics Letters (EPL)* 76.6 (Dec. 2006), pp. 1102–1108. DOI: 10.1209/epl/i2006-10397-8.
- [102] R. Münsch and H. Reinhardt. "Zur Berechnung von Membrantragwerken aus beschichteten Geweben mit Hilfe genäherter elastischer Materialparameter." In: *Bauingenieur* 70.6 (1995), pp. 271–275.
- [103] Normenausschuss Bauwesen (NABau) im DIN. *DIN 4134(1983) - Tragluftbauten - Berechnung, Ausführung und Betrieb*. Berlin: DIN, 1983.
- [104] Normenausschuss Bauwesen (NABau) im DIN. *Eurocode 3: Bemessung und Konstruktion von Stahlbauten - Teil 1-1: Allgemeine Bemessungsregeln und Regeln für den Hochbau; Deutsche Fassung EN 1993-1-1:2005 + AC:2009*. DIN EN 1993-1-1:2005. Berlin: DIN, 2010.
- [105] Normenausschuss Bauwesen (NABau) im DIN. *Eurocode 3: Bemessung und Konstruktion von Stahlbauten - Teil 1-11: Bemessung und Konstruktion von Tragwerken mit Zuggliedern aus Stahl; Deutsche Fassung EN 1993-1-11:2006 + AC:2009*. DIN EN 1993-1-11:2006. Berlin: DIN, 2010.
- [106] Normenausschuss Bauwesen (NABau) im DIN. *Eurocode: Grundlagen der Tragwerksplanung; Deutsche Fassung EN 1990:2002 + A1:2005 + A1:2005/AC:2010*. DIN EN 1990:2002. Berlin: DIN, 2002.
- [107] R. Off. "New trends on membrane and shell structures – examples of bat-sail and cushion-belt technologies." In: *Structures and architecture: proceedings of the First International Conference on Structures and Architecture*. Ed. by P. J. d. S. Cruz. Boca Raton, Fla.: CRC Press, 2010. ISBN: 978-0-415-49249-2.
- [108] R. W. Ogden. *Non-linear elastic deformations*. Mineola, N.Y: Dover Publications, 1997. ISBN: 978-0-486-69648-5.
- [109] C. Osorio. *A parallelized embedded fluid-structure interaction approach for thin-walled isogeometric structures*. Tech. rep. München, Germany: Lehrstuhl für Statik, Technische Universität München, Apr. 2017.

- [110] H. Parisch. *Festkörper-Kontinuumsmechanik: von den Grundgleichungen zur Lösung mit Finiten Elementen*. 1. Aufl. Teubner Studienbücher Technik - Lehrbuch. OCLC: 76440309. Stuttgart: Teubner, 2003. ISBN: 978-3-519-00434-9.
- [111] L. D. Peloux, F. Tayeb, O. Baverel, and J.-F. Caron. "Construction of a Large Composite Gridshell Structure: A Lightweight Structure Made with Pultruded Glass Fibre Reinforced Polymer Tubes." In: *Structural Engineering International* 26.2 (May 2016), pp. 160–167. DOI: 10.2749/101686616X14555428758885.
- [112] C. Petersen. *Statik und Stabilität der Baukonstruktionen: elasto- und plasto-statische Berechnungsverfahren druckbeanspruchter Tragwerke ; Nachweisformen gegen Knicken, Kippen, Beulen*. 2., durchges. Aufl., Nachdr. OCLC: 257926255. Braunschweig: Vieweg, 1992. ISBN: 978-3-528-18663-0.
- [113] B. Philipp and K.-U. Bletzinger. "Hybrid Structures - Enlarging the Design Space of Architectural Membranes." In: *Journal of the International Association for Shell and Spatial Structures (J. IASS)* 54.4 (Dec. 2013), pp. 281–291.
- [114] B. Philipp, M. Breitenberger, I. D’Auria, R. Wüchner, and K.-U. Bletzinger. "Integrated design and analysis of structural membranes using the Isogeometric B-Rep Analysis." In: *Computer Methods in Applied Mechanics and Engineering* 303 (May 2016), pp. 312–340. DOI: 10.1016/j.cma.2016.02.003.
- [115] B. Philipp, M. Breitenberger, R. Wüchner, and K.-U. Bletzinger. "Design of architectural membranes with isogeometric elements." In: *Proceedings of WCCM 2014 - 11th. World Congress on Computational Mechanics*. Vol. II. Barcelona: E-book Congreso mundial, 2014, pp. 303–314. ISBN: 978-84-942844-7-2.
- [116] B. Philipp, M. Breitenberger, R. Wüchner, and K.-U. Bletzinger. "Form-Finding of Architectural Membranes in a CAD-Environment Using the AiCAD-Concept." In: *Modelling Behaviour*. Ed. by M. R. Thomsen, M. Tamke, C. Gengnagel, B. Faircloth, and F. Scheurer. Cham: Springer International Publishing, 2015, pp. 65–74. ISBN: 978-3-319-24206-4.

## Bibliography

- [117] B. Philipp, F. Dieringer, R. Wüchner, and K.-U. Bletzinger. “Form-finding and structural analysis for the design of hybrid structures.” In: *Journal of the International Association for Shell and Spatial Structures* 56.1 (Mar. 2015), pp. 17–24.
- [118] B. Philipp, R. Wüchner, and K.-U. Bletzinger. “Advances in the Form-finding of Structural Membranes.” In: *Procedia Engineering* 155 (2016), pp. 332–341. DOI: 10.1016/j.proeng.2016.08.036.
- [119] B. Philipp, R. Wüchner, and K.-U. Bletzinger. “Conception and Design of Membrane Structures considering their Non-linear Behavior.” In: *Structural Membranes 2013 - VI International Conference on Textile Composites and Inflatable Structures*. Ed. by K.-U. Bletzinger and E. Oñate. Munich, Germany, 2013. ISBN: 978-84-941686-0-4.
- [120] L. Piegl and W. Tiller. *The NURBS Book*. Berlin, Heidelberg: Springer Berlin Heidelberg, 1997. ISBN: 978-3-642-59223-2.
- [121] K. Polthier and M. Schmies. “Straightest geodesics on polyhedral surfaces.” In: ACM Press, 2006, p. 30. ISBN: 1-59593-364-6. DOI: 10.1145/1185657.1185664.
- [122] H. Pottman, A. Asperl, M. Hofer, and A. Kilian. *Architectural geometry*. Ed. by D. Bentley. 1. ed. OCLC: 254158762. Exton, Pa: Bentley Inst. Press, 2007. ISBN: 978-1-934493-04-5.
- [123] S. Raknes, X. Deng, Y. Bazilevs, D. Benson, K. Mathisen, and T. Kvamsdal. “Isogeometric rotation-free bending-stabilized cables: Statics, dynamics, bending strips and coupling with shells.” In: *Computer Methods in Applied Mechanics and Engineering* 263 (Aug. 2013), pp. 127–143. DOI: 10.1016/j.cma.2013.05.005.
- [124] R. Rossi, M. Lazzari, R. Vitaliani, and E. Oñate. “Simulation of light-weight membrane structures by wrinkling model.” In: *International Journal for Numerical Methods in Engineering* 62.15 (Apr. 2005), pp. 2127–2153. DOI: 10.1002/nme.1266.
- [125] T. Rumpel and K. Schweizerhof. “Volume-dependent pressure loading and its influence on the stability of structures.” In: *International Journal for Numerical Methods in Engineering* 56.2 (2003), pp. 211–238.

- [126] R. A. Sauer, T. X. Duong, and C. J. Corbett. “A computational formulation for constrained solid and liquid membranes considering isogeometric finite elements.” In: *Computer Methods in Applied Mechanics and Engineering* 271 (Apr. 2014), pp. 48–68. DOI: 10.1016/j.cma.2013.11.025.
- [127] H. Scherk. “Bemerkungen über die kleinste Fläche innerhalb gegebener Grenzen.” In: *Journal für die reine und angewandte Mathematik* 13 (1834), pp. 185–208.
- [128] L. Schiemann. “Tragverhalten von ETFE-Folien unter biaxialer Beanspruchung.” PhD thesis. München, Germany: Technische Universität München, 2009.
- [129] E. Schling and R. Barthel. “Experimentelle Studien zur Konstruktion zweifach gekrümmter Gitterstrukturen.” In: *DETAIL structure* 01/2017 (Apr. 2017), pp. 51–56.
- [130] H. Schmidt, J. Schneider, and R. Kemmler. “Versagenswahrscheinlichkeit und Bemessung von Zuggliedern in Ringseildächern für Stadien.” In: *Baustatik - Baupraxis 12*. Ed. by K.-U. Bletzinger, N. Gebekken, and R. Fisch. Vol. 12. Baustatik - Baupraxis. München, Germany, 2014. ISBN: 978-3-00-041256-1.
- [131] H. Schwarz. *Gesammelte mathematische Abhandlungen*. Berlin: Springer, 1890.
- [132] K. Schweizerhof and E. Ramm. “Displacement dependent pressure loads in nonlinear finite element analyses.” In: *Computers & Structures* 18.6 (1984), pp. 1099–1114.
- [133] B. Stimpfle. “From NURBS to Textile Architecture.” In: *Structural Membranes 2013 - VI International Conference on Textile Composites and Inflatable Structures*. München, Germany, Oct. 2013, pp. 132–141. ISBN: 978-84-941686-0-4.
- [134] B. Stimpfle and M. Schäffer. “Membrantragwerke.” In: *Stahlbau Kalender 2015*. Ed. by U. Kuhlmann. Weinheim, Germany: Wiley-VCH Verlag GmbH & Co. KGaA, June 2015, pp. 517–566. ISBN: 978-3-433-60521-9.
- [135] G. Strang and G. J. Fix. *An analysis of the finite element method*. Wellesley, MA: Wellesley-Cambridge, 2008. ISBN: 0-9802327-0-8.

## Bibliography

- [136] N. Stranghöner et al. *Prospect for European guidance for the structural design of tensile membrane structures: support to the implementation, harmonization and further development of the Eurocodes*. OCLC: 948770738. Luxembourg: Publications Office, 2016. ISBN: 978-92-79-54652-5.
- [137] I. Stroud. *Boundary Representation Modelling Techniques*. London: Springer London, 2006. ISBN: 978-1-84628-312-3.
- [138] F. Tayeb, J.-F. Caron, O. Baverel, and L. Du Peloux. "Stability and robustness of a 300m<sup>2</sup> composite gridshell structure." In: *Construction and Building Materials* 49 (Dec. 2013), pp. 926–938. DOI: 10.1016/j.conbuildmat.2013.04.036.
- [139] F. Tayeb, O. Baverel, J.-F. Caron, and L. Du Peloux. "Construction of gridshells composed of elastically bended elements and covered by a stretched three-dimensional membrane." In: *Structural Membranes 2013 - VI International Conference on Textile Composites and Inflatable Structures*. München, Germany, Oct. 2013. ISBN: 978-84-941686-0-4.
- [140] K. C. Terwel. "Structural safety: study into critical factors in the design and construction process." OCLC: 905871042. PhD thesis. Delft, The Netherlands: Delft University of Technology, June 2014.
- [141] J. Tomlow. "Designing and constructing the Olympic roof (Munich 1972)." In: *International Journal of Space Structures* 31.1 (Mar. 2016), pp. 62–73. DOI: 10.1177/0266351116642078.
- [142] B. H. V. Topping, ed. *Finite element mesh generation*. Saxe-Coburg publications on computational engineering. OCLC: 249095769. Kippen: Saxe-Coburg Publ, 2004. ISBN: 978-1-874672-10-4.
- [143] J. Uhlemann. "Elastic constants of architectural fabrics for design purposes." OCLC: 950458942. PhD thesis. Duisburg-Essen: Universität Duisburg-Essen, May 2016.
- [144] J. Uhlemann, B. Stimpfle, and N. Stranghöner. "Application of the semiprobabilistic safety concept of EN 1990 in the design of prestressed membrane structures." In: *Proceedings of the EUROSTEEL 2014*. Naples, Italy, Sept. 2014.

- [145] D. Wakefield. "Engineering analysis of tension structures: theory and practice." In: *Engineering Structures* 21.8 (Aug. 1999), pp. 680–690. DOI: 10.1016/S0141-0296(98)00023-6.
- [146] D. Wakefield. "Grundlagen und Berechnung von Membrankonstruktionen." In: *Bauen mit Membranen*. Ed. by K.-M. Koch. München: Prestel-Verlag, 2004. ISBN: 3-7913-3048-9.
- [147] S. W. Walker. *The shapes of things: a practical guide to differential geometry and the shape derivative*. Advances in design and control. Philadelphia: Society for Industrial and Applied Mathematics, 2015. ISBN: 978-1-61197-395-2.
- [148] A. Widhammer. "Variation of Reference Strategy – Generation of Optimized Cutting Patterns for Textile Fabrics." PhD thesis. München, Germany: Technische Universität München, Nov. 2015.
- [149] P. Wriggers. *Nonlinear finite element methods*. OCLC: ocn236120878. Berlin: Springer, 2008. ISBN: 978-3-540-71000-4.
- [150] R. Wüchner and K.-U. Bletzinger. "Stress-adapted numerical form finding of pre-stressed surfaces by the updated reference strategy." In: *International Journal for Numerical Methods in Engineering* 64.2 (Sept. 2005), pp. 143–166. DOI: 10.1002/nme.1344.
- [151] W. Wunderlich and W. D. Pilkey. *Mechanics of structures: variational and computational methods*. 2nd ed. Boca Raton, FL: CRC Press, 2003. ISBN: 978-0-8493-0700-3.
- [152] O. C. Zienkiewicz and R. L. Taylor. *The finite element method*. 5th ed. Oxford ; Boston: Butterworth-Heinemann, 2000. ISBN: 0-7506-5049-4.

## Bisherige Titel der Schriftenreihe

### Band Titel

- 1 Frank Koschnick, *Geometrische Lockingeffekte bei Finiten Elementen und ein allgemeines Konzept zu ihrer Vermeidung*, 2004.
- 2 Natalia Camprubi, *Design and Analysis in Shape Optimization of Shells*, 2004.
- 3 Bernhard Thomee, *Physikalisch nichtlineare Berechnung von Stahlfaserbetonkonstruktionen*, 2005.
- 4 Fernaß Daoud, *Formoptimierung von Freiformschalen - Mathematische Algorithmen und Filtertechniken*, 2005.
- 5 Manfred Bischoff, *Models and Finite Elements for Thin-walled Structures*, 2005.
- 6 Alexander Hörmann, *Ermittlung optimierter Stabwerkmodelle auf Basis des Kraftflusses als Anwendung plattformunabhängiger Prozesskopplung*, 2006.
- 7 Roland Wüchner, *Mechanik und Numerik der Formfindung und Fluid-Struktur-Interaktion von Membrantragwerken*, 2006.
- 8 Florian Jurecka, *Robust Design Optimization Based on Meta-modeling Techniques*, 2007.
- 9 Johannes Linhard, *Numerisch-mechanische Betrachtung des Entwurfsprozesses von Membrantragwerken*, 2009.
- 10 Alexander Kupzok, *Modeling the Interaction of Wind and Membrane Structures by Numerical Simulation*, 2009.
- 11 Bin Yang, *Modified Particle Swarm Optimizers and their Application to Robust Design and Structural Optimization*, 2009.

**Band Titel**

- 12 Michael Fleischer, *Absicherung der virtuellen Prozesskette für Folgeoperationen in der Umformtechnik*, 2009.
- 13 Amphon Jrusjrungkiat, *Nonlinear Analysis of Pneumatic Membranes - From Subgrid to Interface*, 2009.
- 14 Alexander Michalski, *Simulation leichter Flächentragwerke in einer numerisch generierten atmosphärischen Grenzschicht*, 2010.
- 15 Matthias Firl, *Optimal Shape Design of Shell Structures*, 2010.
- 16 Thomas Gallinger, *Effiziente Algorithmen zur partitionierten Lösung stark gekoppelter Probleme der Fluid-Struktur-Wechselwirkung*, 2011.
- 17 Josef Kiendl, *Isogeometric Analysis and Shape Optimal Design of Shell Structures*, 2011.
- 18 Joseph Jordan, *Effiziente Simulation großer Mauerwerksstrukturen mit diskreten Rissmodellen*, 2011.
- 19 Albrecht von Boetticher, *Flexible Hangmurenbarrieren: Eine numerische Modellierung des Tragwerks, der Hangmure und der Fluid-Struktur-Interaktion*, 2012.
- 20 Robert Schmidt, *Trimming, Mapping, and Optimization in Isogeometric Analysis of Shell Structures*, 2013.
- 21 Michael Fischer, *Finite Element Based Simulation, Design and Control of Piezoelectric and Lightweight Smart Structures*, 2013.
- 22 Falko Hartmut Dieringer, *Numerical Methods for the Design and Analysis for Tensile Structures*, 2014.
- 23 Rupert Fisch, *Code Verification of Partitioned FSI Environments for Lightweight Structures*, 2014.
- 24 Stefan Sicklinger, *Stabilized Co-Simulation of Coupled Problems Including Fields and Signals*, 2014.

**Band Titel**

- 25 Madjid Hojjat, *Node-based parametrization for shape optimal design*, 2015.
- 26 Ute Israel, *Optimierung in der Fluid-Struktur-Interaktion - Sensitivitätsanalyse für die Formoptimierung auf Grundlage des partitionierten Verfahrens*, 2015.
- 27 Electra Stavropoulou, *Sensitivity analysis and regularization for shape optimization of coupled problems*, 2015.
- 28 Daniel Markus, *Numerical and Experimental Modeling for Shape Optimization of Offshore Structures*, 2015.
- 29 Pablo Suárez, *Design Process for the Shape Optimization of Pressurized Bulkheads as Components of Aircraft Structures*, 2015.
- 30 Armin Widhammer, *Variation of Reference Strategy - Generation of Optimized Cutting Patterns for Textile Fabrics*, 2015.
- 31 Helmut Masching, *Parameter Free Optimization of Shape Adaptive Shell Structures*, 2016.
- 32 Hao Zhang, *A General Approach for Solving Inverse Problems in Geophysical Systems by Applying Finite Element Method and Metamodel Techniques*, 2016.
- 33 Tianyang Wang, *Development of Co-Simulation Environment and Mapping Algorithms*, 2016.
- 34 Michael Breitenberger, *CAD-integrated Design and Analysis of Shell Structures*, 2016.
- 35 Önay Can, *Functional Adaptation with Hyperkinematics using Natural Element Method: Application for Articular Cartilage*, 2016.